GENERATION OF LONG WATER WAVES BY MOVING DISTURBANCES

Thesis by

Seung-Joon Lee

In Partial Fulfillment of the Requirements

for the Degree of

Doctor of Philosophy

California Institute of Technology

Pasadena, California

1985

(Submitted May 17, 1985)

ACKNOWLEDGMENTS

My sincere thanks and respects go to my teacher, Professor Theodore Yao-Tsu Wu, who suggested the topic and offered the most valuable guidance throughout the graduate study.

I was strongly influenced by my teachers back home, Korea, especially by Professor J. H. Hwang, whom I thank for introducing me to fluid mechanics and for encouraging me to continue my study at Caltech.

Special thanks are due Dr. George T. Yates for his friendship and for his help in the experiments. I appreciate greatly his assistance in the final correction of the manuscript.

I am deeply indebted to Miss Helen Burrus, who provided friendship and encouragement all these years and typed this thesis.

The deepest appreciation of all goes to my parents and my wife, who have sacrificed the most to make this a reality.

I gratefully acknowledge financial support from the Ministry of Education of Korea, the National Science Foundation, the Office of Naval Research, the J. S. Fluor Graduate Fellowship and the California Institute of Technology.

ABSTRACT

Several theoretical models are developed to study generation of nonlinear dispersive long waves by moving disturbances. All these models belong to the same class as the original Boussinesq or KdV model. The newly developed models, now with external forcing functions added to the KdV equation and the pair of coupled Boussinesq equations, have been chosen for numerical investigations. A predictor-corrector method is adopted to develop the numerical schemes employed here. In order to make the region of computation reasonably small for the case with moving disturbances, a pseudo-moving frame and the sufficiently transparent open boundary conditions are devised. The numerically obtained surface elevations exhibit a series of positive waves running ahead of the disturbance over a wide range of transcritical speeds of the disturbance. The numerical results show that, for speeds close to the critical value, the generation of such waves appears to continue indefinitely. The numerically obtained wave resistance coefficient is compared to the results given by linear dispersive theory. Numerical solutions have been obtained using the KdV and Boussinesq models with surface pressure and bottom bump as forcing functions. Comparisons are made between these results for various cases. Experiments were conducted for a two-dimensional bottom bump moving steadily in shallow water of a towing tank. Experimental results so attained are compared with the numerical solutions, and the agreement between them is good in terms of both the magnitude and the phase of the waves for the range of parameters used in the current study.

TABLE OF CONTENTS

LIST OF TABLES

LIST OF FIGURES

LIST OF FIGURES (cont'd)

LIST OF FIGURES (cont'd)

LIST OF FIGURES (cont'd)

LIST OF FIGURES (cont'd)

LIST OF FIGURES (cont'd)

LIST OF FIGURES (cont'd)

LIST OF FIGURES (cont'd)

I. INTRODUCTION

Since the famous experimental work of John Scott Russell (1838, 1845), the interplay of nonlinear and dispersive effects in the long wave theory has attracted many great minds in the history of hydrodynamics. The controversy between Russell's observation that the solitary waves maintain a permanent form and the prediction of wave steepening by Airy wave theory was first resolved by Boussinesq (1872), and independently by Rayleigh (1876). By restricting the direction of the wave propagation to be unidirectional, Korteweg and de Vries (1895) obtained what is known today as the Korteweg-de Vries (KdV) equation. They also found the periodic solution of the stationary KdV equation, which they named 'cnoidal waves'. Since the primary concern of these investigators was to explain how long waves can propagate without changing their form, these early works all dealt with free waves. On the other hand, Kelvin (1886) studied the wave generation by a moving object, either a surface pressure or 'a bed inequality'. By reasoning based on the Airy wave theory, he argued that "whether the irregularity (of a bed) be an elevation or a depression, a rising of level must travel upstream ---, this traveling of an elevation upstream must develop a bore". He also showed that linear dispersive theory predicts an unbounded wave elevation as the speed of the moving object approaches the critical speed from below. It may seem puzzling that Kelvin did not further pursue to relate the 'traveling of an elevation upstream' to solitary and cnoidal waves, which must have been known to him. This phenomenon of 'traveling

of an elevation upstream' was encountered again by Thews and Landweber (1935) during the ship model experiments in a towing tank of shallow water. They made an excellent observation which unlike Russell's report did not attract other researchers' attention. In discussing the assumption of a steady-state solution in wave problems involving the radiation condition, Stoker (1952) pointed out that "one should rather formulate and solve an appropriate initial-value problem and then find the solution of the steady-state problem by making a passage to the limit in allowing the time to tend to infinity." Related to this work we note that the starting point of the Kelvin's 1886 paper was the assumption that the steady state exists. In discussing the upstream influence of a solid obstacle in a uniform stream, Benjamin (1970) pointed out the necessity of the 'forward surge,' and assumed 'a uniform long wave that extends to a steadily increasing distance ahead of the body (disturbance).' However, he used the results of linear dispersive theory for further development of his theory in reaching the conclusion and limited his discussion to the case of subcritical speeds (i. e., less than the long-wave limit in linear dispersive theory).

Wu (1979) derived a pair of generalized Boussinesq equations that govern three-dimensional nonlinear dispersive long waves produced by a moving surface pressure distribution and/or a floor motion such as tsunami-genic ground motion. Wu & Wu (1983) solved the generalized Boussinesq equations numerically and reported the phenomena of 'runaway solitons,' which are generated by the surface

disturbance moving with a constant transcritical velocity, and emerging periodically to form a series of positive waves moving ahead of the disturbance.

At the same time runaway solitons, or, as they were called by Kelvin, the traveling of an elevation upstream, were rediscovered by a group of researchers mostly working on ship model experiments in a shallow towing tank, (Huang, Sibul & Wehausen 1982). The most salient feature in these experiments is the formation of the two-dimensional runaway solitons inside the towing tank, even though the disturbance is a three-dimensional model of a ship.

The purpose of the present work is to study the generation of nonlinear dispersive long waves by moving disturbances such as a uniformly moving surface pressure and/or bottom bump. In this thesis, we present several versions of the governing equations, all of which belong to the same class as the original Boussinesq equations or the KdV equation. The surface pressure and the bottom bump appear in the same fashion in the KdV model, while the bottom bump has an additional term for the Boussinesq model. Among the derived equations, the inhomogeneous KdV equation and the pair of coupled Boussinesq equations are chosen for numerical investigations. A finite difference approximation is used to develop numerical methods based on the scheme originally employed by Wu & Wu (1983). To deal with the moving disturbance, a pseudo-moving frame and the open boundary conditions are devised and successfully render the region of computation reasonably small.

Using the numerical method developed for the Boussinesq model, the surface elevations and the wave resistance coefficient are computed for a uniformly moving surface pressure. In contrast to the results of linear dispersive theory, the numerically obtained surface wave elevations exhibit a series of positive waves running ahead of the disturbance for a wide range of speed of the disturbance. The numerical results seem to indicate that, for sufficiently strong disturbances moving in a certain range of transcritical speeds, the generation of such waves will continue indefinitely. The numerically obtained wave resistance coefficient is averaged over time, and compared to the results given by linear dispersive theory. Numerical solutions predicted by the KdV and by the Boussinesq models are compared for the surface pressure and the bottom bump. In the Boussinesq model, the surface pressure acts as a stronger disturbance than the bottom bump, and the disturbance in the KdV model (which does not distinguish the two cases) renders results between the two Boussinesq solutions.

Experiments are conducted for a two-dimensional bottom bump moving uniformly in a shallow water tank. Experimental results are compared with the numerical solutions rendered by both the Boussinesq and the KdV models. The agreement between numerical solutions and experimental data is surprisingly good in terms of both the magnitude and the phase of the waves for the range of parameters used in the current study. The difference between the results predicted by the two models are about the same as that between the experimental data and the results predicted by either of the two models.

II. THEORY OF GENERATION OF NONLINEAR DISPERSIVE LONG WAVES

The Boussinesq equations and the KdV equation have been used to describe nonlinear dispersive long gravity waves in one horizontal dimension of a constant water depth without any external forcing agency. Both models have the same order of approximation; however, the KdV equation has a disadvantage in that it allows waves to move only in one direction. Nevertheless, the KdV equation has been extensively used and investigated, because it is simpler and it can be solved exactly for various cases under a certain type of initial conditions.

In this chapter, the inhomogeneous Boussinesq and KdV equations will be derived for the case when a moving surface pressure is present and/or a bottom irregularity exists which may vary in space and time.

2.1 The Basic Equations

The fluid is assumed inviscid and incompressible with a constant density ρ. Surface tension is neglected, and the wave breaking is not taken into account. For simplicity in the derivation, we shall consider gravity waves propagating in one horizontal dimension.

The undisturbed initial free surface at time $t = 0$ is a horizontal plane at $z = 0$ (Fig. 2.1). The bottom topography is given by

$$z = -h(x, t) = -h_o + b(x, t) \quad , \qquad (2.1)$$

where h_o is the characteristic water depth, and $b(x, t)$ the deviation,

which includes a moving bottom bump. The perturbed free surface elevation is denoted by $\zeta(x, t)$.

The fluid is assumed at rest for $t < 0$. The fluid motion generated by some extraneous forcing agency will be irrotational, in accordance with Helmholtz's vorticity theorem. Therefore, a velocity potential $\phi(x, z, t)$ exists such that

$$\nabla\phi = \underline{u}(x, z, t) = (u, w) \quad , \tag{2.2}$$

where $\underline{u}$ is the velocity vector, and $\nabla = [(\ )_x, (\ )_z]$. Here the subscripts x, z and t stand for partial differentiation.

The equation of continuity becomes the Laplace equation

$$\nabla \cdot \underline{u} = \Delta\phi(x, z, t) = 0, \quad \text{for } -\infty < x < \infty, \ -h(x, t) < z < \zeta(x, t) \ . \tag{2.3}$$

The boundary conditions for $\phi(x, z, t)$ are:

on the free surface $z = \zeta(x, t)$;

1. the kinematic boundary condition,

$$\zeta_t + \phi_x\zeta_x - \phi_z = 0 \quad , \tag{2.4}$$

2. the dynamic boundary condition,

$$\phi_t + \frac{p_o}{\rho} + \frac{1}{2}(\phi_x^2 + \phi_z^2) + gz = 0 \quad , \tag{2.5}$$

on the bottom $z = -h(x, t)$;

3. the kinematic boundary condition,

$$b_t + \phi_x b_x - \phi_z = 0 \quad , \tag{2.6}$$

where $p_o = p_o(x, t)$ is a prescribed distribution of pressure on the

free surface, and g is the gravitational acceleration.

The initial conditions at $t = 0$ are:

$$\phi(x, z, 0) = 0 \ , \tag{2.7a}$$

$$\zeta(x, 0) = 0 \ . \tag{2.7b}$$

It is desirable to work with the following dimensionless variables:

$$x^* = x/\lambda, \ (z^*, \zeta^*, h^*, b^*) = (z, \zeta, h, b)/h_o, \ t^* = c_o t/\lambda \ , \tag{2.8}$$

$$\phi^* = \phi/c_o\lambda \ , \ (Fn, u^*, w^*) = (U, u, w)/c_o, \ p_o^* = p_o/\rho g h_o \ ,$$

where λ is the characteristic wavelength, and U the speed of the moving disturbance, and c_o the characteristic critical speed defined as

$$c_o = (gh_o)^{1/2} \ . \tag{2.9}$$

In terms of the dimensionless variables, with the superscript * omitted for brevity, the initial boundary value problem for $\phi(x, z, t)$ becomes:

the equation of continuity,

$$\phi_{xx} + \beta^{-1}\phi_{zz} = 0 \quad \text{for} \quad -1 + b(x, t) < z < \zeta(x, t) \ , \tag{2.10}$$

the kinematic free surface boundary condition,

$$\zeta_t + \phi_x\zeta_x - \beta^{-1}\phi_z = 0 \quad \text{on} \quad z = \zeta(x, t) \ , \tag{2.11}$$

the dynamic free surface boundary condition,

$$\phi_t + \frac{1}{2}(\phi_x^2 + \beta^{-1}\phi_z^2) + \zeta + p_o = 0 \quad \text{on} \quad z = \zeta(x, t) \ , \qquad (2.12)$$

the kinematic bottom boundary condition,

$$b_t + \phi_x b_x - \beta^{-1}\phi_z = 0 \quad \text{on} \quad z = -1 + b(x, t) \ , \qquad (2.13)$$

the initial conditions,

$$\phi(x, z, 0) = 0 \ , \qquad (2.14a)$$

$$\zeta(x, 0) = 0 \ , \qquad (2.14b)$$

where the dimensionless parameter β is defined as

$$\beta = (h_o/\lambda)^2 \ . \qquad (2.15)$$

If we denote the characteristic wave amplitude as a, it is obvious that

$$\zeta(x, t) = O(\alpha) \ , \qquad (2.16)$$

where

$$\alpha = a/h_o \ . \qquad (2.17)$$

From the dynamic free surface condition, eq. (2.12), it also follows that

$$\phi(x, z, t) = O(\alpha) \ . \qquad (2.18)$$

The dimensionless parameter α measures nonlinear effects while β indicates the importance of dispersive effects. Both of them are assumed small, however, as shown by Ursell (1953); their ratio determines whether nonlinear or dispersive effects dominate the

wave phenomena. This ratio, called the Ursell number Ur, is defined as

$$Ur = \alpha/\beta \ . \tag{2.19}$$

In the present study, we are primarily interested in the case when

$$Ur = O(1) \ , \tag{2.20}$$

which implies that nonlinear and dispersive effects are of equal importance.

2.2 The Inhomogeneous Boussinesq Equations

In analogy with Rayleigh's (1876) analysis for the homogeneous problem (the case of constant water depth without external forcing), the following asymptotic expansion for $\phi(x, z, t)$ is assumed

$$\phi(x, z, t) = \psi - \frac{\beta(1+z)^2}{2!}\psi_{xx} + \frac{\beta^2(1+z)^4}{4!}\psi_{xxxx} + \ldots + \beta F_1(x, z, t) + \beta^2 F_2(x, z, t) + \ldots \ . \tag{2.21}$$

where

$$\psi(x, t) = O(\alpha) \ , \tag{2.22}$$

$$F_i(x, z, t) = O(\alpha) \ , \quad i = 1, 2, 3, \ldots \ . \tag{2.23}$$

A solution of the form (2.21) will satisfy Laplace eq. (2.10) everywhere in the fluid, provided

$$F_{1zz} = 0 \ , \tag{2.24a}$$

$$F_{2zz} = -F_{1xx} \ , \tag{2.24b}$$

$$\ldots \ .$$

Under the further assumption that

$$b(x,t) = O(\alpha) \ , \tag{2.25}$$

the bottom boundary condition, (2.13), requires that

$$F_{1z} = b_t \ , \tag{2.26a}$$

$$\beta F_{2z} = b\psi_{xx} + b_x\psi_x - bF_{1zz}, \quad \text{on } z = -1 \ . \tag{2.26b}$$

Integrating eqs. (2.24) and applying the boundary conditions (2.26) gives

$$F_1(x,z,t) = zb_t + f_1(x,t) \ , \tag{2.27a}$$

$$F_2(x,z,t) = \beta^{-1}z(b\psi_{xx} + b_x\psi_x) + b_{txx}(\frac{z}{2} - \frac{z^3}{3!}) - zf_{1xx}(1+\frac{z}{2}) + f_2(x,t) \ . \tag{2.27b}$$

The arbitrary functions $f_1(x,t)$, $f_2(x,t)$ can be absorbed into $\psi(x,t)$ by letting

$$\psi'(x,t) = \psi(x,t) + \beta f_1 + \beta^2(\frac{1}{2}f_{1_{xx}} + f_2) \ .$$

Now dropping the $'$ and using the new ψ in (2.21), the expansion of the velocity potential satisfying the equation of continuity and the bottom boundary condition can be written as

$$\phi(x,z,t) = \psi - \frac{\beta(1+z)^2}{2!}\psi_{xx} + \frac{\beta^2(1+z)^4}{4!}\psi_{xxxx} + \beta z(b_t + b\psi_{xx} + b_x\psi_x) + \beta^2(\frac{z}{2} - \frac{z^3}{3!})b_{txx} + O(\alpha\beta^3) \ . \tag{2.28}$$

This expansion contains only one unknown function $\psi(x, t)$, and the z-dependence is completely determined up to the highest-order terms retained. We note that in the absence of external disturbances, the terms with F_i's in eq. (2.21) all vanish and the expansion (2.21) reduces to Rayleigh's form.

The boundary conditions on the free surface are essentially nonlinear as the location of the free surface is a part of the solution. With the assumption

$$p_o(x, t) = O(\alpha) \quad , \tag{2.29}$$

substitution of eq. (2.28) into eqs. (2.11) and (2.12) results in

$$(\zeta_t - b_t) + [(1 - b + \zeta)\psi_x]_x - \beta(\frac{1}{6}\psi_{xxxx} + \frac{1}{2} b_{txx}) + \text{HOTS} = 0 \quad , \tag{2.30}$$

$$\psi_t + \zeta + \frac{1}{2}\psi_x^2 - \frac{\beta}{2}\psi_{xxt} + p_o + \text{HOTS} = 0 \quad , \tag{2.31}$$

where HOTS stands for $O(\alpha^2\beta, \alpha\beta^2)$. These two equations along with the initial conditions constitute the basic system for determining $\psi(x, t)$ and $\zeta(x, t)$. The inhomogeneous Boussinesq equations are derived by replacing $\psi(x, t)$ with the layer mean velocity potential $f(x, t)$ defined as

$$f(x, t) = (1 - b + \zeta)^{-1} \int_{-1+b(x,t)}^{\zeta(x,t)} \phi(x, z, t)dz \quad . \tag{2.32}$$

From this and (2.28) we deduce the relations between $\psi(x, t)$ and $f(x, t)$ as

$$f(x,t) = \psi(x,t) - \beta\left(\frac{1}{6}\psi_{xx} + \frac{1}{2}b_t\right) + O(\alpha\beta^2) \quad , \tag{2.33a}$$

$$\psi(x,t) = f(x,t) + \beta\left(\frac{1}{6}f_{xx} + \frac{1}{2}b_t\right) + O(\alpha\beta^2) \quad . \tag{2.33b}$$

From eqs. (2.30), (2.31) and (2.33b), the inhomogeneous Boussinesq equations are found

$$(\zeta_t - b_t) + [(1 - b + \zeta)f_x]_x + \text{HOTS} = 0 \quad , \tag{2.34}$$

$$f_t + \zeta + \frac{1}{2}f_x^2 - \frac{\beta}{3}f_{xxt} + p_o + \frac{\beta}{2}b_{tt} + \text{HOTS} = 0 \quad . \tag{2.35}$$

A similar set of equations was obtained by Wu (1979) under the less restrictive assumption that $b_x = O(1)$. Wu's equations reduce to (2.34, 2.35) when b is taken $O(\alpha)$, as in the present development.

The two equations (2.34, 2.35) can be combined by eliminating $\zeta(x,t)$ to yield a single fourth-order partial differential equation for $f(x,t)$ as

$$f_{tt} - f_{xx} + 2f_x f_{xt} + f_t f_{xx} - \frac{\beta}{3}f_{xxtt} + \text{HOTS} = \tag{2.36}$$

$$-[(p_o + b)_t + \{(p_o + b)f_x\}_x] - \frac{\beta}{2}b_{ttt} \quad .$$

This combined inhomogeneous Boussinesq equation shows some interesting features. The surface pressure appears to leading order in the same manner as the bottom disturbance. There is, however, an additional term at second order for the bottom disturbance which is absent for the surface pressure. This suggests that whenever the disturbances are small a surface pressure may produce a very similar solution as a bottom bump if both disturbances are prescribed by the

same function. As the disturbance becomes larger, the b_{ttt} term in (2.36) will no doubt make a contribution and some differences between the location and type of disturbances will become apparent. Lepelletier (1981) and Schember (1982) obtained a similar expression under the same assumption as Wu (1979), and used it in their numerical computation.

2.3 The Inhomogeneous KdV Equation

For the homogeneous case, the KdV equation can be derived from the Boussinesq equations by restricting the direction of the wave propagation, as shown by Whitham (1974). To derive the inhomogeneous KdV equation, the additional assumptions that

$$p_o(x, t) = O(\alpha\beta) \quad , \tag{2.37}$$

$$b(x, t) = O(\alpha\beta) \quad , \tag{2.38}$$

are necessary. Since these are more restrictive than the assumptions in the previous section, the original set of eqs. (2.28, 2.30, 2.31, 2.33, 2.34, 2.35, 2.36) all remain valid, if the terms of the same order as the neglected are neglected for consistency. For later use, we rewrite some of them below:

the expansion of the velocity potential,

$$\phi(x, z, t) = \psi - \frac{\beta(1+z)^2}{2!}\psi_{xx} + \frac{\beta^2(1+z)^4}{4!}\psi_{xxxx} + \beta z b_t + O(\alpha\beta^3) \quad , \tag{2.39}$$

the relations between $\psi(x, t)$ and $f(x, t)$,

$$f(x, t) = \psi(x, t) - \frac{\beta}{6}\psi_{xx} + O(\alpha\beta^2) \quad , \tag{2.40a}$$

$$\psi(x, t) = f(x, t) + \frac{\beta}{6} f_{xx} + O(\alpha\beta^2) \quad , \tag{2.40b}$$

the pair of equations for $f(x, t)$ and $\zeta(x, t)$,

$$(\zeta_t - b_t) + [(1 + \zeta)f_x]_x + \text{HOTS} = 0 \quad , \tag{2.41}$$

$$f_t + \zeta + \frac{1}{2} f_x^2 - \frac{\beta}{3} f_{xxt} + p_o + \text{HOTS} = 0 \quad , \tag{2.42}$$

the combined fourth order partial differential equation for $f(x, t)$,

$$f_{tt} - f_{xx} + 2f_x f_{xt} + f_t f_{xx} - \frac{\beta}{3} f_{xxtt} + \text{HOTS} = -(p_o + b)_t \quad . \tag{2.43}$$

It is useful to introduce the layer mean horizontal velocity $v(x, t)$ defined as

$$v(x, t) = (1 - b + \zeta)^{-1} \int_{-1+b(x,t)}^{\zeta(x,t)} \phi_x(x, z, t)dz \quad . \tag{2.44}$$

Thus, the relation between $v(x, t)$ and $f_x(x, t)$ becomes

$$v(x, t) = f_x(x, t) + \text{HOTS} \quad . \tag{2.45}$$

If we replace f_x by v in eq. (2.41) and in the x-differentiated version of eq. (2.42), we have

$$(\zeta - b)_t + [(1 + \zeta)v]_x + \text{HOTS} = 0 \quad , \tag{2.46}$$

$$v_t + \zeta_x + vv_x - \frac{\beta}{3} v_{xxt} + p_{ox} + \text{HOTS} = 0 \quad . \tag{2.47}$$

The lowest-order approximation to these gives

$$\zeta_t + v_x = 0 \quad \text{and} \quad v_t + \zeta_x = 0 \quad . \tag{2.48}$$

If the eqs. (2.37, 2.38) had not been assumed, we should have obtained

$$\zeta_t + u_x = b_t \quad \text{and} \quad u_t + \zeta_x = -p_{ox} \ , \tag{2.49}$$

which is a system of inhomogeneous linear nondispersive long-wave equations. Eliminating u gives

$$\zeta_{tt} - \zeta_{xx} = p_{oxx} + b_{tt} \ .$$

A solution of this for a uniformly moving disturbance such that

$$p_o = p_o(x - tFn) \quad \text{and} \quad b = b(x - tFn)$$

is given by

$$\zeta = \begin{cases} (Fn^2 - 1)^{-1}(p_o + F_n{}^2 b), & \text{for } Fn \neq 1 \ , \\ \text{not defined}, & \text{for } Fn = 1 \ , \end{cases}$$

as can be easily proved by back substitution (see Lamb (1932)). We may therefore conclude that the forcing disturbance p_o and b must be of higher order than the leading terms because otherwise no bounded solution exists at Fn = 1.

If we restrict ourselves to a wave moving to the right, a solution of eq. (2.48) is

$$v = \zeta \ , \tag{2.50}$$

$$\zeta_t + \zeta_x = 0 \ . \tag{2.51}$$

Then, we look for the next-order approximation of the form

$$v = \zeta + \alpha C + \beta D \ , \tag{2.52}$$

where C and D are $O(\alpha, \beta)$. Substituting eq. (2.52) into eqs. (2.46, 2.47) we get

$$(\zeta_t + \zeta_x) + (2\zeta\zeta_x - b_t + \alpha C_x) + \beta D_x + \text{HOTS} = 0, \qquad (2.53)$$

$$(\zeta_t + \zeta_x) + (\zeta\zeta_x + p_{ox} + \alpha C_t) + \beta(D_t - \tfrac{1}{3}\zeta_{xxt}) + \text{HOTS} = 0 . \qquad (2.54)$$

The eq. (2.51) implies that we may replace the t derivatives with the minus x derivatives for the terms of $o(\alpha, \beta)$; thus, eqs. (2.53, 2.54) are consistent if

$$\alpha C = -\tfrac{1}{4}\zeta^2 + \tfrac{1}{2}(p_o - b) , \qquad (2.55)$$

$$D = \tfrac{1}{6}\zeta_{xx} . \qquad (2.56)$$

Hence we have

$$v(x, t) = \zeta - \tfrac{1}{4}\zeta^2 + \tfrac{\beta}{6}\zeta_{xx} + \tfrac{1}{2}(p_o - b) + \text{HOTS} , \qquad (2.57)$$

$$\zeta_t + (1 + \tfrac{3}{2}\zeta)\zeta_x + \tfrac{\beta}{6}\zeta_{xxx} + \text{HOTS} = -\tfrac{1}{2}(p_{ox} + b_x) . \qquad (2.58)$$

Equation (2.58) is called the inhomogeneous KdV equation, which implies that under the more restrictive assumptions (2.37, 2.38) a surface pressure and a bottom bump of equal functional distribution will produce the same wave field. Akylas (1984) and Cole (1985) derived a similar equation for a similar problem, however, with the delta function on the right-hand side. The KdV model presented here is an approximation uniformly valid in time t and in the

entire region of x for the forced motion, while both Akylas and Cole derived it as an equation valid only for their outer problem.

2.4 Wave Resistance

A disturbance moving through an inviscid fluid having a free surface will experience a resistance due to the generation of waves. This wave resistance can be obtained in various ways, and here the work-energy principle is implemented for the entire fluid domain. We shall use dimensional quantities until the final results are obtained.

The energy density $e(x, z, t)$ of the fluid is defined as

$$e(x, z, t) = \frac{u^2}{2} + gz \quad . \tag{2.59}$$

The time rate of change of the total energy $E(t)$ in the entire fluid domain $S(t)$ is

$$dE/dt = (d/dt)\int_{S(t)} e(x, z, t)\rho dS = \int_{S(t)} (de/dt)\rho dS \quad . \tag{2.60}$$

To compute de/dt, we use the Euler equation

$$du/dt = -\nabla(p/\rho + gz) \quad , \tag{2.61}$$

and find

$$\rho(de/dt) = -\underline{u} \cdot \nabla p = -\nabla \cdot (p\underline{u}) \quad , \tag{2.62}$$

where the equation of continuity, $\nabla \cdot \underline{u} = 0$, has been used for the last equality. Thus we have

$$dE/dt = -\int_{S(t)} \nabla\cdot(p\underline{u})dS$$

$$= -\int_{-\infty}^{\infty} dx \int_{-h}^{\zeta} [(pu)_x + (pw)_z]dz \qquad (2.63)$$

$$= -\int_{-\infty}^{\infty} [\int_{-h}^{\zeta}(pu)dz]_x dx + \int_{-\infty}^{\infty} \{[p(u\zeta_x - w)]_{z=\zeta} - [p(ub_x - w)]_{z=-h}\}dx \, .$$

The first integral in the last expression vanishes. Hence the kinematic boundary conditions on the free surface and on the bottom, eqs. (2.4) and (2.6), give

$$dE/dt = -\int_{-\infty}^{\infty} (p_o\zeta_t - p_b b_t)dx \, , \qquad (2.64)$$

where p_b is the pressure at the bottom. The same result was also derived by Wu (1979). For a moving disturbance of finite length, the integrand vanishes except over the length L of the disturbance.

For a disturbance moving uniformly to the left with the velocity U, we define a moving reference frame (x', z', t') by

$$x' = x + Ut, \quad z' = z, \quad t' = t \, . \qquad (2.65)$$

For a surface pressure and a bottom bump dE/dt can be rewritten as

$$dE/dt = -U\int_L (p_o(x')\zeta_{x'})dx' - \int_L (p_o\zeta_{t'})dx' \, , \qquad (2.66)$$

$$dE/dt = U\int_L [p_b(x', t')b_{x'}(x')]dx' \quad , \tag{2.67}$$

respectively.

By the work-energy principle dE/dt must be equal to the work done by the moving disturbance. If the wave resistance is denoted by $R(t)$, we must have

$$dE/dt = UR + B \quad , \tag{2.68}$$

where $B = B(t)$ represents the rate of the work done due to the vertical wave motion underneath the disturbance.

For a surface pressure, if there exists a steady-state solution, then the second integral vanishes, and so does B because there is no vertical motion of the fluid with respect to the moving frame. In general, however, B is nonzero. The wave resistance and B can be identified from (2.66)

$$R = -\int_L (p_o\zeta_{x'})dx' \quad , \tag{2.69}$$

$$B = -\int_L (p_o\zeta_{t'})dx' \quad . \tag{2.70}$$

For a bottom bump B is identically zero, and the wave resistance is given by

$$R = \int_L (p_b b_{x'})dx' \quad . \tag{2.71}$$

The coefficient of the wave resistance is defined as

$$C_R = R/\rho g h_o^2 \quad . \tag{2.72}$$

Then eqs. (2.67, 2.71) give C_R for each case in terms of the dimensionless variables as follows:

for a surface pressure,

$$C_R = -\int_L (p_o \zeta_{x'}) dx' \quad ; \tag{2.73}$$

for a bottom bump,

$$C_R = \int_L (p_b b_{x'}) dx' \quad , \tag{2.74}$$

where $L^* = L/\lambda$, and $p_b^* = p_b/\rho g h_o$ and the superscript * is omitted. p_b is obtained by the Bernoulli's equation applied at the bottom

$$p_b = 1 - b - \psi_t + O(\alpha\beta) \quad . \tag{2.75}$$

In the absence of surface pressure, the Bernoulli's equation applied to the free surface gives

$$\psi_t = -\zeta + O(\alpha\beta) \quad . \tag{2.76}$$

Combining (2.75, 2.76), we obtain

$$p_b = 1 - b + \zeta + O(\alpha\beta) \quad . \tag{2.77}$$

For the KdV model b is neglected for consistency.

III. NUMERICAL METHODS

In the previous chapter we derived several versions of equivalent model equations. They all belong to the same class as the original Boussinesq model and in principle any of them can be used to study the propagation of nonlinear dispersive long waves generated by moving disturbances. In this chapter we choose for numerical investigations the inhomogeneous Boussinesq equations (2.34, 2.35) and the inhomogeneous KdV equation (2.58), for which we will use a finite difference approximation to develop numerical methods based upon the scheme employed by Wu & Wu (1983).

Once the governing equations are derived, they can be rewritten in terms of the dimensional variables. Now for a moving disturbance spanning over a finite length, this length L can be used in place of λ in nondimensionalization. Having done so, we obtain the same equations in dimensionless form as before but with the new definition of x^*, t^*, ϕ^* and β as follows:

$$x^* = x/L, \quad t^* = c_o t/L, \quad \phi^* = \phi/c_o L \ , \qquad \beta = (h_o/L)^2 \ , \tag{3.1}$$

where the quantities on the right-hand side are dimensional. We also introduce another dimensionless parameter ϵ and time T^* defined as

$$\epsilon = h_o/L \ , \tag{3.2a}$$

$$T^* = c_o t/h_o = t^*/\epsilon \ . \tag{3.2b}$$

Here and in the sequel, the asterisk * will be omitted for brevity.

3.1 The Inhomogeneous KdV Equation

From eqs. (2.58) and (2.14b), the inhomogeneous KdV equation along with the initial condition is given by

$$\pm \zeta_t + (1 + \frac{3}{2}\zeta)\zeta_x + \frac{\beta}{6}\zeta_{xxx} = -d \quad , \tag{3.3}$$

$$\zeta = 0 \quad \text{at} \quad t = 0 \quad , \tag{3.4}$$

where the +(-) sign is taken for a disturbance moving to the right(left), and

$$d(x, t) = \frac{1}{2}(p_o + b)_x \quad . \tag{3.5}$$

For the reason of numerical stability, as shown by Whitham (1974), we replace the dispersion term ζ_{xxx} with $\pm\zeta_{xxt}$ (+, left-going; −, right-going) in (3.3), by invoking the lowest order approximation. Thus the KdV equation becomes

$$\zeta_t - (1 + \frac{3}{2}\zeta)\zeta_x - \frac{\beta}{6}\zeta_{xxt} = d \quad , \tag{3.6}$$

for a disturbance moving to the left, which we shall consider throughout this study.

Equation (3.6) will be approximated by a finite difference equation. In discretization the forward difference is used for the time derivatives and the central difference is used for the spatial derivatives. The resulting difference equation is solved in a finite spatial domain, $x_0 \leq x \leq x_N$, which is called a window. We denote the uniform grid size in space by Δx. Then the number of

grid points is $N + 1$, where

$$N = (x_N - x_0)/\Delta x \quad . \tag{3.7}$$

The uniform grid size in time is denoted by Δt. For any function $Q(x, t)$, we adopt the following notation

$$Q_i^j = Q(x_0 + i\Delta x,\ j\Delta t) \quad \text{for} \quad i = [0, N],\ j = [0, \infty) \ , \tag{3.8}$$

and

$$Q^j = (Q_1^j,\ Q_2^j,\ \ldots,\ Q_{N-1}^j)^T \ , \tag{3.9}$$

where Q^j is a $(N-1)$-dimensional column vector, and the superscript T stands for the transpose.

For computational reasons, it is desirable to have a reasonably small window size. Since the disturbance is moving, it will eventually hit the boundary. To prevent this, we introduce a pseudo-moving frame, which moves in the direction of the motion of the disturbance.

A definition sketch is given in Fig. 3.1.

To advance in time, a predictor-corrector method is employed without iteration at the corrector stage. The local truncation error is of $O(\Delta x^2, \Delta t^2)$.

For the predictor vector η we have:

$$-\gamma\eta_{i-1} + (1 + 2\gamma)\eta_i - \gamma\eta_{i+1} =$$

$$-\gamma\zeta_{i-1}^j + (1 + 2\gamma)\zeta_i^j - \gamma\zeta_{i+1}^j + \Delta t(d_i^j + q_i^j)$$

$$\text{for} \quad i = [1, N-1],\ j = [0, K-1] \ , \tag{3.10}$$

where $K\Delta t$ is the final time level and

$$\gamma = \beta(6\Delta x^2)^{-1} \quad , \tag{3.11}$$

$$q_i^j = -(2\Delta x)^{-1}(1 + \frac{3}{2}\zeta_i^j)(\zeta_{i+1}^j - \zeta_{i-1}^j) \quad . \tag{3.12}$$

Equation (3.10) is implicit, as we have to solve a set of simultaneous equations at each time level. In matrix form we have

$$\eta = \zeta^j + \Delta t A^{-1}(d^j + q^j + r^j) \quad , \tag{3.13}$$

where

$$A = \begin{bmatrix} 1+2\gamma & -\gamma & 0 & \cdots & 0 \\ -\gamma & 1+2\gamma & -\gamma & & \\ & & \cdots & & \\ & & -\gamma & 1+2\gamma & -\gamma \\ 0 & \cdots & 0 & -\gamma & 1+2\gamma \end{bmatrix}, \tag{3.14}$$

$$\begin{aligned} r_i^j &= 0, \quad i \neq 1, \ N-1 \ , \\ &= \eta_0 - \zeta_0^j, \quad i = 1 \quad , \\ &= \eta_N - \zeta_N^j, \quad i = N-1 \ . \end{aligned} \tag{3.15}$$

A is a constant tridiagonal matrix of the dimension (N-1), which is strictly diagonally dominant.

The vector r^j is determined by the boundary conditions imposed on the artificial boundaries at $i = 0$ and N. These boundary conditions are called open or transparent boundary conditions, because they are intended to permit the passage of a wave through the boundaries.

To obtain them, we use

$$\zeta_t = \pm \zeta_x \ , \tag{3.16}$$

and the Taylor series expansion up to the second order. The sign in eq. (3.16) is taken so that the waves must leave the window. Hence, the open boundary conditions at i = 0, N are

$$\eta_0 = \zeta_1^j + \frac{\delta}{2}(\zeta_2^j - \zeta_0^j) + \frac{\delta^2}{2}(\zeta_2^j - 2\zeta_1^j + \zeta_0^j) \ , \tag{3.17}$$

$$\eta_N = \zeta_{N-1}{}^j + \frac{\delta}{2}(\zeta_{N-2}{}^j - \zeta_N^j) + \frac{\delta^2}{2}(\zeta_N^j - 2\zeta_{N-1}{}^j + \zeta_{N-2}{}^j) \ , \tag{3.18}$$

where

$$\delta = (\frac{\Delta t}{\Delta x} - 1) \ . \tag{3.19}$$

The corrector vector ζ^{j+1} is given in matrix form by:

$$\zeta^{j+1} = \zeta^j + \Delta t A^{-1}[\frac{1}{2}(d^j + d^{j+1}) + \frac{1}{2}(q^j + s) + r^j] \ , \tag{3.20}$$

where the elements of the vector s are

$$s_i = -(2\Delta x)^{-1}(1 + \frac{3}{2}\eta_i)(\eta_{i+1} - \eta_{i-1}) \ . \tag{3.21}$$

Equation (3.20) is also implicit, and we use the same open boundary conditions for the corrector; i.e.,

$$\zeta_0{}^{j+1} = \eta_0, \quad \zeta_N{}^{j+1} = \eta_N \ . \tag{3.22}$$

The performance of the open boundary conditions is related to the role of the pseudo-moving frame. If we choose Δt and Δx such

that

$$J = \Delta x / \Delta t Fn \tag{3.23}$$

is an integer ($J = 2, 3, 3, \ldots$), then the disturbance travels Δx in J time steps. If we shift the window every J time steps and if we look at the solution only when the window is shifted, the position of the disturbance in the window does not change. At the time of window shifting, a new grid point emerges into view from the upstream side of the window while an old grid point disappears at the downstream side as it moves behind the window. In the interim time levels, while the window remains fixed as well as during window shifting, the mechanical laws are referred to the fluid frame throughout. Thus, only the region of computation undergoes stepwise changes, hence the name pseudo-moving frame. As the shift is done in the direction of the motion of the disturbance, the downstream boundary always chases any waves reflected from this boundary due to the imperfectness of the open boundary condition. If we assume the reflected waves are small in magnitude, they must propagate with a speed almost equal to the critical speed. Therefore, for the moving disturbances with $Fr \approx 1.0$, the reflected waves are limited to the neighborhood of the downstream boundary. The upstream boundary is taken far enough away from the forerunning waves that no waves ever encounter the boundary.

To provide the new upstream boundary value ζ_{-1}^{j+1} when the window is shifted, we use the same principle used to get the open boundary condition, namely,

$$\zeta_{-1}^{j+1} = \zeta_1^j + \frac{1}{2}(\delta - 1)(\zeta_2^j - \zeta_0^j) + \frac{1}{2}(\delta - 1)^2(\zeta_2^j - 2\zeta_1^j + \zeta_0^j) \ . \tag{3.24}$$

With the initial condition

$$\zeta_i^0 = 0, \quad \text{for} \quad i = [0, N] \ , \tag{3.25}$$

the formalism of our numerical procedure is now complete.

We need to know the stability and the convergence of the numerical procedure described so far. There are two ways to examine these aspects of a numerical procedure. One way is to prove the stability and the convergence of the scheme analytically. The other way is to directly run the numerical code for well-chosen test cases. For nonlinear problems, such analyses are generally complicated and linearized analysis often fails to predict nonlinear instability. Therefore, we choose the latter method to investigate the numerical scheme.

To test the stability and the convergence of the code, we first consider the homogeneous case, $d = 0$, without shifting the window. Equation (3.6) with $d = 0$ has a family of exact solutions of permanent form, among which we take a solitary wave solution as an initial condition. We obtain the solitary wave solution by substituting the ansatz

$$\zeta(x + Vt) = a_o \operatorname{sech}^2[K(x + Vt)] \ , \tag{3.26}$$

into the homogeneous version of eq. (3.6) to determine V and K in terms of a_o. We find

$$V = 1 + \frac{a_o}{2} \ , \tag{3.27}$$

$$K = [3a_o/2\beta(2 + a_o)]^{1/2} \ . \tag{3.28}$$

We note that $\beta = \epsilon^2$ is just a scaling ratio of the x- and z-axis in this case.

If $x = 0$ is taken as the position of the initial solitary wave peak, the discretized initial condition is

$$\zeta_i^0 = a_o \operatorname{sech}^2[K\Delta x(i - I_p)] \quad \text{for} \quad i = [0, N] \ , \tag{3.29}$$

where the eq. (3.28) is used for K and

$$I_p = -x_0/\Delta x \ .$$

The numerical solution for $a_o = 0.3$ is shown in Fig. 3.2, for which we used $x_0 = -20$, $x_N = 10$, $\Delta x = 0.1$, $K = 200$, $\Delta t = 0.1$ and $\epsilon = 0.5$. The amplification factor $\Lambda(t)$, defined as

$$\Lambda = \max_x \text{. (peak value-initial amplitude)/(initial amplitude)} \ , \tag{3.30}$$

is about 1% at $K = 160$. The speed of propagation is within 1% of the value predicted by eq. (3.27).

To examine the accuracy of the imposed open boundary condition (3.16), we allowed the above solitary wave to run twice as long, and thus pass through the left boundary, and compared the result to another computation differing only in that a larger window was used ($x_0 = -40$). The effect of the boundary condition is then sought by taking the difference between the two results, as shown in Fig. 3.3. Before the main portion of the solitary wave reaches the boundary ($t < 16$) the difference is negligible. For $t > 16$, the maximum difference is about 1 % of the initial solitary wave amplitude.

Further refinement of the boundary condition can be achieved if we use the relation between V and a_o and

$$\zeta_t = \pm V\zeta_x \ , \tag{3.31}$$

instead of eq. (3.16). The result with this minor modification is even more striking with the maximum difference being less than 0.1 % of the initial wave amplitude.

To determine the proper grid size Δx and Δt, various values were tested. It is clear that smaller grid sizes yield better results; however, very small grids will consume excessive computation time, and we sought intermediate grid sizes to give accurate results with economic computation time.

For the case of the homogeneous problem, since a solitary wave moves with a supercritical speed, it is quite safe to have $\Delta x = \Delta t$. We show in Table 3.1 the comparison of the amplification factor $\Lambda(t)$ for $\Delta x = \Delta t$ equal to 0.05 and 0.1 up to $K = 800$. At the final time level $\Lambda = 0.6$ and 4.4 % for $\Delta x = 0.05$ and 0.1, respectively. Considering that the computation time is four times longer if the grid size is reduced by half, we accepted the error with $\Delta x = 0.1$ for $K \leq 1000$.

For the case of the inhomogeneous problem, J, eqs. (3.23), is chosen so that

$$JFn = \frac{\Delta x}{\Delta t} \approx 2 \ , \tag{3.32}$$

and thus renders Δt about a half of Δx. Although our numerical scheme is implicit, for convergence it is generally believed safe to keep the CFL (Courant-Friedrichs-Lewy) condition with a margin to account for possible departures due to the effects of the nonlinearity. We obtained satisfactory results for $\Delta x = 0.2$ and Δt determined by eq. (3.32) and used these values for all the results presented in this thesis.

The VAX 11/780 digital computer in the Booth Computing Center of Caltech was used for all the computations. A typical case, running for $K = 1000$, used about 120 seconds of CPU time.

3.2 The Inhomogeneous Boussinesq Equations

The system of coupled eqs. (2.34, 2.35) is more preferable for numerical computation than the combined eq. (2.36), since we should use a higher-order implicit scheme for the latter, if a reasonable size of grids is to be used (see Schember (1982)). On the other hand, for the former we can devise a mixed explicit-implicit method, which drastically reduces the computation efforts.

From eqs. (2.34, 2.35) and (2.14), the inhomogeneous Boussinesq equations along with the homogeneous initial conditions are

$$\zeta_t + [(1 - b + \zeta)f_x]_x = b_t \ , \tag{3.33}$$

$$f_t + \zeta + \frac{1}{2} f_x^2 - \frac{\beta}{3} f_{xxt} = -p_o - \frac{\beta}{2} b_{tt} \ , \tag{3.34}$$

$$\zeta = 0 \text{ and } f = 0 \text{ at } t = 0 \ . \tag{3.35}$$

Discretizing these eqs. (3.33, 3.34, 3.35), we adopt the same principles and notations as in the previous section.

We denote the predictor vectors as η, y for ζ, f, respectively, and get

$$\eta_i = \zeta_i^j + \Delta t G_i^j \quad , \tag{3.36}$$

$$\begin{aligned} &-\sigma y_{i-1} + (1 + 2\sigma) y_i - \sigma y_{i+1} = \\ &-\sigma f_{i-1}^j + (1 + 2\sigma) f_i^j - \sigma f_{i+1}^j + \Delta t (P_i^j + Z_i^j) \quad , \\ &\qquad \text{for } i = [1, N - 1], \quad j = [0, K - 1] \quad , \end{aligned} \tag{3.37}$$

where

$$\sigma = \beta (3\Delta x^2)^{-1} \quad , \tag{3.38}$$

and the elements of the vectors G^j, P^j and Z^j are

$$\begin{aligned} G_i^j = {} & b_{ti}^j - \Delta x^{-2} (1 - b_i^j + \zeta_i^j)(f_{i+1}^j - 2 f_i^j + f_{i-1}^j) \\ & -(2\Delta x)^{-1} \{-b_{xi}^j + (2\Delta x)^{-1} (\zeta_{i+1}^j - \zeta_{i-1}^j)\} (f_{i+1}^j - f_{i-1}^j) \quad , \end{aligned} \tag{3.39}$$

$$P_i^j = -p_{oi}^j - \frac{\beta}{2} b_{tti}^j \quad , \tag{3.40}$$

$$Z_i^j = -\zeta_i^j - (8\Delta x^2)^{-1} (f_{i+1}^j - f_{i-1}^j)^2 \quad . \tag{3.41}$$

Equation (3.36) is explicit, as the right-hand side is given in terms of known quantities at the j-th time level. Equation (3.37) is implicit and has exactly the same structure as eq. (3.10). In matrix form we can write

$$\eta = \zeta^j + \Delta t G^j \ , \tag{3.42}$$

$$y = f^j + \Delta t H^{-1}(P^j + Z^j + m^j) \ , \tag{3.43}$$

where H is a constant tridiagonal matrix

$$H = \begin{bmatrix} 1+2\sigma & -\sigma & 0 & \cdots & 0 \\ -\sigma & 1+2\sigma & -\sigma & & \\ & & \cdots & & \\ & & -\sigma & 1+2\sigma & -\sigma \\ 0 & \cdots & 0 & -\sigma & 1+2\sigma \end{bmatrix} , \tag{3.44}$$

and m^j is the boundary vector as explained before (see r^j in (3.15)),

$$\begin{aligned} m_i^j &= 0, \quad i \neq 1, \quad N-1, \\ &= y_0 - f_0^j, \quad i = 1 \ , \\ &= y_N - f_N^j, \quad i = N-1 \ . \end{aligned} \tag{3.45}$$

y_0 and y_N are determined by the open boundary conditions

$$y_0 = f_1^j + \frac{\delta}{2}(f_2^j - f_0^j) + \frac{\delta^2}{2}(f_2^j - 2f_1^j + f_0^j) \ , \tag{3.46}$$

$$y_N = f_{N-1}^j + \frac{\delta}{2}(f_{N-2}^j - f_N^j) + \frac{\delta^2}{2}(f_N^j - 2f_{N-1}^j + f_{N-2}^j) \ . \tag{3.47}$$

For the corrector vectors ζ^{j+1} and f^{j+1} we obtain in matrix form:

$$\zeta^{j+1} = \zeta^{j} + \frac{\Delta t}{2}(G^{j+1} + Y^{j}) , \tag{3.48}$$

$$f^{j+1} = f^{j} + \Delta t H^{-1}[\frac{1}{2}(P^{j} + P^{j+1}) + \frac{1}{2}(Z^{j} + W) + m^{j}] , \tag{3.49}$$

where the vectors Y^{j} and W are given by

$$Y_i^j = b_{ti}^{j+1} - \Delta x^{-2}(1 - b_i^{j+1} + \eta_i)(y_{i+1} - 2y_i + y_{i-1})$$

$$- (2\Delta x)^{-1}\{-b_{xi}^{j+1} + (2\Delta x)^{-1}(\eta_{i+1} - \eta_{i-1})\}(y_{i+1} - y_{i-1}) , \tag{3.50}$$

$$W_i = -\eta_i - (8\Delta x^2)^{-1}(y_{i+1} - y_{i-1})^2 . \tag{3.51}$$

The boundary vector for the corrector is the same as that for the predictor, and thus we have

$$f_0^{j+1} = y_0, \quad f_N^{j+1} = y_N . \tag{3.52}$$

To proceed to the next time level, we need to determine ζ_0^{j+1} and ζ_N^{j+1}. Using the same open boundary conditions, we get

$$\zeta_0^{j+1} = \zeta_1^{j} + \frac{\delta}{2}(\zeta_2^{j} - \zeta_0^{j}) + \frac{\delta^2}{2}(\zeta_2^{j} - 2\zeta_1^{j} + \zeta_0^{j}) , \tag{3.53}$$

$$\zeta_N^{j+1} = \zeta_{N-1}^{j} + \frac{\delta}{2}(\zeta_{N-2}^{j} - \zeta_N^{j}) + \frac{\delta^2}{2}(\zeta_N^{j} - 2\zeta_{N-1}^{j} + \zeta_{N-2}^{j}) . \tag{3.54}$$

When the window is shifted, it is needed to provide the new upstream boundary values ζ_{-1}^{j+1} and f_{-1}^{j+1}, which are computed by

$$\zeta_{-1}^{j+1} = \zeta_1^j + \frac{1}{2}(\delta - 1)(\zeta_2^j - \zeta_0^j) + \frac{1}{2}(\delta - 1)^2(\zeta_2^j - 2\zeta_1^j + \zeta_0^j) , \tag{3.55}$$

$$f_{-1}^{j+1} = f_1^j + \frac{1}{2}(\delta - 1)(f_2^j - f_0^j) + \frac{1}{2}(\delta - 1)^2(f_2^j - 2f_1^j + f_0^j) . \tag{3.56}$$

With the initial conditions

$$\zeta_i^0 = 0, \quad f_i^0 = 0, \quad \text{for } i = [0, N] , \tag{3.57}$$

the numerical procedure is now completed.

To test the stability and the convergence of the code, it is desirable to use a permanent form solution to the homogeneous version of eqs. (3.32, 3.33),

$$\zeta_t + [(1 + \zeta)f_x]_x = 0 , \tag{3.58a}$$

$$f_t + \zeta + \frac{1}{2}f_x^2 - \frac{\beta}{3}f_{xxt} = 0 . \tag{3.58b}$$

However, there is no such a permanent wave solution of eq. (3.58a, b) with a simple form as a solitary wave solution of the KdV equation. On the other hand, the homogeneous version of eq. (2.36) ,

$$f_{tt} - f_{xx} + 2f_x f_{xt} + f_t f_{xx} - \frac{\beta}{3}f_{xxtt} = 0 , \tag{3.59}$$

does admit solitary wave as an exact solution. Although an exact solution of eq. (3.59) does not satisfy eqs. (3.58a, b) exactly, the error is of $O(\alpha^3)$, and we used the exact solution of eq. (3.59) in stability and convergence tests. We obtain the solitary wave solution by substituting the ansatz,

$$f(x + V_B t) = - \frac{a_B}{K_B V_B} \tanh[K_B(x + V_B t)] \quad , \tag{3.60}$$

into the eq. (3.59) to get V_B, K_B in terms of a_B. Equation (3.60) is made an ansatz, because in the lowest-order approximation $- f_t$ and f_x are the surface wave elevation and the horizontal velocity, respectively, and also because f_x must be negative if the wave moves to the left. We find

$$V_B = (1 + a_B)^{1/2} \quad , \tag{3.61}$$

$$K_B = [3a_B/4\beta(1 + a_B)]^{1/2} \quad . \tag{3.62}$$

Taking $a_o = a_B$, we obtain

$$V > V_B \text{ and } K > K_B \quad , \tag{3.63}$$

from eqs. (3.26, 3.27) and (3.61, 3.62). Thus, we see that the KdV solitary wave moves faster and is less dispersed than that of the combined Boussinesq equation. Making use of eq. (3.58b) to find ζ, we have

$$\zeta(x+V_B t) = \frac{a_B}{1+a_B} \{\operatorname{sech}^2[K_B(x+V_B t)] + a_B \operatorname{sech}^4[K_B(x+V_B t)]\} \quad , \tag{3.64}$$

where a_B is confirmed as the peak value at $x + V_B t = 0$. If $x = 0$ is taken at the initial wave peak, the discretized initial conditions are

$$\zeta_i^0 = \frac{a_B}{1+a_B} \{\mathrm{sech}^2[K_B \Delta x(i - I_p)] + a_B \mathrm{sech}^4[K_B \Delta x(i - I_p)]\} , \tag{3.65}$$

$$f_i^0 = -\frac{a_B}{K_B V_B} \tanh [K_B \Delta x(i - I_p)], \quad \text{for } i = [0, N] . \tag{3.66}$$

The numerical solution for $a_B = 0.3$ is shown in Fig. 3.4, for which we used $x_0 = -40$, $x_N = 10$, $\Delta x = 0.1$, $K = 400$, $\Delta t = 0.1$ and $\epsilon = 0.5$. The amplification factor Λ is about 5.9 % and 7.4 % at $K = 160$ and $K = 320$, respectively. Since the initial conditions are not the exact solution of eqs. (3.58a, b), it is not surprising to have some change at the initial stage. Λ changes only 1.5 % between $K = 160$ and 320, which is about the same as we had for the KdV model in the previous section (Λ changed 1 % between $K = 0$ and 160). The proposed open boundary conditions were tested in the same manner as before, and similar results were obtained as shown in Fig. 3.5. The proper grid size for the case of the homogeneous problems was decided as described earlier and the test results are shown in Table 3.2. It shows that for $\Delta x = \Delta t = 0.05$, Λ at $K = 200$ and 1600 are 3.2 % and 4.4 % respectively, which means most of the amplification occurs at the initial stage. For the case of inhomogeneous problems, it is necessary to observe the CFL condition with a margin as the numerical procedure is now half-explicit. $\Delta x = 0.2$ and Δt

given by eqs. (3.32) were also found successful, and were used for most of the results shown in this thesis. A typical case, running for K = 1000, used about 240 seconds of CPU time.

IV. NUMERICAL RESULTS AND DISCUSSION

The numerical results presented in this thesis were obtained using the numerical methods developed in the previous chapter.

For a moving surface pressure, the surface wave elevation and the wave resistance coefficient computed using the Boussinesq model are shown for a full range of the depth Froude number, Fn, from Fn = 0.1 to Fn = 1.3. The wave resistance coefficient numerically obtained is compared with that computed using the linear dispersive theory. The results of the linear dispersive theory are summarized in the Appendix.

For a moving surface pressure and a moving bottom bump, both assuming the same functional distribution, the numerical results predicted by the Boussinesq and the KdV models are compared.

4.1 Numerical Results for a Moving Surface Pressure

The numerical results obtained using the inhomogeneous Boussinesq model for a moving surface pressure are now discussed. We consider the following surface pressure distribution

$$p_o(x + tFn) = \begin{cases} (p_m/2)[1-\cos\{2\pi(x+tFn)\}], & \text{for } 0 \leq (x+tFn) \leq 1 \\ 0, & \text{otherwise.} \end{cases} \qquad (4.1)$$

The motion starts at $t = 0$, and $x = 0$ is the initial leading edge of the disturbance. The surface wave elevation and the wave resistance coefficient were computed for various values of Fn and p_m. The results for $p_m = 0.1$ and $\epsilon = 0.5$ are shown in Figs.

4.1.1-4.1.17. Fn is varied from 0.1 to 1.3 with an increment of 0.1 except in the neighborhood of Fn = 1, where the increment is 0.05. Each figure includes 5 snapshots of the surface wave elevation at equal time intervals as viewed in the pseudo-moving frame and the wave resistance coefficient C_R plotted as a function of time. The position of the disturbance is indicated by two vertical lines. The parameters used in the computation are given in Table 4.1.

4.1.1 The Surface Wave Elevation

To describe the kinematics of the wave system, we divide the range of Fn into 4 groups.

Group 1. Fn = 0.1, 0.2; There are no noticeable waves generated except in the region just underneath the disturbance, where the surface is depressed.

Group 2. Fn = 0.3-0.85; If we are in the moving frame and looking only at the downstream waves, we might think that a steady-state solution would soon be established, since the trailing waves near the disturbance do not seem to be changing soon after the motion starts, say, after four waves have been formed. However, there is a series of positive waves moving ahead of the disturbance, though they are very small in magnitude compared to the trailing waves.

Group 3. Fn = 0.9 - 1.15; We see a series of positive waves of good size running ahead of the disturbance followed by a slowly prolonging negative wave of nearly constant displacement, which is immediately followed by a train of modulated cnoidal waves in the trailing region.

Group 4. Fn = 1.2, 1.3; All the transient waves are swept far downstream, and the surface is elevated only around the disturbance. In this range of Fn, the disturbance only has a local effect.

We note that the depressed prolonging constant wave immediately behind the disturbance, which we shall call the depleted region, is present only in Group 3.

For Groups 1 and 4, the surface elevation is similar to that given by the inhomogeneous linear nondispersive long-wave equation, as discussed in Section 2.3. We may use the linear nondispersive theory for a rough estimate, though there are some small quantitative differences between the predicted amplitudes of the free surface displacement.

For Groups 2 and 3, the wave pattern is drastically different from that predicted by the linear dispersive theory. The positive waves running ahead of the disturbance, called runaway solitons, do not exist at all in the solution of the classical linear theory. Moreover, for the transcritical range of Fn, the linear dispersive theory predicts the wave elevation to increase beyond all bounds as Fn approaches 1 from below, as shown in the Appendix. In drastic contrast, the present nonlinear theory predicts well-defined waves everywhere.

As the runaway soliton propagates upstream for a fixed Fn, its amplitude, a_s, slowly grows. For Fn = 1 the evolving shape of the first runaway soliton is shown in Fig. 4.2.1 at various times. Based on the discussion in Section 3.2, the numerical amplification of the first soliton at the end of the computation time can be estimated

as about 4 % of the initial amplitude shortly after its emergence from the disturbance region. This seems to suggest that there is another reason for the growth in addition to the numerical amplification. A possible reason is that the runaway soliton just generated is not precisely a solitary wave of permanent form and will thus still be undergoing some evolution. In Fig. 4.2.2, for the case of Fn = 1, the first soliton which runs away, when C_R has its second minimum, $t = t_2$, is compared to the permanent form solitary wave of the same amplitude given by eq. (3.65). $t = t_2$ is taken because the first runaway soliton begins to have its tail fairly near the undisturbed water surface at that time. We define the effective wavelength of a solitary wave as the length over which the wave elevation exceeds 3 % of its maximum value (see Lighthill (1978)). Then the Ursell number of the newly born soliton is found to be 32, which is twice that of the permanent form solitary wave with the same effective wavelength, 16, as given by eq. (3.65). Therefore, it seems that the evolution of the runaway soliton is very likely the cause for the continued growth. We will return to this point in the next chapter, where we discuss the experimental results.

The location of the first zero-crossing point of the surface elevation, $x' = x_{xc}$, is of interest for practical importance as well as for understanding the kinematics of waves around the disturbance region. x_{zc} moves back and forth as the runaway solitons are generated and it is at its mean position when the surface elevation above the leading edge is highest or lowest. The wave slope near the leading edge of the pressure distribution is large or small when x_{zc} is at its mean position. In Fig. 4.2.3, we show the time history of x_{zc} for Fn = 1.

As Fn increases, a_s and the time required to generate a runaway soliton, T_s, becomes larger. In Fig. 4.3.1, a_s and T_s are shown as functions of Fn, where a_s is the amplitude of the first runaway soliton at $t = t_2$ and T_s is the time interval between the first two minima of the correspoinding $C_R(t)$ curve.

In Fig. 4.3.2, the mean value and the fluctuation (2nd maximum - 2nd minimum) of x_{zc} are shown as functions of Fn. It indicates that the mean position of the first zero-crossing point is near the leading edge for small Fn's, and moves backward as Fn increases.

We define r_a as

$$r_a = a_s/a_t \quad , \tag{4.2}$$

where a_t is the wave height of the trailing wave closest to the disturbance. Wave height is taken because the trailing waves are cnoidal-like waves. Then, as Fn increases, r_a grows as long as the runaway solitons are generated. In Fig. 4.3.3, r_a is given as a function of Fn. We used a_s and a_t at $t = t_2$ for the computation of r_a. This trend of increasing r_a points out the differences between Group 2 and 3, and clearly shows that for small Fn the trailing waves are the most striking feature, while at higher Fn the leading waves grow to substantial size.

For other values of the p_m (0.05 and 0.15 were investigated), the general trends discussed above are all qualitatively the same. T_s as a function of Fn is presented for $p_m = 0.05,\ 0.1,\ 0.15$ in Fig. 4.3.4. It shows that, as p_m increases, T_s decreases and the upper-bound of Fn, above which no solitons are generated, becomes somewhat larger.

4.1.2 The Wave Resistance

The wave resistance is given by the integration of the pressure distribution multiplied by the wave slope over the disturbance length, (2.69), and is a function of p_m, Fn and time for a given shape of pressure distribution. Variations of the wave slope in the region of the applied pressure distribution are necessary to change the wave resistance.

Thus, for Groups 1 and 4, C_R becomes almost zero after an initial transient period, because no new waves of significant size are generated after that time.

For Groups 2 and 3, $C_R(t)$ curves show as many maxima as there are runaway solitons generated. Since there is no other physical phenomenon observed which has such a long period, the fluctuation of the wave resistance must be associated with the generation of runaway solitons. We observe that the maximum or minimum of C_R occurs when the surface elevation above the leading edge, $x' = 0$, is highest or lowest, respectively.

For the subcritical case (Fn $<$ 1), the difference between a maximum and the following minimum values of C_R decreases as time goes on. This implies that the generation of the runaway solitons may cease after a certain period of time. We also note that the upstream surface level near the leading edge raises to a certain value. The time required to reach such a limiting state becomes longer as Fn approaches 1.

For Fn $\geq$ 1, the difference between a maximum and the following minimum values changes very little as time increases.

This implies that the generation of runaway solitons may continue indefinitely. Based upon the observation of C_R with time described above, we further subdivide Group 3 into Group 3a, Fn = 0.9, 0.95 and Group 3b, Fn = 1.0-1.15.

We may decompose C_R into two components

$$C_R = C_{RS} + C_{RT} , \tag{4.3}$$

where $C_{RS}(t)$ is due to the generation of runaway solitons, and $C_{RT}(t)$ is the rest. $C_{RT}(t)$ can be found approximately by connecting the minima of C_R with a smooth curve. We observe that

$$C_R(t = \infty) = \begin{cases} C_{RT}(t = \infty) & \text{for } Fn < 1. \\ \text{no limiting value} & \text{for } Fn \geq 1. \end{cases} \tag{4.4}$$

For $Fn < 1$, $C_{RT}(t = \infty)$ consists of two parts. One is due to the trailing waves and the other is due to the constant raised water level just ahead of the disturbance. This result seems to agree with what Benjamin (1970) obtained; however, he used the results of linear dispersive theory and his model for the long-time behavior is quite different from what we observe.

As a measure of the work done by the disturbance in generating a runaway soliton, we define W_S as

$$W_S = Fn \int C_{RS}\, dt ,$$

where the integration is taken over the time interval between the two successive minima of the C_R. W_S for the first three runaway solitons at $Fn = 1$ and the total wave energy of the permanent solitary wave, eq. (3.64), of corresponding amplitude, E_T, are presented in Table 4.2. It shows that W_S is somewhat smaller than the corresponding E_T. The reasons for this discrepancy are yet to be understood in relation to the question whether the runaway soliton is really an entity when it emerges from the disturbance region.

From the numerical results for $Fn < 1$, we observe that the wave resistance coefficient averaged over the time interval between the first and the third minimum (or fourth when available), C_{RA}, can be used as an approximate asymptotic limiting value of C_R. In Fig. 4.4.1, we show C_{RA} as a function of Fn for $p_m = 0.05$, 0.1, and 0.15. Because the full linear dispersive theory predicts that the wave elevation becomes unbounded as Fn approaches 1 from below, it is somewhat surprising, at least at first glance, to see a maximum C_{RA} occur around $Fn = 0.6$ rather than 1. However, the wave resistance need not be unbounded, as Fn tends to 1 from below. As shown in the Appendix, according to the linear dispersive theory, the wave resistance coefficient is given by

$$C_R = p_m^2 \sin^2(k/2\epsilon)\,[1 - (k/2\pi\epsilon)^2]^{-2}\,[1 - (2k/\sinh 2k)]^{-1}\,, \tag{4.5}$$

where the dimensionless wave number, k, is determined by the dispersion relation. There are two limiting cases of interest, namely, when Fn approaches zero from above and 1 from below. As can be

easily shown, C_R is bounded for both cases, and the values taken are zero and (3/8) p_m^2/ϵ^2, respectively (see Appendix for details). As C_R for $Fn > 1.0$ is zero in linear dispersive theory, C_R has a finite discontinuity at $Fn = 1$.

In Fig. 4.4.2, C_{RA} is normalized by p_m^2/ϵ^2 for the nonlinear results presented in Fig. 4.4.1 along with the results of linear dispersive theory. The linear dispersive theory predicts a maximum value of C_{RA} at a Fn of about 0.64. We note that the existence of the maxima is due to the finite size of the disturbance. Although the two theories give fundamentally different wave patterns, the agreement in the prediction of the wave resistance coefficient is remarkable over the whole range of Fn. The current nonlinear theory gives a continuous rapid decrease for $Fn \approx 1$. For $Fn > 0.6$, the linear dispersive theory becomes invalid, because the predicted wave amplitude becomes so large that the assumption of the small amplitude is open to question. However, for $0.2 < Fn < 0.6$, it is difficult to say which theory gives the more accurate wave resistance and surface elevation, and it is highly recommended that this issue be resolved experimentally. The existence of the maximum of C_{RA} implies that there may be a critical point near $Fn = 0.6$ around which runaway solitons of noticeable size begin to form and C_{RA} starts to decrease slowly. As the strength of the disturbance increases, the difference between the two theories becomes larger as we would expect, and so does the range of Fn over which the nonlinear theory predicts the nonnegligible values of the wave resistance.

4.1.3 The Basic Mechanism

The basic mechanism of the whole phenomenon is yet to be fully understood; nevertheless, our understanding, so far, can be described as follows. According to the linear dispersive theory the group velocity is slightly less than the phase velocity, whose upper bound is the critical speed. Hence the energy, accumulated with the dispense of the work done by the moving disturbances in its neighborhood, should propagate downstream. This becomes more and more difficult as Fn increases, and consequently the surface elevation near the disturbance becomes unbounded as Fn approaches 1. In the nonlinear theory it is possible for waves to move faster than the disturbance itself. Therefore, some part of the energy propagates upstream, and thus the wave elevation remains bounded as Fn tends to 1.

For $Fn < 0.8$, we observe from the numerical results that the trailing waves are responsible for most of the wave resistance, and that C_{RS} is very small compared to C_{RT}. However, as Fn increases, the runaway solitons become larger, and the depleted region appears. For Fn close to 1, C_{RS} is as big as C_{RT} and the wave amplitude of the runaway solitons is about the same as the wave height of the trailing waves. As Fn further increases, more of the energy propagates upstream than downstream. For Fn greater than 1.25 approximately, the runaway solitons are not fast enough to propagate away from the disturbance, and the waves are localized to the neighborhood of the disturbance.

4.2 Comparison of the Inhomogeneous KdV and Boussinesq Equations

We now compare the solution behavior of the inhomogeneous KdV equation with that of the inhomogeneous Boussinesq equations. As seen from eq. (2.43), the Boussinesq equations differenitiate a moving surface pressure from a moving bottom bump, while the KdV equation does not. As shown in the Appendix, the linear dispersive theory predicts similar wave shapes for both disturbances, but the wave amplitude for the bottom bump is smaller than that due to the surface pressure of equal strength by a factor of $\operatorname{sech} k$. This factor is always less than 1 and approaches 1 as k tends to zero, that is, as Fn tends to 1 from below.

As examples, we take the same cosine function as a disturbance for the surface pressure and the bottom bump, and use p_m or $b_m = 0.1$ with Fn = 0.8, 0.9, 1.0, 1.1. The results of the inhomogeneous KdV and Boussinesq equations are shown in Figs. 4.5.1-4.5.4 and Figs. 4.6.1-4.6.4, respectively.

The main differences are the shape of waves and the number of runaway solitons generated by the end of the computation time. We see that the surface pressure, in the Boussinesq model, acts as a stronger disturbance than the bottom bump, and that the disturbance in the KdV model gives the results between these two. This observation continues to hold in general for a wide variety of values of p_m and b_m. In Figs. 4.7.1-4.7.3, we present the results of the KdV and Boussinesq model for p_m or $b_m = 0.2$ with Fn = 1.

Further discussion of these models and comparison with experimental results will be made after the experimental procedures are described in the next chapter.

V. EXPERIMENTS FOR A BOTTOM BUMP AND THE COMPARISON WITH THE NUMERICAL RESULTS

To aid in evaluating the results from the numerical solution, and to focus directions for future developments, we carried out experiments using a bottom bump moving uniformly along a shallow water tank. The bottom disturbance is preferred to the surface pressure for its ease of construction and implementation. After we observed qualitative agreement between experiments and theory in preliminary experiments, our main efforts were directed toward measuring the wave elevation. Since we knew from the numerical solution that the phenomenon is unsteady, we positioned several wave gages at various locations to detect the evolution of the waves during and after their generation.

5.1 Experiments for a Bottom Bump

5.1.1 Experimental Setup and Measurements

Experiments were conducted in a flume 7.5 m long, 0.75 m wide and 0.6 m deep, constructed of glass. The bottom unevenness of the flume is less than $\pm$ 0.1 cm. A two-dimensional bump 4.9 cm long, 72 cm wide and 0.65 cm high at its mid-chord plane was machined of aluminium. In cross section the bump had a circular arc top and a flat base. To make the bump electrically insulated from the water and wave gages in the tank, the surface of the bump was finished with Krylon Spray Enamel No. 1604. It was positioned just above the floor of the flume with a gap of 0.05 cm at the highest

location of the floor, and was rigidly suspended from a towing carriage by two vertical bars at the channel sides. The carriage ran on wheels along parallel tracks mounted above the flanged top of the side walls. A 1/4 HP DC motor (Bodine NSH-55) was used to move the carriage along the track by means of a cable drive. The carriage speed was controlled remotely with the aid of a Minarik variable speed control (Model W63). The carriage could be brought up to a speed within 60 cm of its rest position and maintained the speed for the length of a data run (4-5 m). The maximum speed obtainable was 150 cm/sec, and the range of the speed used in the experiments was between 40 and 90 cm/sec.

Wave elevations were measured using parallel-wire resistance type wave gages. A drawing of a typical wave gage and the circuit diagram of a full bridge for the wave gages are shown in Figs. 5.1.1, 5.1.2, respectively. Two stainless steel wires of various lengths (4.5-7 cm) with a diameter of 0.16 cm (1/16 in.) were used for a wave gage, and the wires were spaced 0.5 cm apart. A change of wetted length of the wave gage in water causes an imbalance in the pre-balanced bridge circuit and induces an output voltage proportional to the change in submergence depth. A bank of Hewlett-Packard carrier preamplifiers (Model 8805A) provided a 4.5 volt 2400 Hz excitation signal to each bridge. The demodulated and amplified output of these preamplifiers was within $\pm$ 3 volts and single-ended at ground potential. Since the output from the preamplifiers still retained some of the 2400 Hz excitation component, a low-pass filter, RC circuit having a cutoff frequency of 300 Hz, was used to eliminate this noise.

The speed of the carriage was measured by a tachometer in contact with the track. A switch-clock system was also used to obtain an independent measure of the average speed over the range where the speed data obtained by the tachometer were almost constant. A typical shape of the speed vs. time curve (see Fig. 5.1.3) was a steep ramp with a small overshoot at the initial acceleration stage, followed by a desired uniform speed. A block diagram of the experimental set-up is shown in Fig. 5.1.4.

One set of experimental data was obtained from 2 different runs of the bump along the flume. Each run was made at the same speed but in opposite directions. Three wave gages were fixed in the flume as shown in Fig. 5.1.5, and were mounted on a support beam, which was T-jointed AMES angle, and which spanned the entire length of the tank. In this way we obtained wave gage records at 5 fixed locations from 2 runs of the experiment. Since one of the fixed wave gages, FWG, was at the middle of the measuring interval, it was used to check the repeatability of the 2 runs. Another wave gage was mounted on the carriage and moved with the bump. The position of the moving wave gage, MWG, was 1.0 L upstream or 5.0 L downstream from the leading edge of the bump in each run. Thus each set of data consisted of 5 FWG, 2 MWG records and a speed curve, all of which were recorded as a function of time.

5.1.2 Data Acquisition and Experimental Procedure

A Sanborn thermal chart recorder (Model 358-100A) along with a Sanborn low-gain amplifier bank (Model 958-2900) were used for immediate visual inspection of the data. All measurements of wave

elevation and speed was digitized with the Analog-to-Digital (A/D) data acquisition system built into a Digital Equipment Corporation PDP 11/23 computer installed in the laboratory. The digitized values were obtained at a sampling rate of 20 Hz and were converted from integer numbers between 0 and 4096 (12 bit resolution) to real numbers which corresponded to a $\pm$ 5 volts range. The data acquisition was done using a Fortran program which was run through a graphic terminal (Tektronix 4105) next to the tank. An analog back-up of the data was simultaneously recorded on a Hewlett-Packard FM tape recorder (Model 3968A).

As the length of the tank is limited, we had to carefully choose the parameters to make the best use of the given limited facilities. To have at least 2 runaway solitons generated by the end of the experiment, the bump needed to travel about 100 times its length. Because we could obtain useful data for only 5 m of the flume, the upper bound of the bump length was about 5 cm. In the preliminary experiments with $b_m > 0.3$, we observed that the troughs of the waves running ahead of the bump were 20-30 % of the water depth above the undisturbed water surface. Hence the upstream wave structure resembles the bore model in the theory of hydraulic jumps, where the nonlinear effects dominate the dispersive effects. Therefore we decided to use $b_m < 0.2$, and then the dimensionless parameters α, β determined the bump height and the range of water depths. In the experiments ϵ ranged from 0.8 to 1.1 and b_m ranged from 0.12 to 0.16. For each water depth, tests were done for $0.6 < Fn < 1.3$.

A complete list of the parameters used in the experiments is given in Table 5.1.

Calibration of wave gages was done before and after the experiments for each water depth case. From each calibration a proportional conversion constant was obtained by using a least-square fit and the average of two was used for the experimental data obtained between two calibrations. The calibration range was typically $\pm$ 2 cm, and the error in the least-square fit was typically 2-3 % for the values at the end of calibration interval. Since the two calibration constants differed by less than 5 %, the error range can be estimated as about 5 % for the highest waves measured in the experiments. While we were preparing for the next run, experimental data were processed and the surface elevations and the speed record were plotted on the graphic terminal in terms of dimensionless variables.

5.2 Comparison of Experimental and Numerical Results

5.2.1 Numerical Simulation

To more accurately interpret any comparison between the experimental data and the numerical results, we need to consider the effects, which are neglected in the mathematical model but exist in the experiments.

First, we consider the effects of viscosity. For long waves, energy dissipation occurs mainly due to bottom friction. It is sufficient to estimate the attenuation of runaway solitons, because they should suffer most wave attenuation. We adopt the empirical formula suggested by Daily and Stephan (1952) for the attenuation of a solitary

wave in a channel with smooth side walls and bottom. It is given in dimensional form as

$$a/h_o = (a_o/h_o)[1 + (a_o/h_o)^{1/4} C_1 (x_t/h_o)]^{-4} , \qquad (5.1)$$

where

$$C_1 = (1/20)[1 + (2h_o/B)][\nu/(gh_o^3)^{1/2}]^{1/2} ,$$

and a_o is the initial amplitude of the solitary wave, a the attenuated amplitude, B the width of the channel, ν the kinematic viscosity of the fluid and x_t is the distance traversed by the solitary wave. Typical values can be chosen as follows:

$$a_o/h_o = 0.5,\ h_o/B = 1/15,\ \nu = 0.01\ cm^2/sec,\ x_1/h_o = 50,\ h_o = 5\ cm,$$

and give an attenuation factor Ω

$$\Omega = (a_o - a)/a_o = 5\text{-}6\ \% ,$$

which is an approximate estimate for the first runaway soliton at the end of the experiments. Thus we may conclude that the effect of wave attenuation included in the experimental data is small.

The presence of a viscous boundary layer around the bump may increase the effective strength of the bump. As a rough estimate we can use the displacement thickness of a flat plate in steady laminar flow (typical Reynolds number is 3.5×10^4), which is given in dimensional form as (see Schlichting (1979)),

$$\delta_1 = 1.72(\nu x/U)^{1/2} . \qquad (5.2)$$

Taking $x = 5$ cm and $U = 40$ cm/sec, we obtain

$$\delta_1 = 0.05 \text{ cm} .$$

Therefore, the displacement thickness near the trailing edge is about the same as the clearance between the bump and the channel floor. As stated in Section 5.1.1, bottom unevenness was $\pm$ 0.1 cm, which is not negligible compared to the bump height, 0.65 cm. For the numerical simulations, we assumed that the bottom was flat at its mean position and that there was no net flow between the base of the bump and the channel floor, and we neglect the effects of viscosity at the top of the bump. In an attempt to account for bottom unevenness, the bottom-bump clearance, and presence of a viscous boundary layer, an effective bump height of 0.8 cm was used instead of the actual bump height of 0.65 cm. Using the effective bump height, 0.8 cm, the new range of b_m is from 0.15 to 0.2; that is, we increase b_m by 0.03-0.04.

As the width of the tank is finite, there is an edge effect. Considering that the aspect ratio (width/length) of the bump is about 15, we may also conclude that the assumption of one horizontal dimension is valid. Wave elevations were measured at points as close as possible to the longitudinal center plane.

Another difference between the experiments and the mathematical model is that it takes a finite amount of time to reach a uniform speed in the experiments, while in the theory we assume the uniform motion is reached instantaneously. As the distance traveled by the bump is integration of the speed with respect to time, the difference

in the initial acceleration makes the position of the bump given by the theory different from that in the experiments. Since the position of the bump is a key to the phase of the wave system, we modified the numerical scheme to solve an unsteady motion problem and used the experimentally obtained speed record at the initial acceleration stage as an input to the numerical simulation.

5.2.2 Comparison with the Boussinesq Model

Experimental data along with the numerical solutions predicted by the Boussinesq model are shown in Figs. 5.2.1-5.2.20 for $b_m = 0.15, 0.166, 0.185, 0.2$, and for each b_m, cases of $F_n = 0.7, 0.8, 0.9, 1.0, 1.1$ are presented. The solid line is used for the numerical solution and the dotted line for the experimental data. Each figure consists of 10 curves. The first two curves are numerically obtained snapshots at time $T = T_1$ and T_2 where T_2 corresponds to the final instant for each experiment and $T_1 = T_2/2$. The next two curves are from the MWG's, and show the generation of runaway solitons and the development of the depleted region in the moving frame. The next curve gives the numerically obtained wave resistance coefficient. The last 5 curves are from the FWG's, and show the comparison of experimental and numerical results of the evolution of the whole wave system in the fixed frame of reference.

First let's look at the case $b_m = 0.15$, Figs. 5.2.1-5.2.5. Now, we may divide the range of Fn into three Groups A, B and C. For Group A (Fn = 0.72, 0.79) the number of waves running ahead and their amplitude are in good agreement with the theory. For trailing waves, the agreement is good at the initial stage;

however, it becomes poorer as time goes on. We observe that the numerical solution gives higher waves in the trailing region, and that the experimental FWG records show a decrease in the amplitude of the first trailing wave as time goes on. As trailing waves become more steepened, they begin to break in the experiments, and consequently move more slowly. For Group B ($F_n = 0.89, 1.01$) all the features noted in the previous chapter, namely, the runaway solitons, the depleted region and the trailing waves, are exhibited by both results, and their quantitative agreement in terms of both the magnitude and the phase of waves is surprisingly good; however, we notice that slightly bigger and more runaway solitons are generated in the experiments. For Group C (Fn = 1.11) the surface depression in the depleted region is in good agreement; however, the amplitude of runaway solitons is underpredicted by the numerical solution.

As b_m increases, the descriptions given above continue to hold in general. The agreement between theory and experiments remains good in upstream waves for Group A, in the entire region for Group B and in the downstream waves for Group C. For the trailing waves of Group A, the numerical solution predicts higher amplitude waves, and wave breaking was observed in the experiments. For runaway solitons and the trailing waves of Group B, the numerical solution gives slightly fewer and smaller amplitude waves than the experimental data. For runaway solitons in Group C, experimental results show larger amplitude for small b_m, and smaller amplitude for large b_m. For stronger disturbances, breaking of runaway solitons was observed soon after their emergence from the disturbance

region. From the FWG records for cases $b_m = 0.185,\ 0.2$ in Figs. 5.2.15 and 5.2.20, we observe that the amplitude of the first soliton in the record of FWG at $x = -74.1$ is smaller than that in FWG at $x = -57.1$, which indicates that wave breaking occurred between these two FWG's. As b_m increased, the range of Fn for which no wave breaking was observed narrowed.

We recall the amplification of runaway solitons discussed in Section 4.1.1 as they propagate upstream. During the experiments, we often observed that a clean runaway soliton was formed near the disturbance, and then, as it propagated upstream, it started to break some time after it left the disturbance region. This supports the idea that runaway solitons are still evolving as they move ahead of the disturbance.

Due to the limited length of the tank it is difficult to confirm the supposition that these runaway solitons will be generated without end for $Fn \geq 1$. However, based upon the agreement between the experimental data and the numerical results, we may conclude that the generation of the runaway solitons for $Fn \geq 1$ will last for a very long time, at least for the range of parameters used in these experiments. For $Fn < 1$, it seems that the limiting state is approached in a much shorter (finite) time.

Related to the wave breaking observed in the trailing waves, it is certain that the wave resistance of a finite disturbance moving with speed corresponding to $0.7 \leq Fn \leq 0.8$ must include the breaking effect, as the wave breaking changes the wave field significantly.

5.2.3 Comparison with the KdV Model

From the discussion in Section 4.2, we learned that the bottom bump in the KdV model acts as a stronger disturbance than a corresponding bump in the Boussinesq model. The discussion in the previous section indicates that the Boussinesq model gives fewer and smaller waves than the experimental results for most cases with the exception of regions where wave breaking occurs. Thus, it remains to be seen which of the models will predict more closely the experimental results.

To show the differences between the results of two models, we present the comparison of the results of KdV model and the experimental data for the two extreme cases, $b_m = 0.15$ and 0.2 in Figs. 5.3.1-5.3.10. Let us first look at the case $b_m = 0.15$. For Group A (Fn = 0.72, 0.79), the KdV model predicts larger upstream waves than the experimental results, and bigger waves in the trailing region than the Boussinesq model. For Group B (Fn = 0.9, 1.01) the agreement is excellent everywhere. The solution of the KdV model is only slightly less than the experimental data, and is closer to the experimental results than the results of the Boussinesq model. For Group C (Fn = 1.11) the depressed wave is in good agreement, and the amplitude of the runaway solitons is underpredicted by the KdV model. Again, the results of the KdV model are in closer agreement with the experiments. For the case $b_m = 0.2$, we see that the KdV model gives more and larger runaway solitons than the experimental results for all Froude numbers.

In summary, both the Boussinesq and the KdV model predict less than the experimental data in most cases for weaker disturbance.

The solution of the KdV model becomes larger than the experimental results as the disturbance becomes stronger. Considering the effects present in the experiments such as viscosity, bottom unevenness, and bottom-bump clearance, it is difficult to say definitely which model performs better. However, it seems that the KdV model is no less competent in its performances than the Boussinesq model for the range of parameters tested in the present study; thus, we may conclude that the KdV model is suitable in future analytical treatment for $Fn \approx 1$, because it gives all the basic features of the solution and because it is simpler.

VI. SUMMARY AND CONCLUSIONS

In this thesis, several models of nonlinear dispersive long-wave equations, which are uniformly valid in space and time, were derived when external forcing agencies were present. In particular, a moving surface pressure and a moving bottom bump were studied in detail. All of the derived equations belong to the same class as the original Boussinesq equations or the KdV equation. The Boussinesq model was formulated under the assumption that the disturbance is of $O(\alpha)$ and no explicit restrictions were placed on the speed of the disturbance. The inhomogeneous KdV equation was derived under the more restrictive assumptions that the strength of the disturbances is of $O(\alpha\beta)$, and that the speed of the moving disturbance is close to the critical speed. The surface pressure and the bottom bump appear in the same fashion in the KdV model, while they show slight differences in the Boussinesq model.

Employing a predictor-corrector method, numerical procedures were developed to solve the inhomogeneous KdV equation and the pair of coupled inhomogeneous Boussinesq equations. The numerical scheme is implicit for the KdV model and mixed explicit-implicit for the Boussinesq model. To deal with the moving disturbance, a pseudo-moving frame and sufficiently 'transparent' open boundary conditions have been devised and they are successful in rendering the region of computation reasonably small.

Using the numerical method developed for the Boussinesq model, the surface elevations and the wave resistance coefficient

were computed for a cosine surface pressure moving uniformly with the depth-Froude-number, Fn, ranging from 0.1 to 1.3. In contrast to the results of linear dispersive theory, the present numerical results for the water surface wave elevation exhibit a series of positive waves running ahead of the disturbance for Fn ranging from 0.25 to 1.25. These forward propagating solitary waves are especially well defined for $Fn \approx 1$. To distinguish the salient features of the resulting wave field, the range of Fn can be divided into 4 groups: For Group 1 ($Fn \leq 0.2$) and Group 4 ($Fn \geq 1.25$), the effects of the moving disturbance are localized to its neighborhood only. For Group 2 ($0.2 < Fn \leq 0.85$), the trailing waves reach a steady state soon after the motion starts; however, a series of positive waves moves ahead of the disturbance, though their amplitude is very small compared to that of the trailing waves. For Group 3 ($0.85 < Fn < 1.25$), the upstream running positive waves become large and comparable to the trailing waves in their magnitude, and we have a slowly prolonging negative wave of nearly constant displacement between the disturbance and the trailing waves, which is a train of modulated cnoidal waves. We may further subdivide Group 3 into Group 3a ($0.85 < Fn < 1$) and 3b ($1 \leq Fn < 1.25$). For Group 2 and 3a, there seems to be an end of the generation of the waves running ahead, and the upstream surface level near the leading edge of the disturbance rises to a certain constant value. For Group 3b the generation of the runaway soliton seems to continue indefinitely.

Using linear dispersive theory, the wave resistance coefficient was computed for the same cosine surface pressure disturbance as

used before, and its value was found to be bounded for all Froude numbers and has a finite discontinuity at $Fn = 1$. The numerically obtained wave resistance coefficient was averaged over time, and compared to the results predicted by linear dispersive theory. The results of the current nonlinear theory are larger for $0.2 < Fn < 0.6$ and smaller for $0.6 < Fn < 1.0$ than those given by linear dispersive theory, and they exhibit a continuous rapid decrease for $Fn \geq 1$. With the same cosine distribution for the surface pressure and the bottom bump, computations were done using the KdV and the Boussinesq models, and the results of the two models were compared. In the Boussinesq model, the surface pressure acts as a stronger disturbance than the bottom bump, and the disturbance in the KdV model gives results intermediate to the two Boussinesq results.

Experiments were conducted in a shallow water tank using a bottom bump moving uniformly with Fn ranging from 0.6 to 1.3. Wave elevations were measured by a set of resistance type wave gages installed both in a moving and in a fixed reference frame. Experimental data were compared with the results predicted by the Boussinesq model. The numerical results and the experimental measurements are in good agreement for the upstream waves of Group A ($Fn = 0.7, 0.8$), for the entire wave field of Group B ($Fn = 0.9, 1.0$) and for the downstream waves of Group C ($Fn = 1.1$). For the trailing waves of Group A, the numerical results predict waves with higher amplitude than those measured, and wave breaking was observed in the experiments. For runaway solitons in Group C, experimental data show larger amplitude for weak disturbances and smaller

amplitude for strong disturbances relative to the numerical prediction of nonlinear theory. For sufficiently strong disturbances, breaking of runaway solitons was observed soon after their emergence from the disturbance region.

The numerical solutions of the KdV model were also computed for comparison. Over the range of the parameters used in the current study, the difference between the results predicted by the two models are about the same as that between the experimental data and the results predicted by either of the two models. The KdV model seems to have advantages for future analytical treatment for $Fn \approx 1$, because it is capable of predicting all the basic features of the solution and because it offers a simpler formulation.

APPENDIX

Linear dispersive theory is well described in textbooks such as Lamb (1932), Stoker (1957), Whitham (1974) and Lighthill (1978). When a uniformly moving disturbance is present, the surface elevation can be obtained by solving either an initial value problem or a proper boundary value problem under the assumption that a steady state exists. Here, we shall follow Lamb (1932) who takes the latter approach, and we will quote the results without providing the intermediate steps. The relevant sections are 245, 246, and 249 for a moving surface pressure, a moving bottom bump and the wave resistance, respectively. Dimensional quantities will be used until final results are obtained.

The wave resistance, R, experienced by a disturbance moving uniformly with a subcritical speed, $U < c_o$, is given by (Section 249)

$$R = [1 - (C_g/U)]E \ , \qquad (A.1)$$

where C_g is the group velocity, and E is the mean wave energy per unit area of the free surface. C_g is given by

$$C_g = \frac{U}{2} [1 + (2kh_o/\sinh 2kh_o)] \ , \qquad (A.2)$$

where the wave number, k, is determined by the dispersion relation

$$(U/c_o)^2 = \tanh kh_o/kh_o \ , \qquad c_o = (gh_o)^{1/2} \ . \qquad (A.3)$$

We note that the wave number depends on the speed of the disturbance only aside from the water depth h_o. E is given by

$$E = \frac{1}{2} \rho g A^2 , \qquad (A.4)$$

where A is the amplitude of the stationary waves far downstream. Substituting eqs. (A.2) and (A.4) into (A.1) the wave resistance can be rewritten as

$$R = \frac{1}{4} \rho g A^2 [1 - (2kh_o / \sinh 2kh_o)] . \qquad (A.5)$$

Therefore, once k is determined by eq. (A.3), we only need to know A to obtain the wave resistance.

Using the Fourier's method, for a moving surface pressure such that

$$p_o(x') = P_1 \delta(x'), \quad x' = x + Ut, \quad \text{and} \quad U < c_o , \qquad (A.6)$$

where δ is the delta function, the surface wave elevation is given by (Section 245)

$$\zeta = \begin{cases} -(2P_1/\rho U^2) M(kh_o) \sin kx' + O[\exp(-kx')], & x' > 0 \\ O[\exp(kx')] , & x' < 0 , \end{cases} \qquad (A.7)$$

where

$$M(\xi) = 2\sinh^2 \xi / (\sinh 2\xi - 2\xi) . \qquad (A.8)$$

To generalize this result to a disturbance prescribed by an arbitrary function, we need to replace $(i/\pi)P_1 \sin kx'$ by $\Gamma(k, x')$ (see Lighthill (1979)),

$$\Gamma = [P(k)\exp(ikx') - P(-k)\exp(-ikx')] ,$$

where $P(\kappa)$ is the Fourier transform of $p_o(x')$ defined as

$$P(\kappa) = (1/2\pi)\int_{-\infty}^{\infty} p_o(x')\exp(-i\kappa x')dx' \quad , \tag{A.9}$$

and $i = (-1)^{1/2}$. Since $P(-\kappa)$ is the complex conjugate of $P(\kappa)$, Γ can be rewritten as

$$\begin{aligned} \Gamma &= 2i\ \mathrm{Im}[P(k)\exp(ikx')] \quad , \\ &= 2i\ \mathrm{mod}[P(k)]\ \sin(kx' + \arg[P(k)]) \quad , \end{aligned} \tag{A.10}$$

where Im stands for the imaginary part, mod for the modulus and arg for the argument of the complex function, respectively. Hence the amplitude of the waves far downstream for an arbitrary shaped disturbance, A_p, becomes

$$A_p = (4\pi/\rho U^2)M(kh_o)\ \mathrm{mod}[P(k)] \quad . \tag{A.11}$$

As U approaches c_o from below, kh_o tends to zero, and $\mathrm{mod}[P(k)]$ tends to the area of the disturbance, which is the integration of $p_o(x')$ with respect to x' over the length of the disturbance. Therefore, as U approaches c_o from below, A_p tends to infinity, since $M(\xi)$ is singular at $\xi = 0$.

The cosine pressure distribution used in the numerical computation can be written in terms of the dimensional quantities as

$$p_o(x') = \begin{cases} (p_m/2)(1 - \cos \mu x'), & 0 \le x' \le L \\ 0, \quad \text{otherwise}, \end{cases} \tag{A.12}$$

where

$$\mu = (2\pi/L) \quad . \tag{A.13}$$

Its Fourier transform at $\kappa = k$ is given by

$$P(k) = (ip_m/4\pi)[1 - \exp(-ikL)][\mu^2/k(k^2 - \mu^2)] \quad . \qquad (A.14)$$

Therefore, A_p becomes

$$A_p = (2p_m/\rho U^2)M(kh_o)\sin(kL/2)[\mu^2/k(k^2 - \mu^2)] \quad . \qquad (A.15)$$

We note that A_p is zero if L is any integer multiple of the wavelength, $(2\pi/k)$, of the waves far downstream. In other words, there are some particular Fn's at which no waves are generated far downstream for a fixed L. Substituting eq. (A.15) into eq. (A.5), and making use of eqs. (A.3) and (A.8), the wave resistance is obtained as

$$R = (p_m^2/\rho g)\sin^2(kL/2)[1 - (k/\mu)^2]^{-2}\,[1 - (2kh_o/\sinh 2kh_o)]^{-1} \quad . \qquad (A.16)$$

Similarly, for the moving bottom bump

$$b(x') = B_1\delta(x') \quad , \qquad (A.17)$$

the surface wave elevation is given by (Section 246)

$$\zeta = \begin{cases} -(2B_1/h_o)N(kh_o)\sin kx' + O[\exp(-kx')] \quad , & x' > 0 \\ O[\exp(kx')] \quad , & x' < 0 \quad , \end{cases} \qquad (A.18)$$

where

$$N(\xi) = (\xi/\sinh\xi)M(\xi) \quad . \qquad (A.19)$$

We define dimensionless variables as follows

$$x'^* = x'/h_o, \quad k^* = kh_o, \quad p_m^* = p_m/\rho g h_o ,$$
$$P_1^* = P_1/\rho g h_o^2 , \quad B_1^* = B_1/h_o^2 , \tag{A.20}$$

and in the sequel we omit the asterisk * for brevity.

From eq. (A.14) we find the wave resistance coefficient C_R in terms of dimensionless variables as

$$C_R = p_m^2 \sin^2(k/2\epsilon)[1-(k/2\pi\epsilon)^2]^{-2}[1-(2k/\sinh 2k)]^{-1} , \tag{A.21}$$

which is the eq. (4.5). The dispersion relation, (A.3), can be re-written in terms of the dimensionless variables as

$$Fn^2 = \tanh k/k . \tag{A.22}$$

It is clear that, as Fn tends to zero from above, k approaches infinity. Therefore, C_R approaches zero as Fn tends to zero from above. As Fn approaches 1 from below, k tends to zero, and $\sin^2(k/2\epsilon)$ and $1-(2k/\sinh 2k)$ have the same behavior; namely, both terms are proportional to k^2, which renders C_R bounded. Hence we have

$$\lim_{Fn\to 1^-} C_R = \frac{3}{8}(p_m/\epsilon)^2 . \tag{A.23}$$

To compare the wave elevation due to a surface pressure to that generated by a bottom bump, we consider the dimensionless form of eqs. (A.7) and (A.18) for $x' > 0$. From eq. (A.7) we obtain

$$\zeta = -2P_1 \, Fn^{-2} M(k) \sin(kx') + O[\exp(-kx')], \quad \text{for } x' > 0 \ . \tag{A.24}$$

Similarly from eq. (A.18) we find

$$\zeta = -2B_1 N(k) \sin(kx') + O[\exp(-kx')] , \quad \text{for } x' > 0 \ . \tag{A.25}$$

Therefore, if $P_1 = B_1$, using eqs. (A.17) and (A.22), the ratio of the amplitudes, σ_o, at far downstream for the surface pressure and the bottom bump becomes

$$\sigma_o = Fn^{-2} \, (k/\sinh k) \ ,$$

$$= \cosh k \ . \tag{A.24}$$

This indicates that the wave amplitude due to the surface pressure is always larger than that due to the bottom bump, and that both disturbances generate similar waves as Fn approaches 1 from below, if both disturbances assume the identical functional distribution.

REFERENCES

Akylas, T. R. 1984 On the excitation of long nonlinear water waves by a moving pressure distribution. J. Fluid Mech. vol. 141, pp. 455-466.

Benjamin, T. B. 1970 Upstream influence. J. Fluid Mech. vol. 40, pp. 49-79.

Boussinesq, J. 1872 Théorie des ondes et des remous qui se propagent le long d'un canal rectangulaire horizontal, en communiquant au liquide contenu dans ce canal des vitesses sensiblement pareilles de la surface au fond. J. Math. Pures Appl. vol. 17, pp. 55-108.

Cole, S. L. 1985 Transient waves produced by flow past a bump. To appear in Wave Motion.

Daily, J. W. and Stephan, Jr., S. C. 1952 The solitary wave-its celerity, profile, internal velocities and amplitude attenuation. Hydro. Lab., Dept. of Civil Engng., Massachusetts Institute of Technology Tech. Rep. No. 8.

Huang, De-Bo, Sibul, O. J. and Wehausen, J. V. 1982 Ships in very shallow water. Festkolloquium-Dedication to Professor Karl Wieghardt. March 1982, Institute fur Schiffbau der Universitat Hamburg.

Kelvin, Lord 1886 On stationary waves in flowing water II. Phil. Mag. vol. 22, pp. 445-452.

Korteweg, D. J. and de Vries, G. 1895 On the change of form of long waves advancing in a rectangular channel, and on a new type of long stationary waves. Phil. Mag. vol. 39, pp. 422-443.

Lamb, H. 1932 Hydrodynamics, 6th Ed., Cambridge Univ. Press. pp. 398-416.

Lepelletier, T. G. 1981 Tsunamis-harbor oscillations induced by nonlinear transient long waves. Ph. D. Thesis, California Institute of Technology, Pasadena, CA.

Lighthill, J. 1978 Waves in Fluids. Cambridge Univ. Press, pp. 260-269, 464-466.

Rayleigh, Lord 1876 On waves. Phil. Mag., vol. 1, pp. 257-279.

Russell, J. S. 1838 Report of the Committee on Waves. Rep. Meet. Brit. Assoc. Adv. Sci., 7th, Liverpool, 1837, John Murray:London, pp. 417-496.

Russell, J. S. 1845 Report on Waves. Rep. Meet. Brit. Assoc. Adv. Sci. 14th, York, 1844, John Murray:London, pp. 311-390.

Schember, H. R. 1982 A new model for three-dimensional nonlinear dispersive long waves. Ph. D. Thesis, California Institute of Technology, Pasadena, CA.

Schlichting, H. 1979 Boundary Layer Theory, 7th Ed., McGraw-Hill:New York, N. Y., pp. 127-149.

Stoker, J. J. 1952 Some remarks on radiation conditions. Proc. Sym. Appl. Math., vol. 5, pp. 97-102.

Stoker, J. J. 1957 Water Waves. Interscience:New York, pp. 198-218.

Thews, J. G. and Landweber, L. 1935 The influence of shallow water on the resistance of a cruiser model. U. S. Experimental Model Basin, Navy Yard, Washington, D. C. Rep. No. 408.

Ursell, F. 1953 The long-wave paradox in the theory of gravity waves. Proc. Camb. Phil. Soc., vol. 49, pp. 685-694.

Whitham, G. B. 1974 Linear and Nonlinear Waves. John Wiley & Sons, Inc., New York, N. Y., pp. 460-466.

Wu, T. Y. 1979 On tsunamis propagation-evaluation of existing models. Tsunamis-Proc. of the National Science Foundation Workshop, organized and edited by Hwang, L. S. and Lee, Y. K., Tetra Tech Inc., Pasadena, CA, pp. 110-149.

Wu, D-M, and Wu, T. Y. 1983 Three-dimensional nonlinear long waves due to moving surface pressure. Proc. 14th Sym. Naval Hydro., National Academic Press, Washington, D. C., pp. 103-125.

TABLE 3.1

Amplification Factor Λ for the KdV Equation

t	$\Delta x = \Delta t = 0.1$		$\Delta x = \Delta t = 0.05$	
	peak value	$\Lambda(t)$ %	peak value	$\Lambda(t)$ %
0	0.3000	0	0.3000	0
10	0.3030	1.00	0.3005	0.17
20	0.3045	1.50	0.3008	0.27
30	0.3056	1.87	0.3009	0.30
40	0.3074	2.47	0.3011	0.37
50	0.3090	3.00	0.3012	0.40
60	0.3100	3.33	0.3014	0.47
70	0.3120	4.00	0.3016	0.53
80	0.3133	4.43	0.3018	0.60

TABLE 3.2

Amplification Factor Λ for the Boussinesq Equations

t	$\Delta x = \Delta t = 0.1$		$\Delta x = \Delta t = 0.05$	
	peak value	$\Lambda(t)$ %	peak value	$\Lambda(t)$ %
0	0.3000	0	0.3000	0
10	0.3151	5.03	0.3097	3.20
20	0.3191	6.37	0.3112	3.73
30	0.3213	7.10	0.3117	3.90
40	0.3240	8.00	0.3122	4.07
50	0.3266	8.87	0.3124	4.13
60	0.3282	9.40	0.3125	4.17
70	0.3308	10.27	0.3128	4.27
80	0.3315	10.50	0.3131	4.37

TABLE 4.1

Parameters used in the Numerical Computation

for the Cosine Surface Pressure of $p_m = 0.1$

$p_m = 0.1, \epsilon = 0.5$							
F_n	$-x_0$	x_N	Δx	J	Δt	K	d_K^*
0.1	10	10	0.1	20	0.050	1000	5
0.2	10	10	0.1	10	0.050	500	5
0.3	10	10	0.1	6	0.056	300	5
0.4	10	20	0.1	5	0.050	250	5
0.5	20	20	0.2	4	0.100	400	20
0.6	20	25	0.2	3	0.111	300	20
0.7	15	25	0.2	3	0.095	450	30
0.8	20	25	0.2	3	0.083	600	40
0.85	20	25	0.2	2	0.118	750	75
0.9	20	25	0.2	2	0.111	750	75
0.95	20	25	0.2	2	0.105	1000	100
1.0	20	25	0.2	2	0.100	1000	100
1.05	20	25	0.2	2	0.095	1000	100
1.1	20	25	0.2	2	0.091	1500	150
1.15	20	30	0.2	2	0.087	1500	150
1.2	10	20	0.2	2	0.083	1000	100
1.3	10	20	0.2	2	0.077	1000	100

*d_K is given by $d_K = K\Delta x/J$, and is the distance traveled by the disturbance by the end of computation, $t = K\Delta t$.

TABLE 4.2

Comparison between W_S and E_T of the First Three Runaway Solitons for Fn = 1

	W_S	E_T
1st	0.1036	0.1370
2nd	0.1027	0.1340
3rd	0.1058	0.1389

TABLE 5.1

Parameters used in the Experiments

for the Bottom Bump

b_m = 0.65 cm, L = 4.9 cm

h_o(cm)	b_m/h_o	$(b_m/h_o)^*$	F_n**
4.0	0.163	0.200	0.7, 0.8, 0.9, 1.0, 1.1, 1.2
4.33	0.150	0.185	0.7, 0.8, 0.9, 1.0, 1.1
4.83	0.135	0.166	0.7, 0.8, 0.9, 1.0, 1.1, 1.2
5.33	0.122	0.150	0.7, 0.8, 0.9, 1.0, 1.1, 1.2

*effective bump height b_m = 0.8 cm is used.

**with the error of $\pm$ 0.02

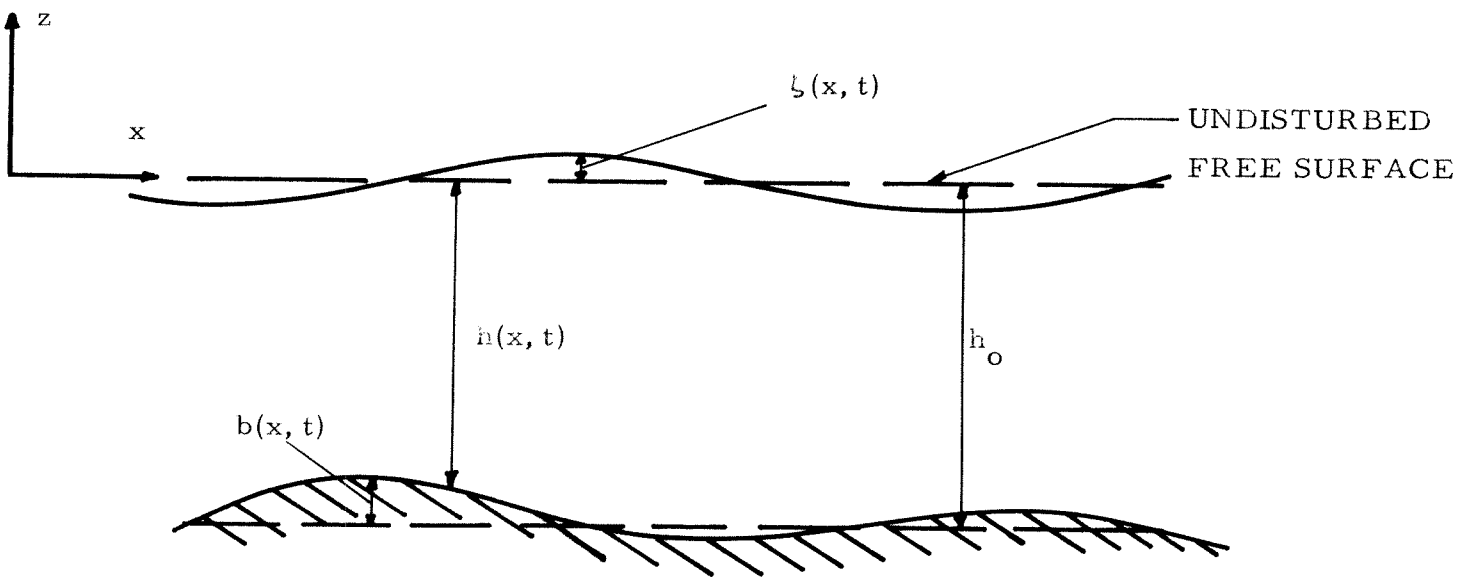

Fig. 2.1. Definition sketch for the derivation of the governing equations.

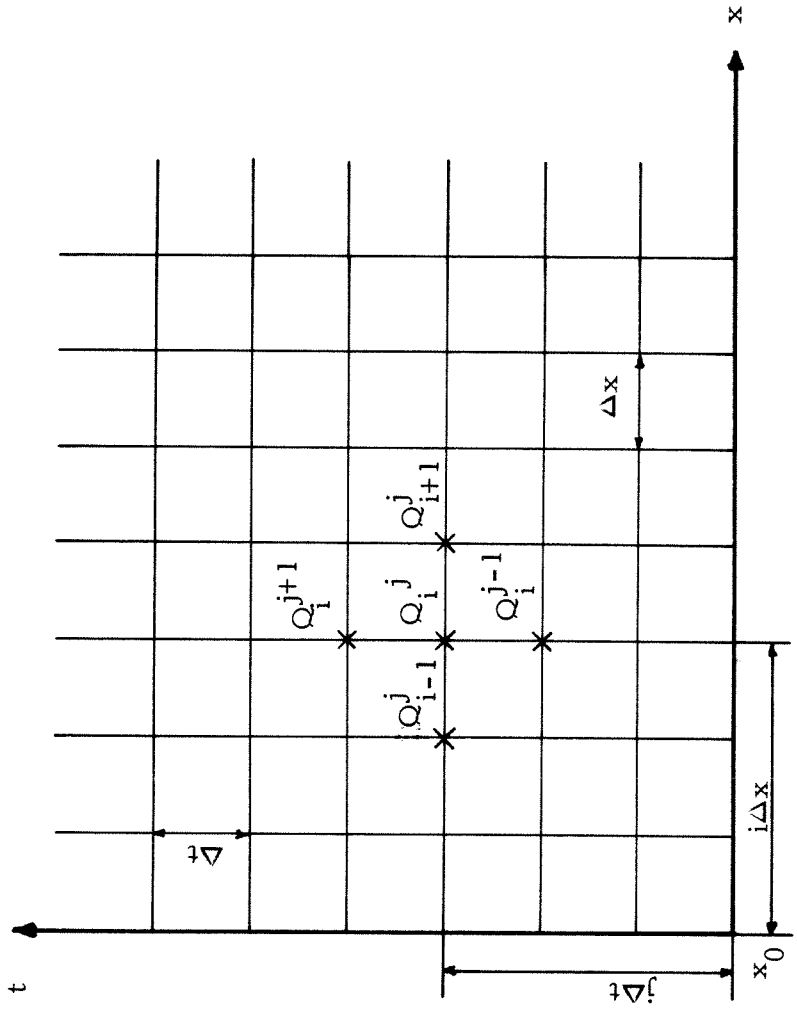

Fig. 3.1. Definition sketch for the numerical methods.

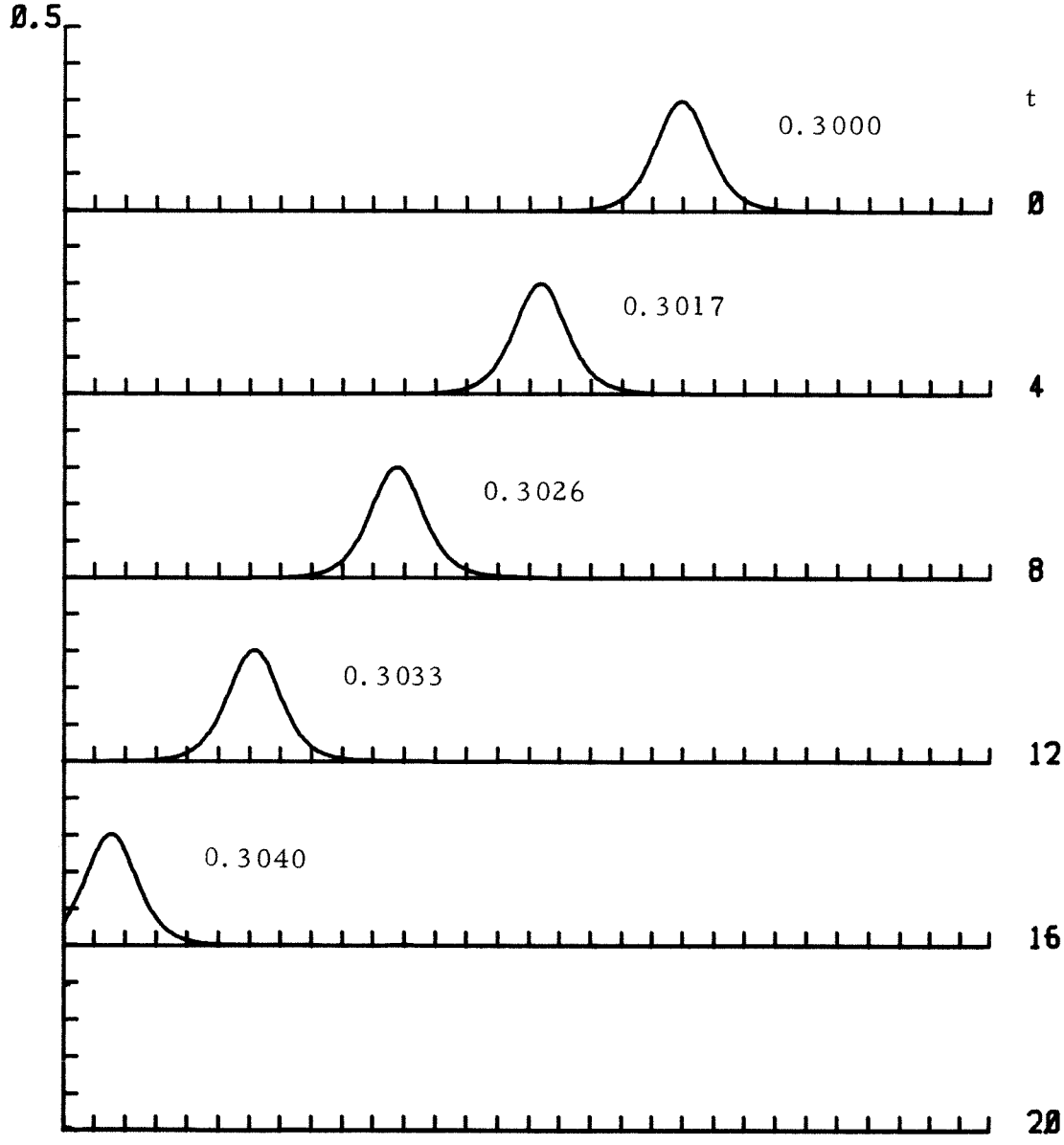

Fig. 3.2. Stability test of the numerical KdV model using the solitary wave as initial condition, $a_o = 0.3$.

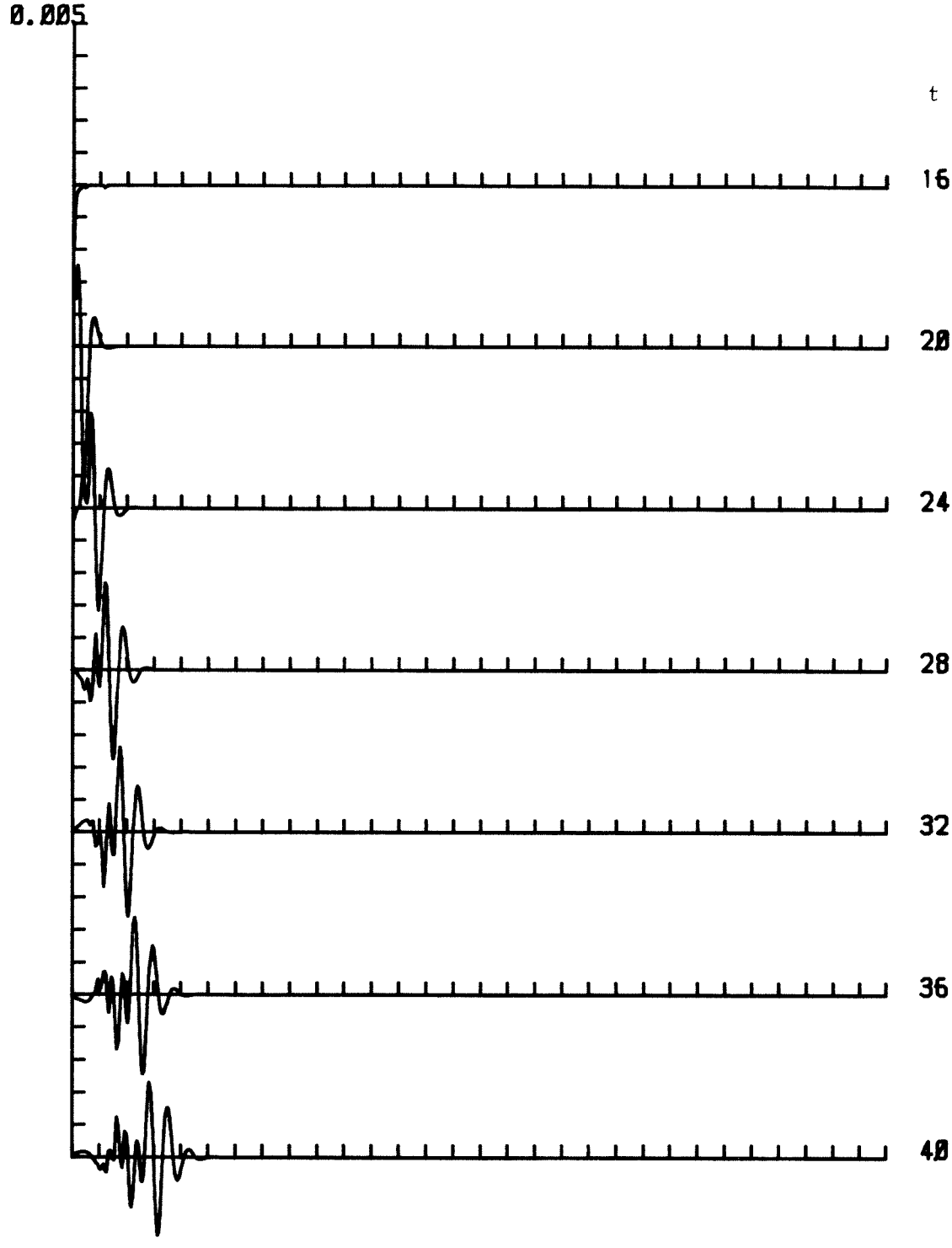

Fig. 3.3. Test of the boundary condition for the numerical KdV model using the solitary wave as initial condition, $a_o = 0.3$, with two different window sizes.

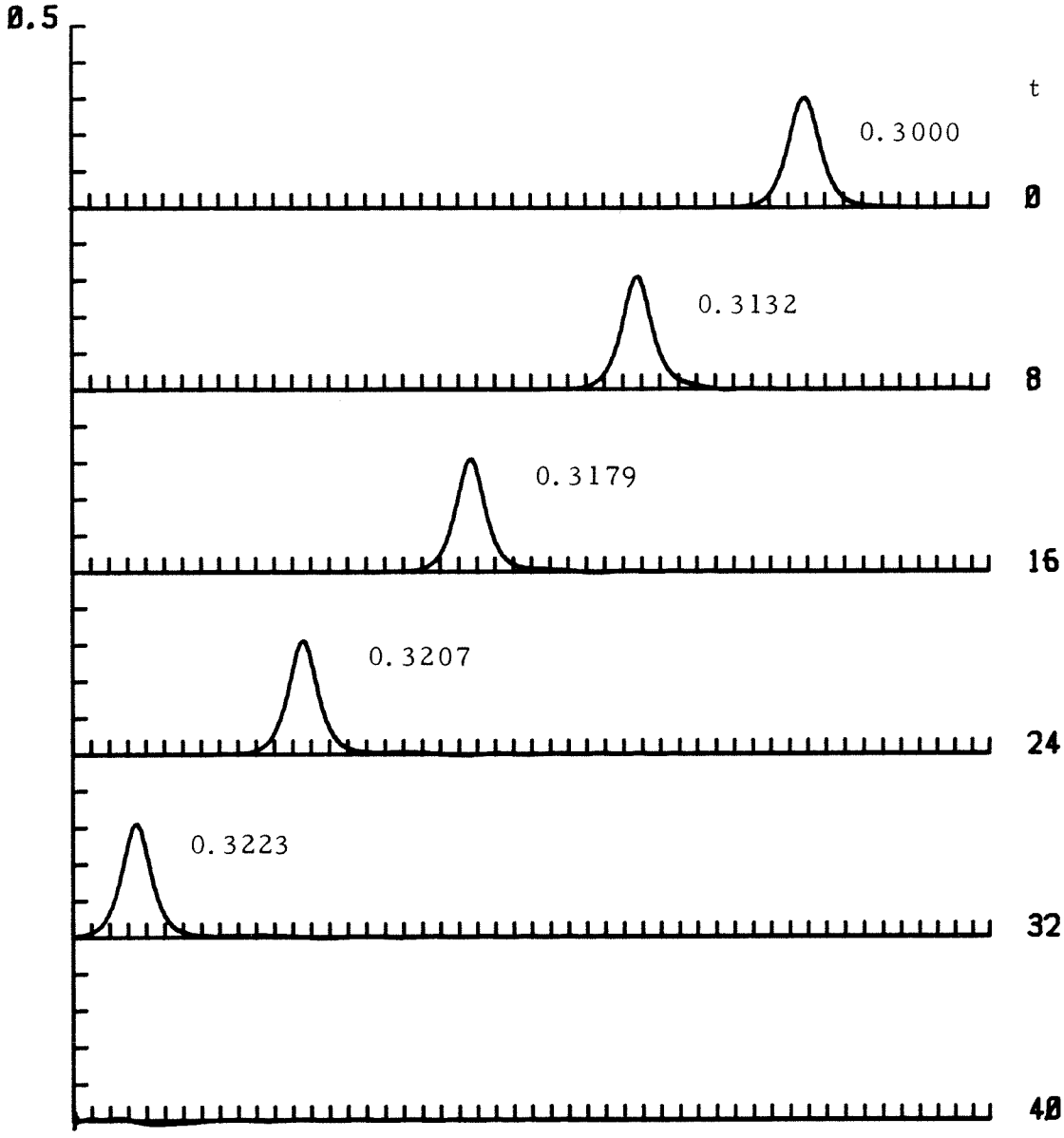

Fig. 3.4 Stability test of the numerical Boussinesq model using the solitary wave as initial condition, $a_B = 0.3$.

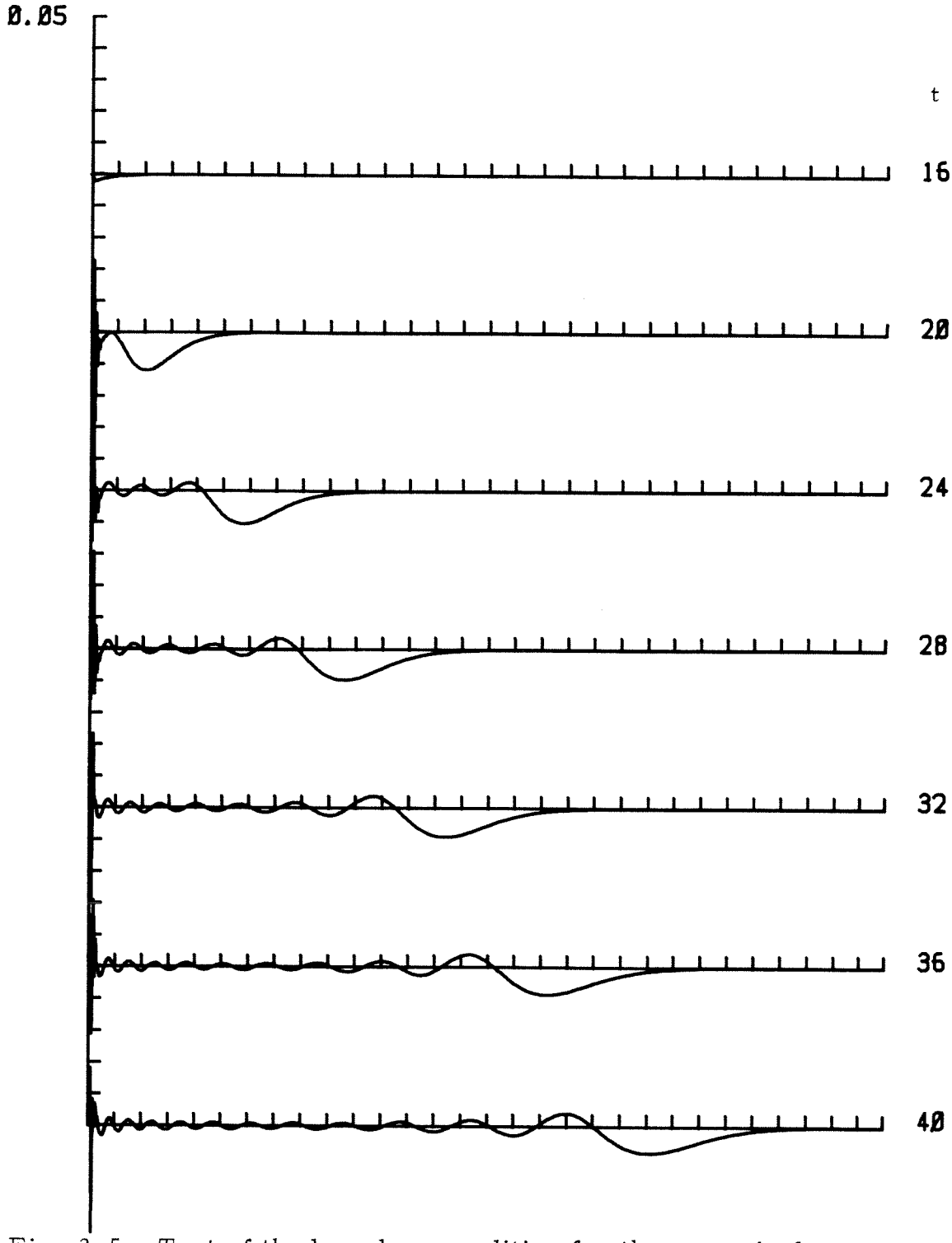

Fig. 3.5. Test of the boundary condition for the numerical Boussinesq model using the solitary wave as initial condition, $a_B = 0.3$, with two different window sizes.

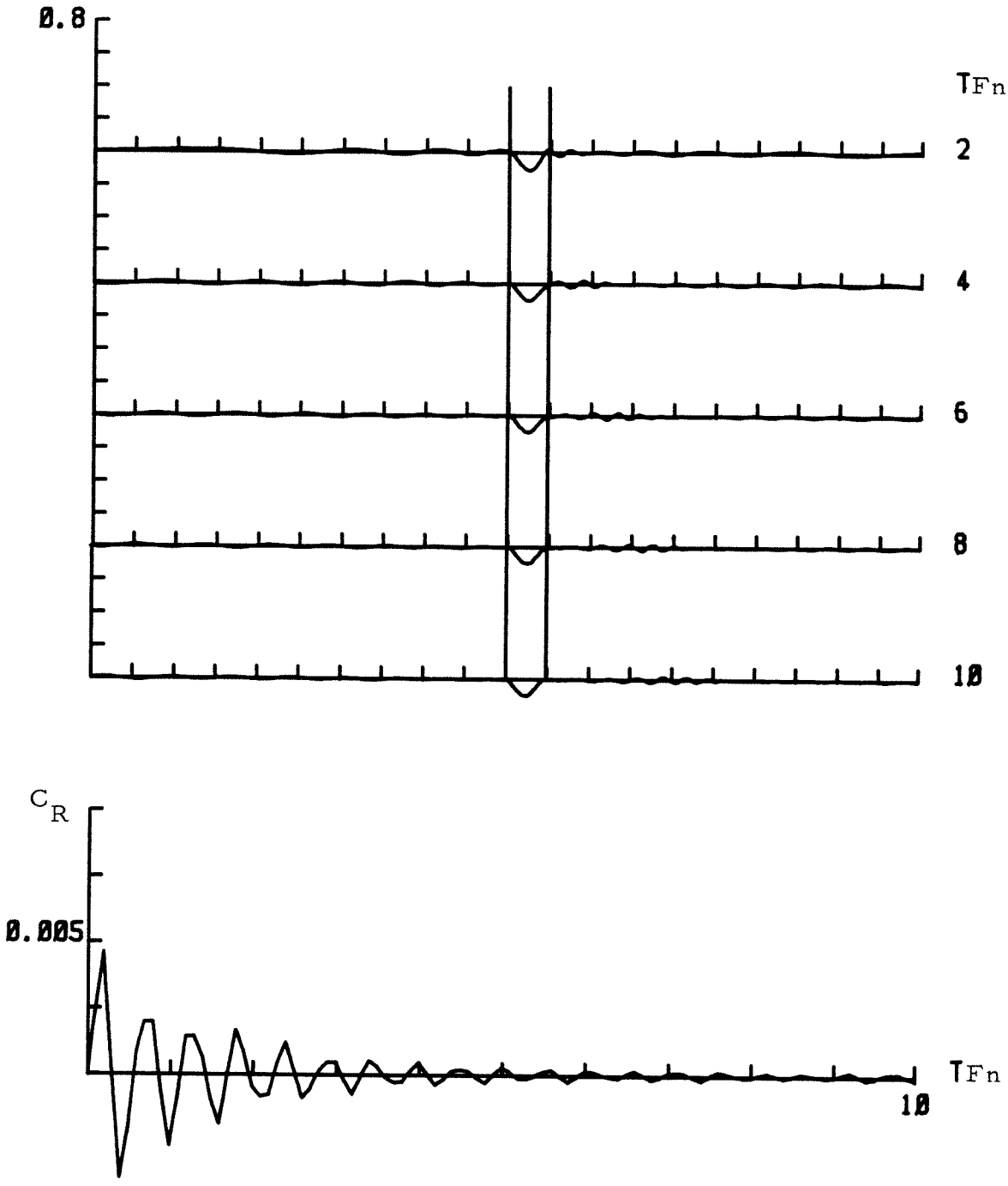

Fig. 4. 1. 1. The surface wave elevation and the wave resistance coefficient of the cosine surface pressure given by the numerical Boussinesq model for $p_m = 0.1$, $\epsilon = 0.5$ and $Fn = 0.1$.

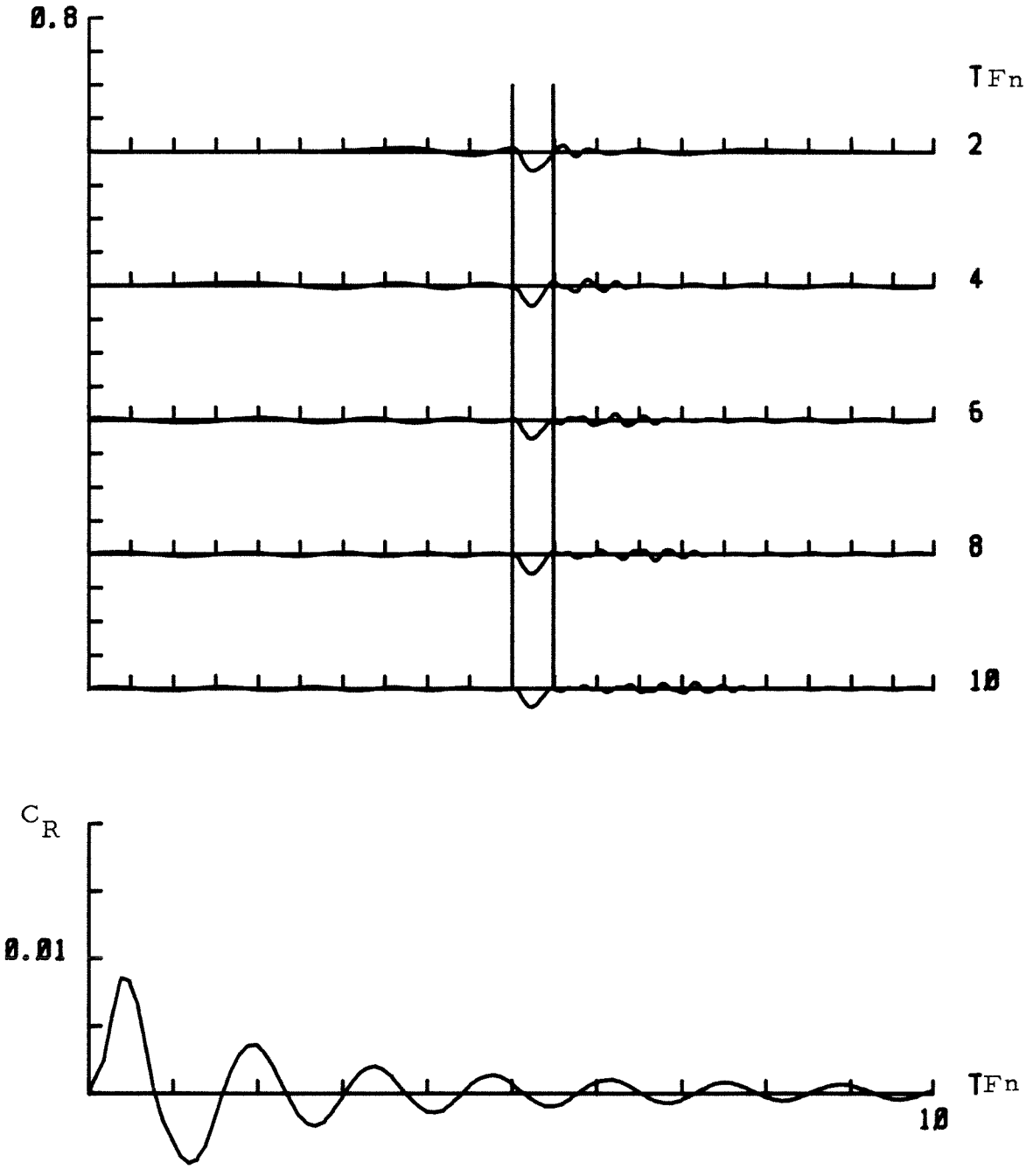

Fig. 4. 1. 2. The surface wave elevation and the wave resistance coefficient of the cosine surface pressure given by the numerical Boussinesq model for $p_m = 0.1$, $\epsilon = 0.5$ and $Fn = 0.2$.

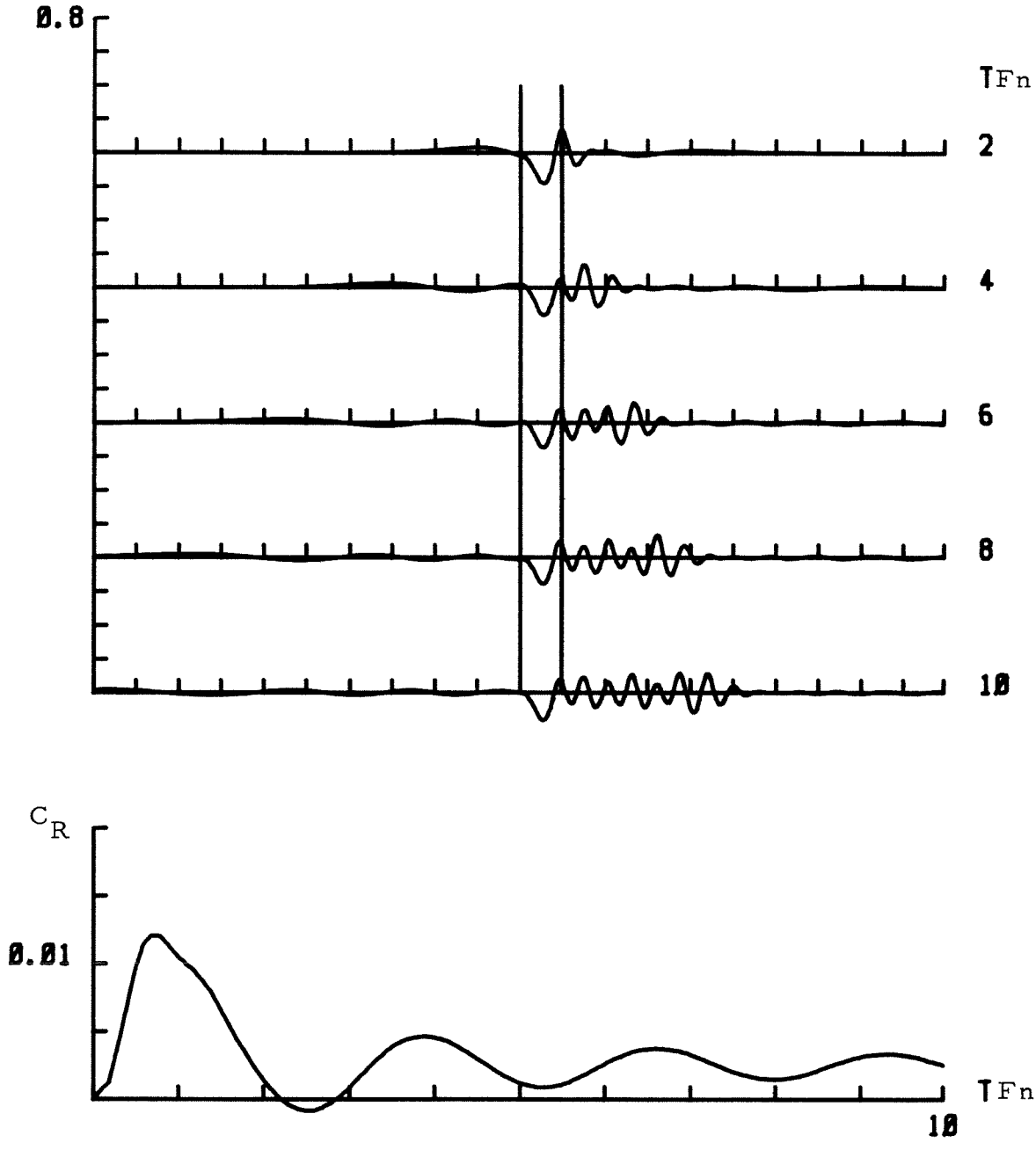

Fig. 4. 1. 3. The surface wave elevation and the wave resistance coefficient of the cosine surface pressure given by the numerical Boussinesq model for $p_m = 0.1$, $\epsilon = 0.5$ and $Fn = 0.3$.

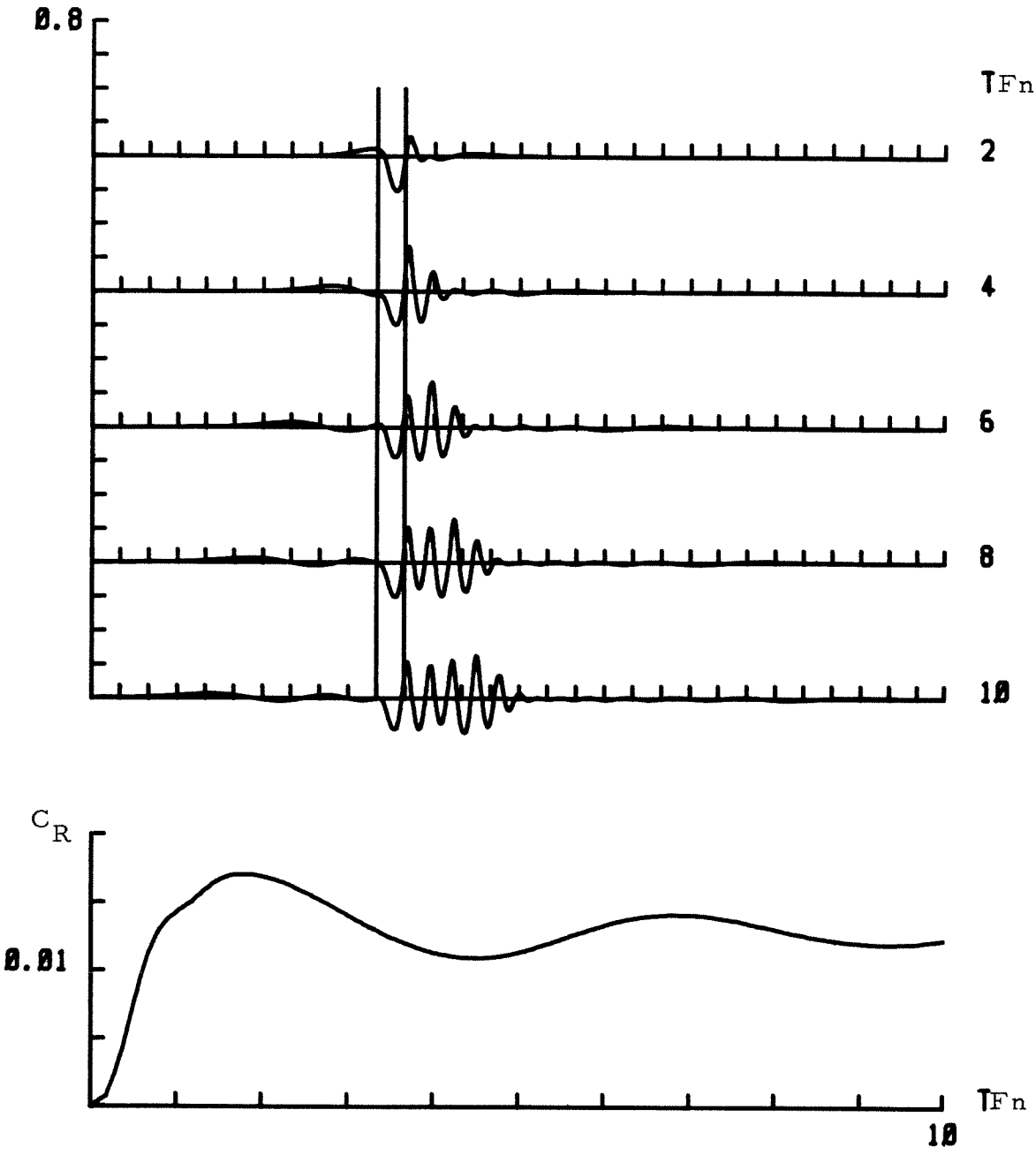

Fig. 4. 1. 4. The surface wave elevation and the wave resistance coefficient of the cosine surface pressure given by the numerical Boussinesq model for $p_m = 0.1$, $\epsilon = 0.5$ and $Fn = 0.4$.

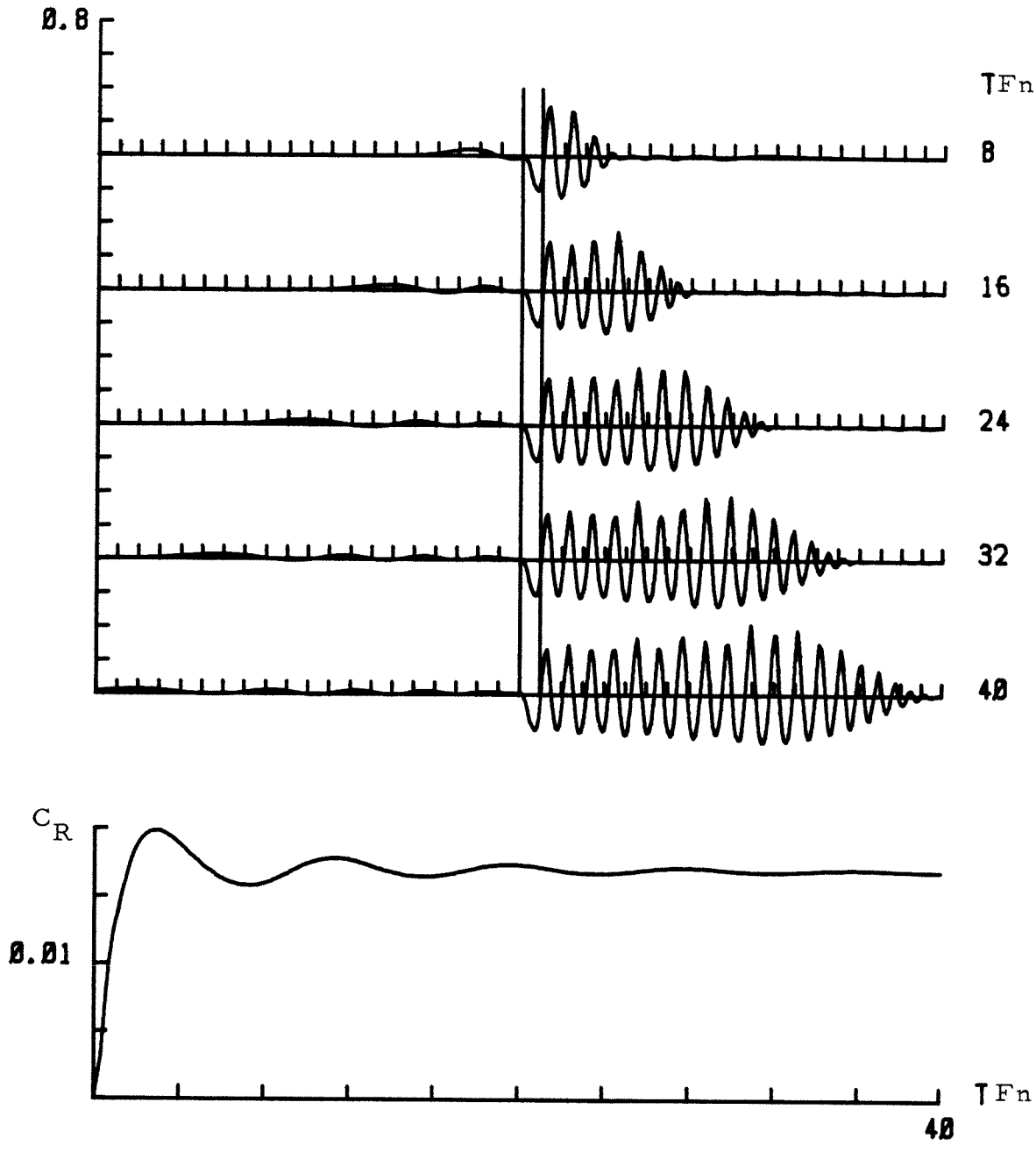

Fig. 4. 1. 5. The surface wave elevation and the wave resistance coefficient of the cosine surface pressure given by the numerical Boussinesq model for $p_m = 0.1$, $\epsilon = 0.5$ and $Fn = 0.5$.

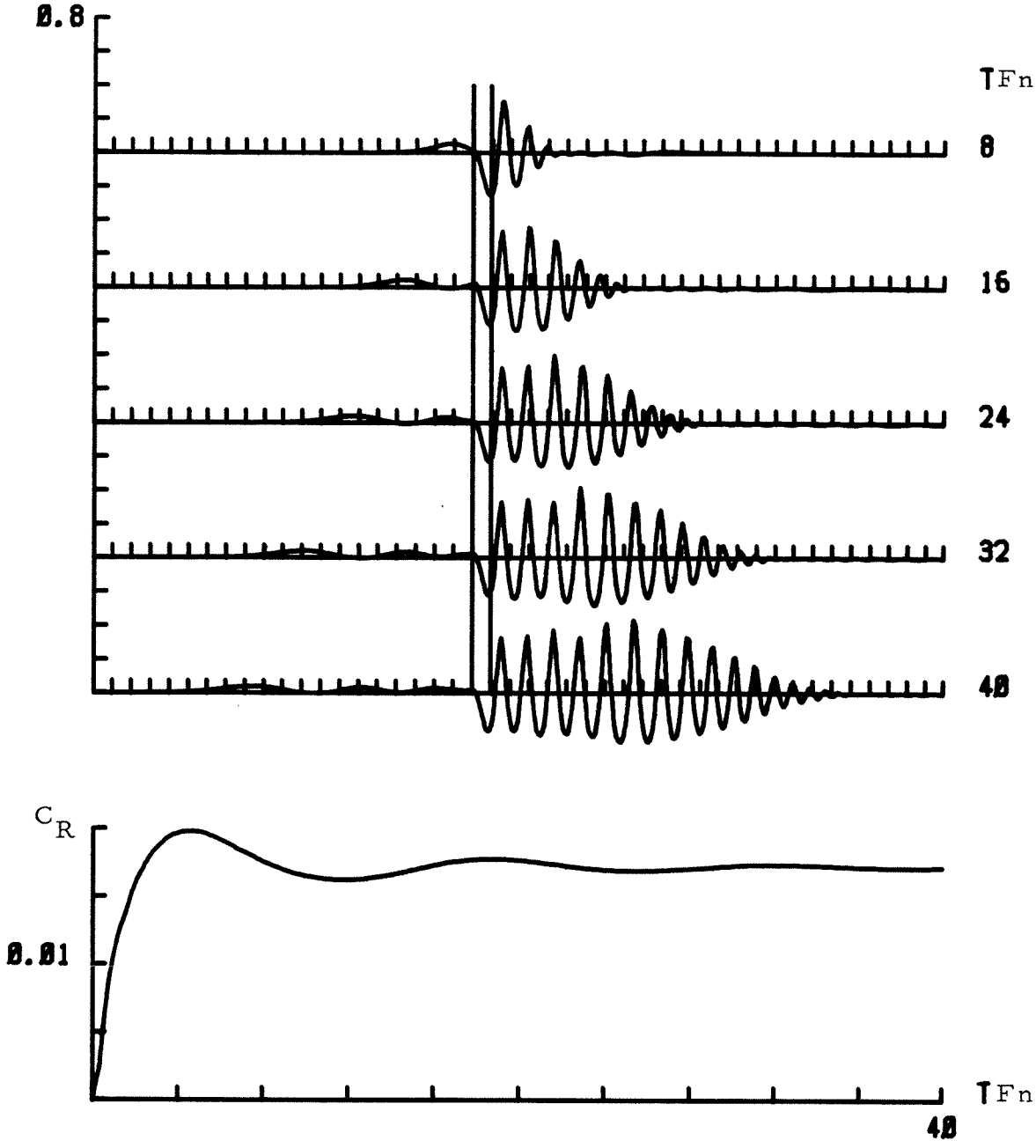

Fig. 4. 1. 6. The surface wave elevation and the wave resistance coefficient of the cosine surface pressure given by the numerical Boussinesq model for $p_m = 0.1$, $\epsilon = 0.5$ and $Fn = 0.6$.

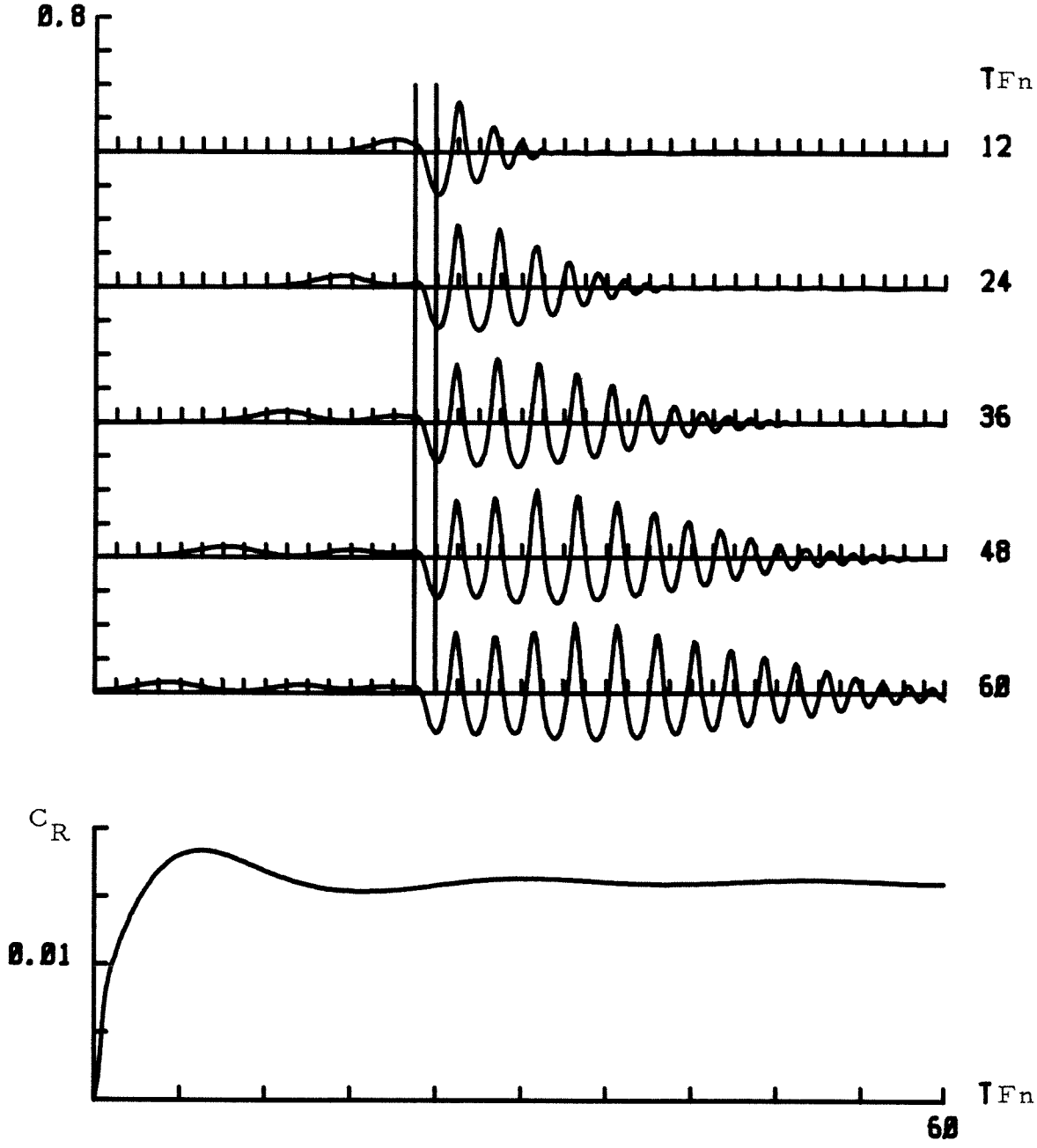

Fig. 4. 1. 7. The surface wave elevation and the wave resistance coefficient of the cosine surface pressure given by the numerical Boussinesq model for $p_m = 0.1$, $\epsilon = 0.5$ and $Fn = 0.7$.

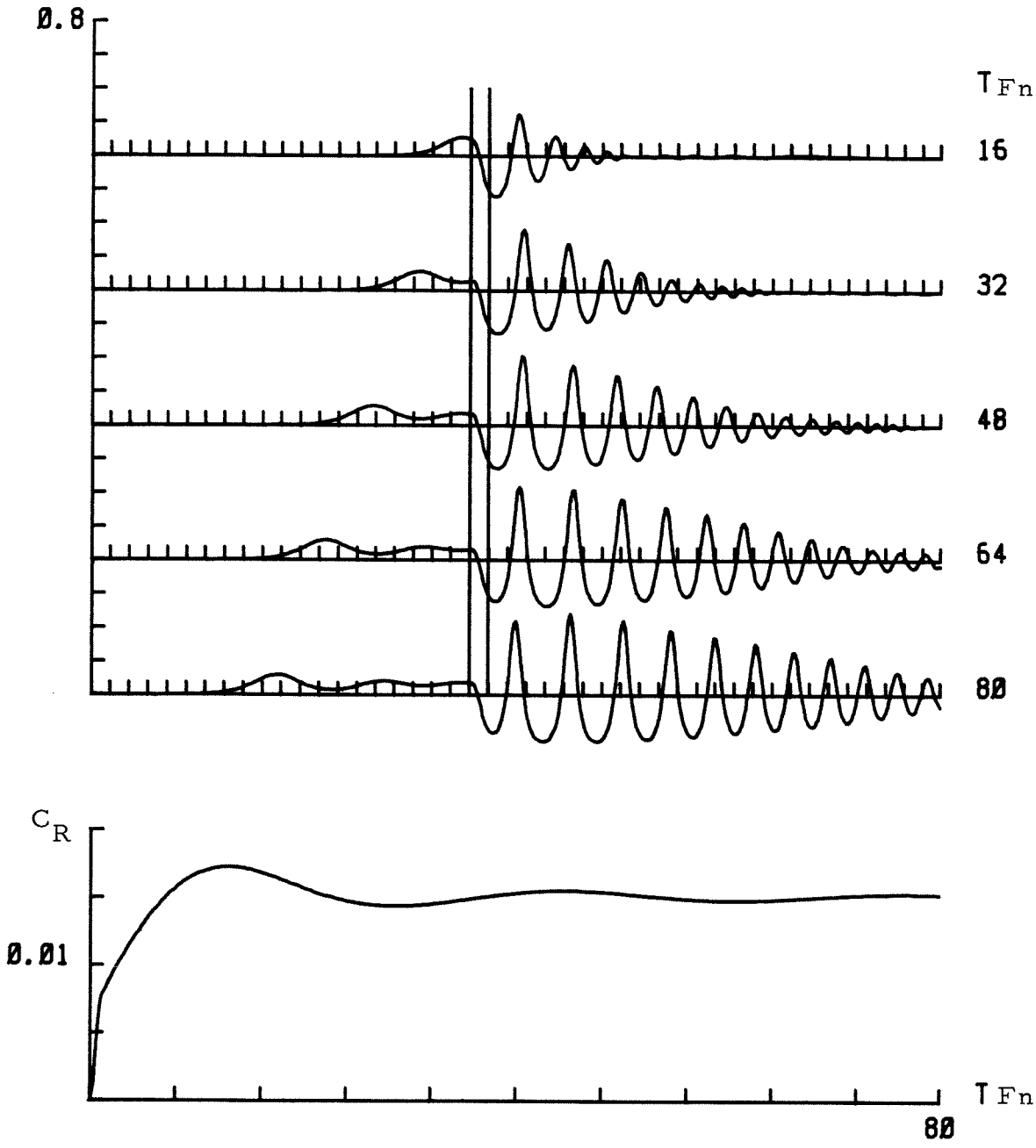

Fig. 4. 1. 8. The surface wave elevation and the wave resistance coefficient of the cosine surface pressure given by the numerical Boussinesq model for $p_m = 0.1$, $\epsilon = 0.5$ and $Fn = 0.8$.

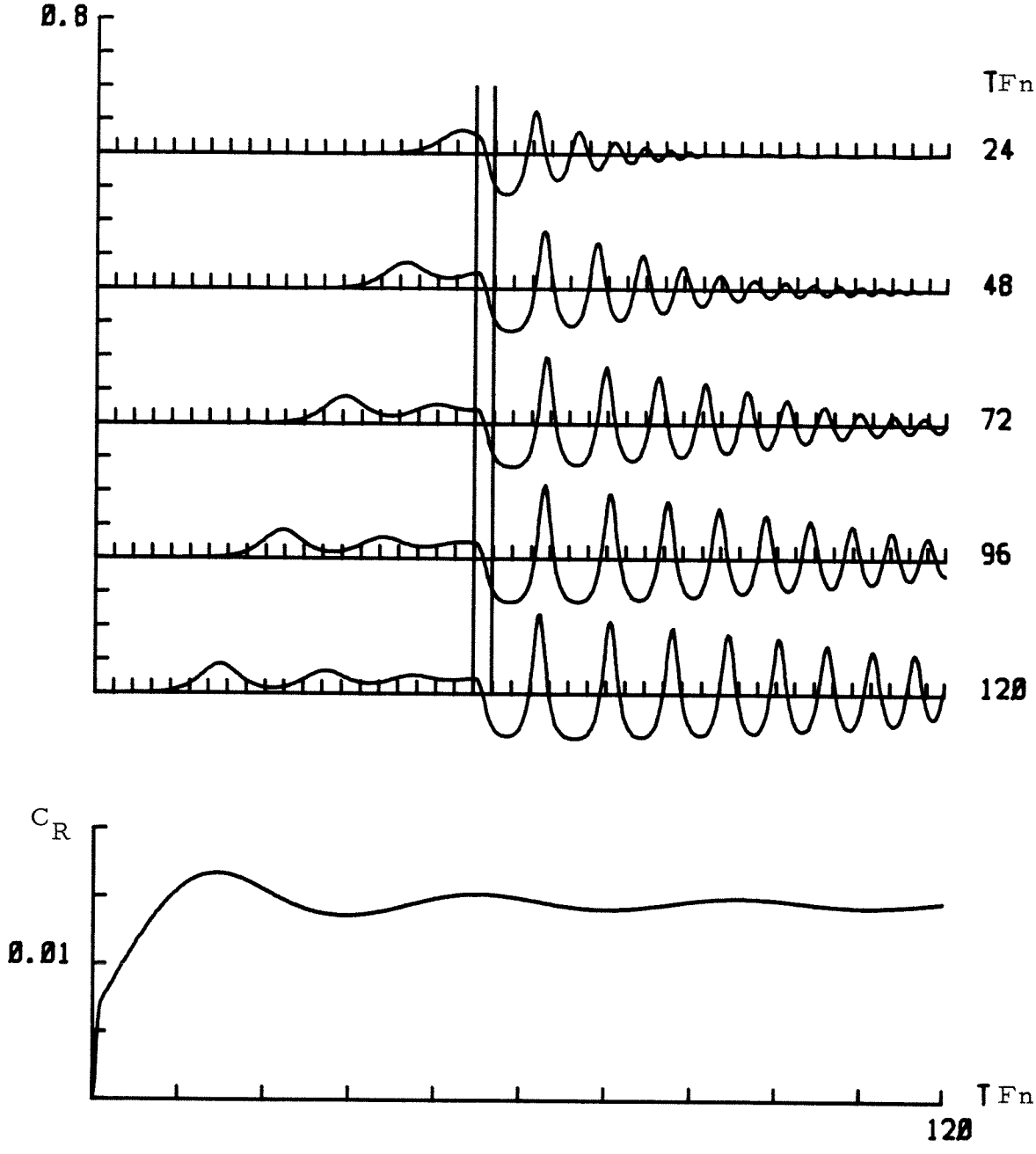

Fig. 4. 1. 9. The surface wave elevation and the wave resistance coefficient of the cosine surface pressure given by the numerical Boussinesq model for $p_m = 0.1$, $\epsilon = 0.5$ and $Fn = 0.85$.

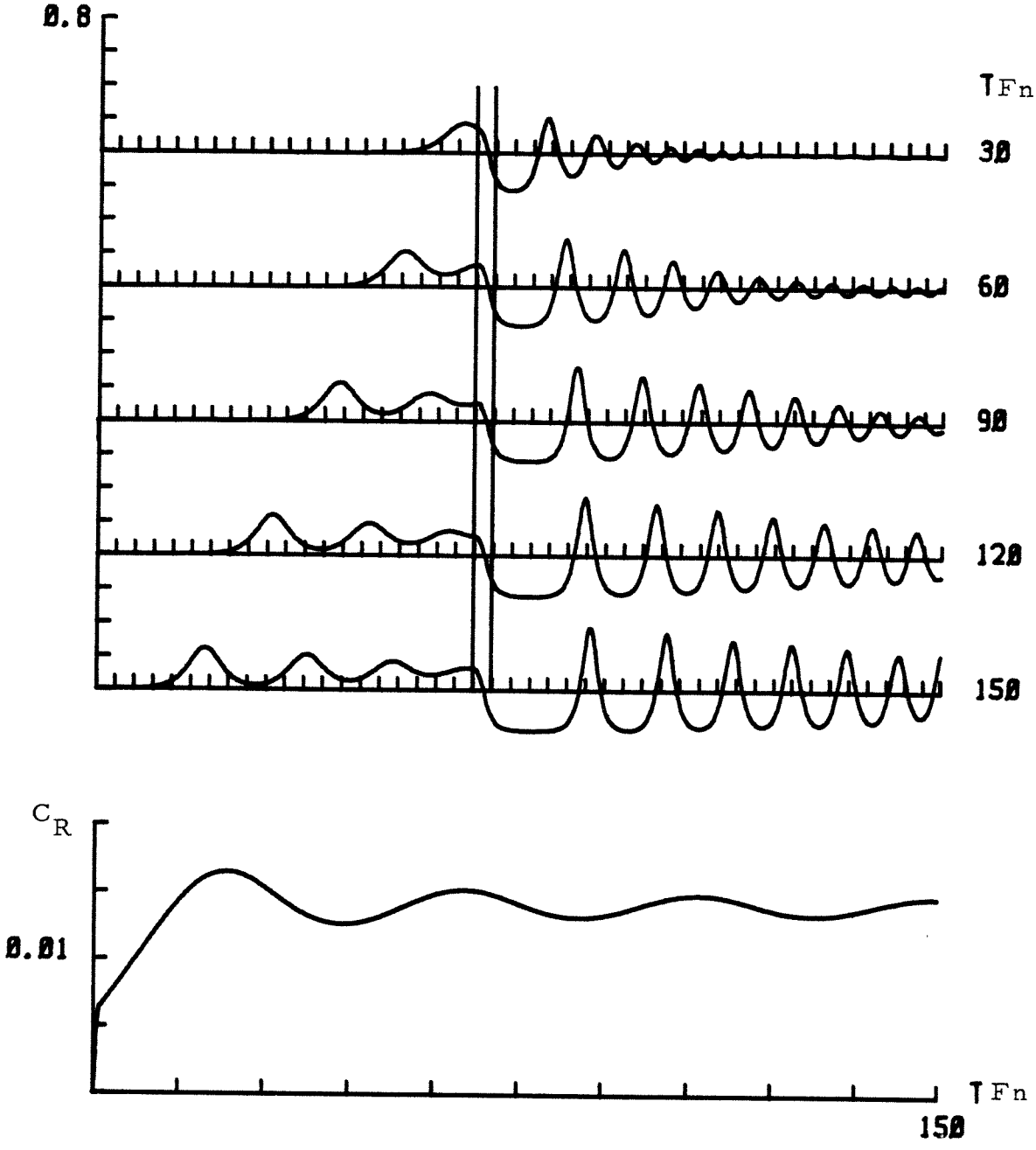

Fig. 4. 1. 10. The surface wave elevation and the wave resistance coefficient of the cosine surface pressure given by the numerical Boussinesq model for $p_m = 0.1$, $\epsilon = 0.5$ and $Fn = 0.9$.

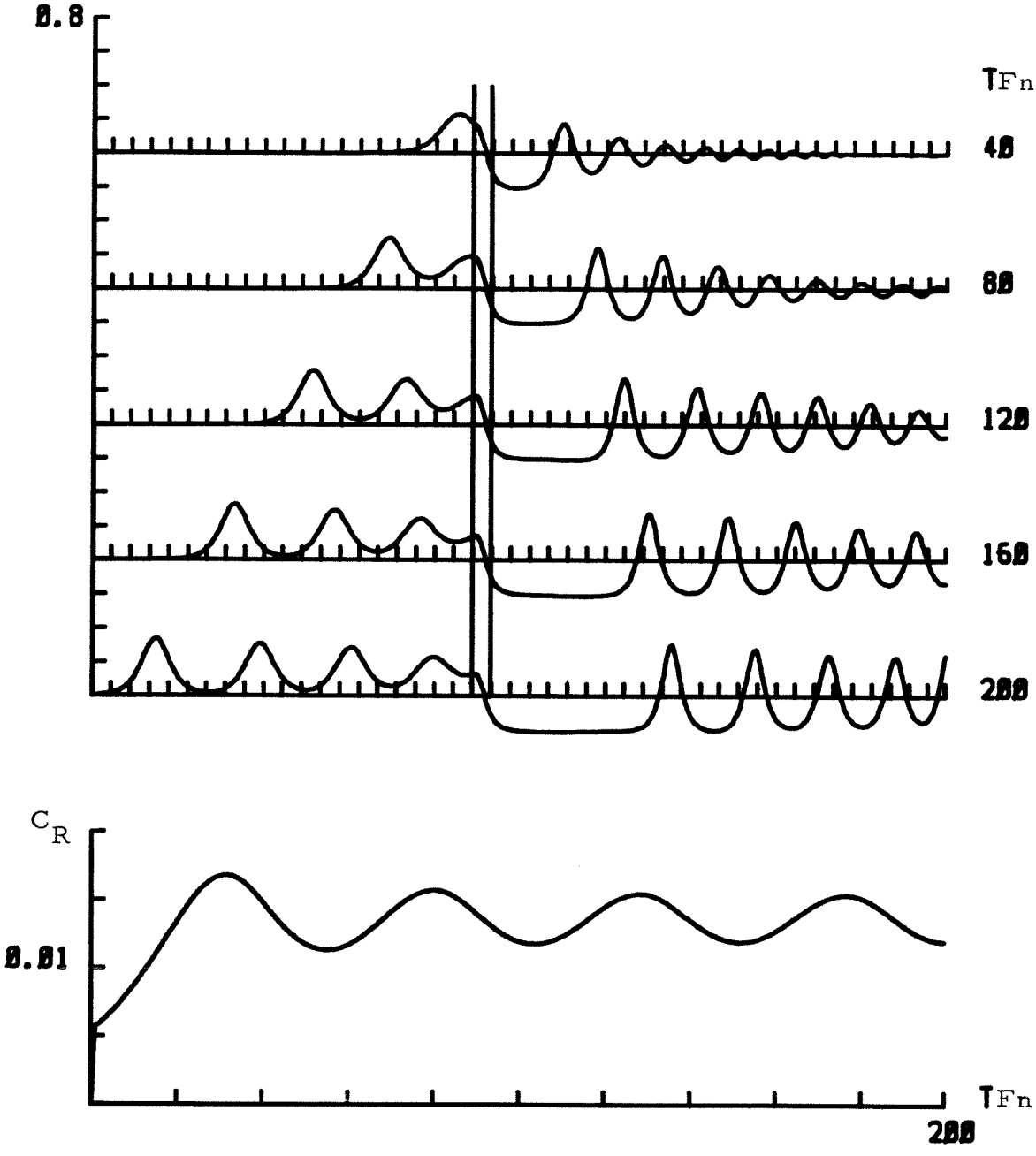

Fig. 4. 1. 11. The surface wave elevation and the wave resistance coefficient of the cosine surface pressure given by the numerical Boussinesq model for $p_m = 0.1$, $\epsilon = 0.5$ and $Fn = 0.95$.

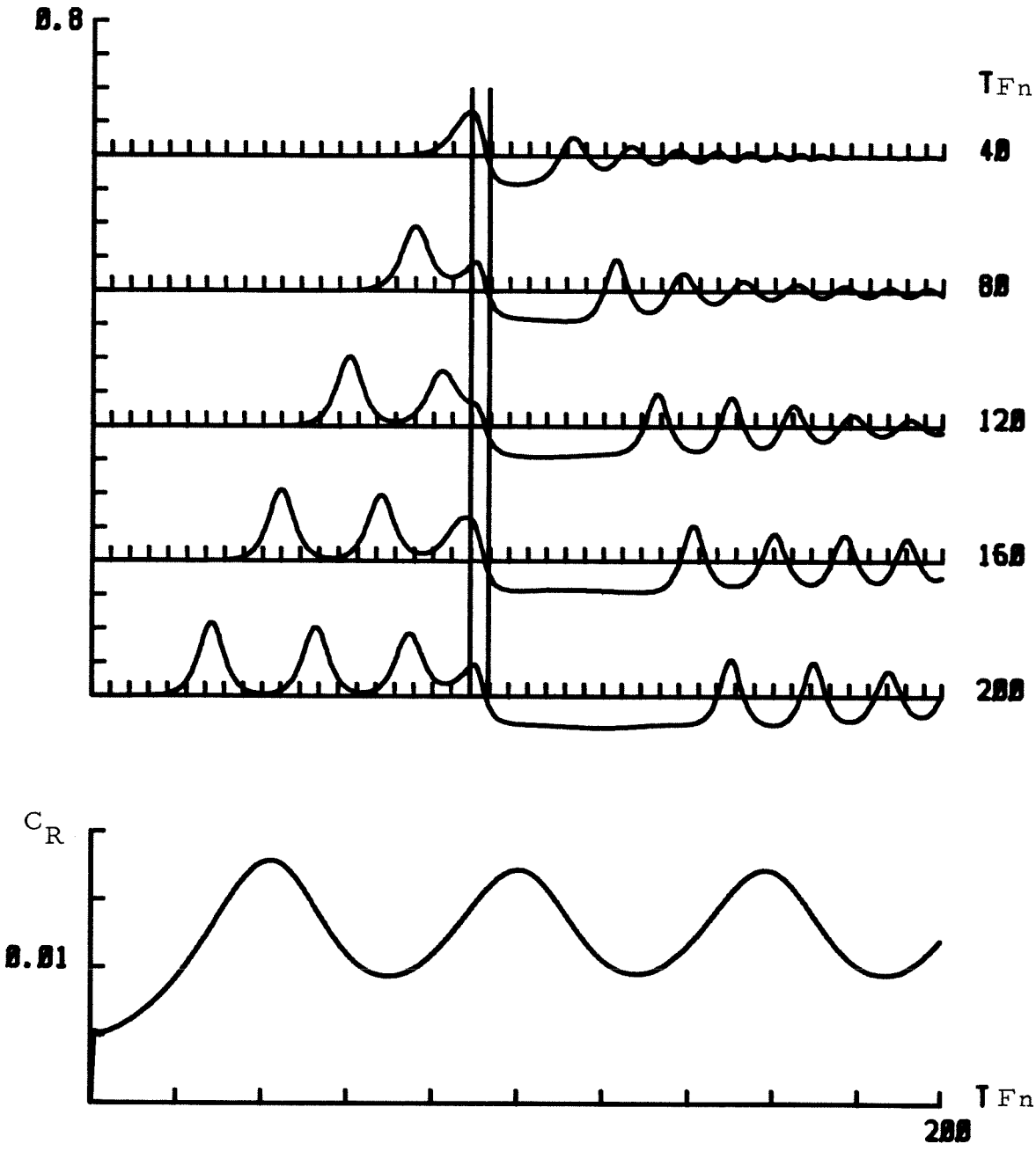

Fig. 4.1.12. The surface wave elevation and the wave resistance coefficient of the cosine surface pressure given by the numerical Boussinesq model for $p_m = 0.1$, $\epsilon = 0.5$ and $Fn = 1.0$.

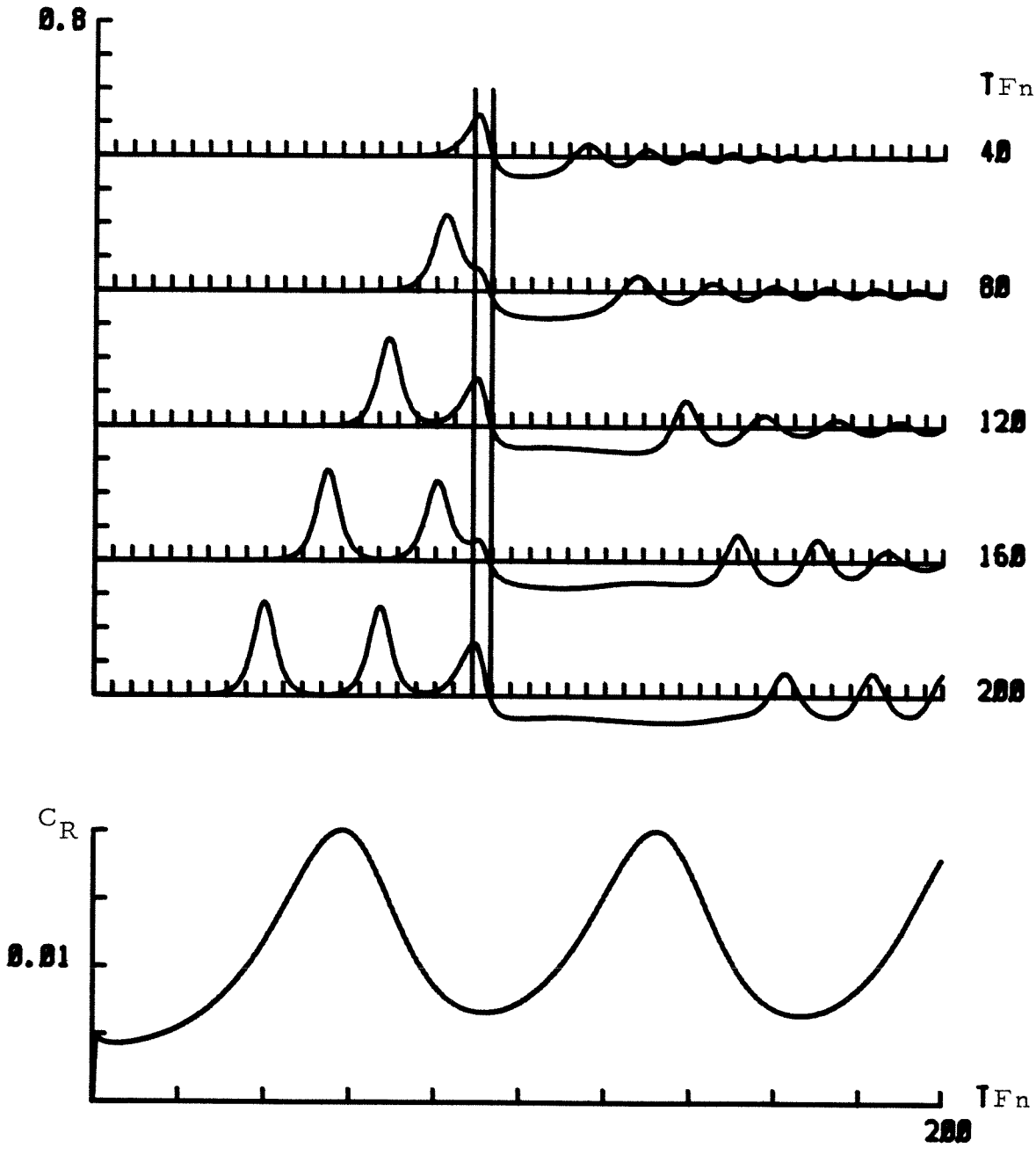

Fig. 4.1.13. The surface wave elevation and the wave resistance coefficient of the cosine surface pressure given by the numerical Boussinesq model for $p_m = 0.1$, $\epsilon = 0.5$ and $Fn = 1.05$.

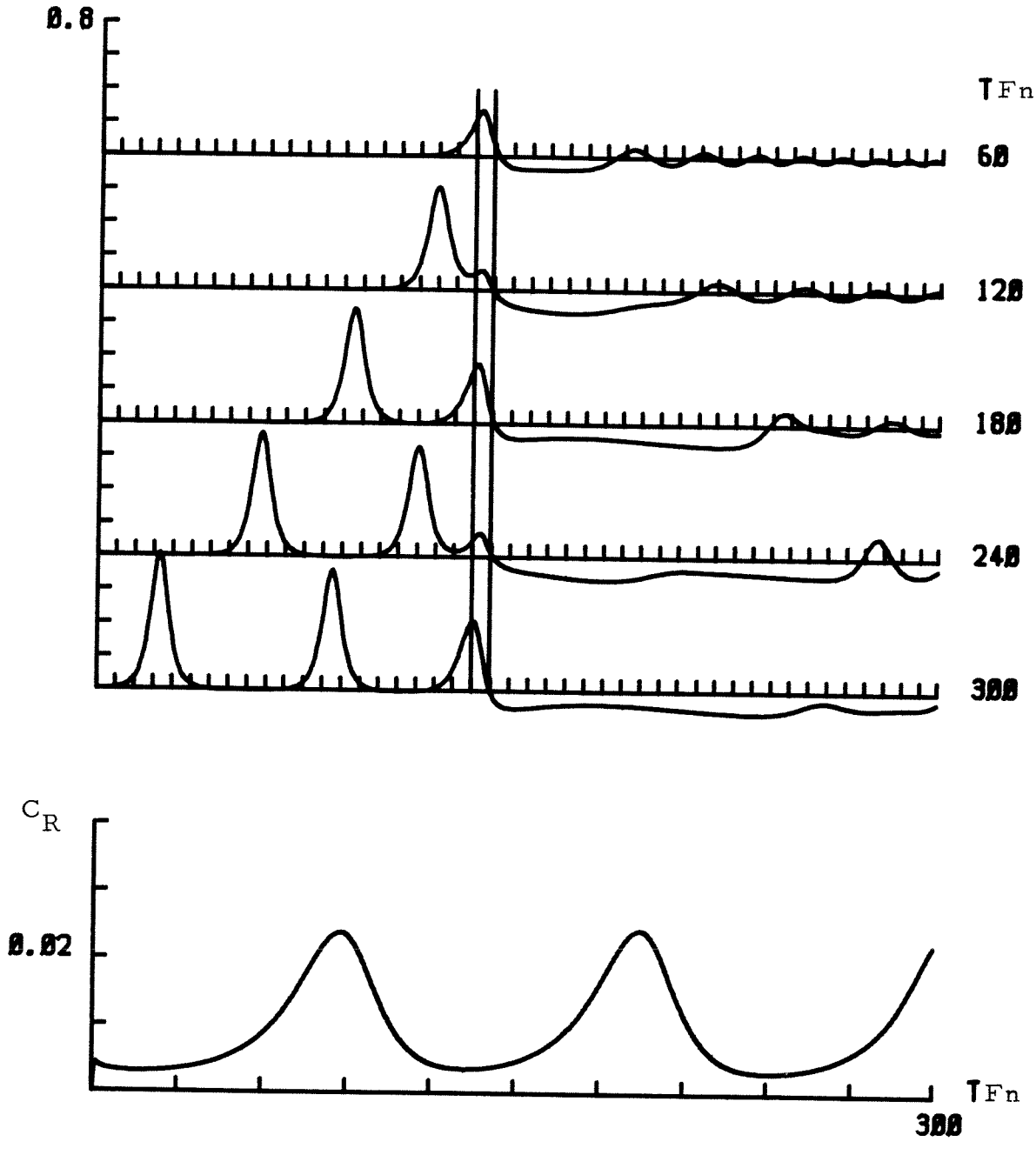

Fig. 4. 1. 14. The surface wave elevation and the wave resistance coefficient of the cosine surface pressure given by the numerical Boussinesq model for $p_m = 0.1$, $\epsilon = 0.5$ and $Fn = 1.1$.

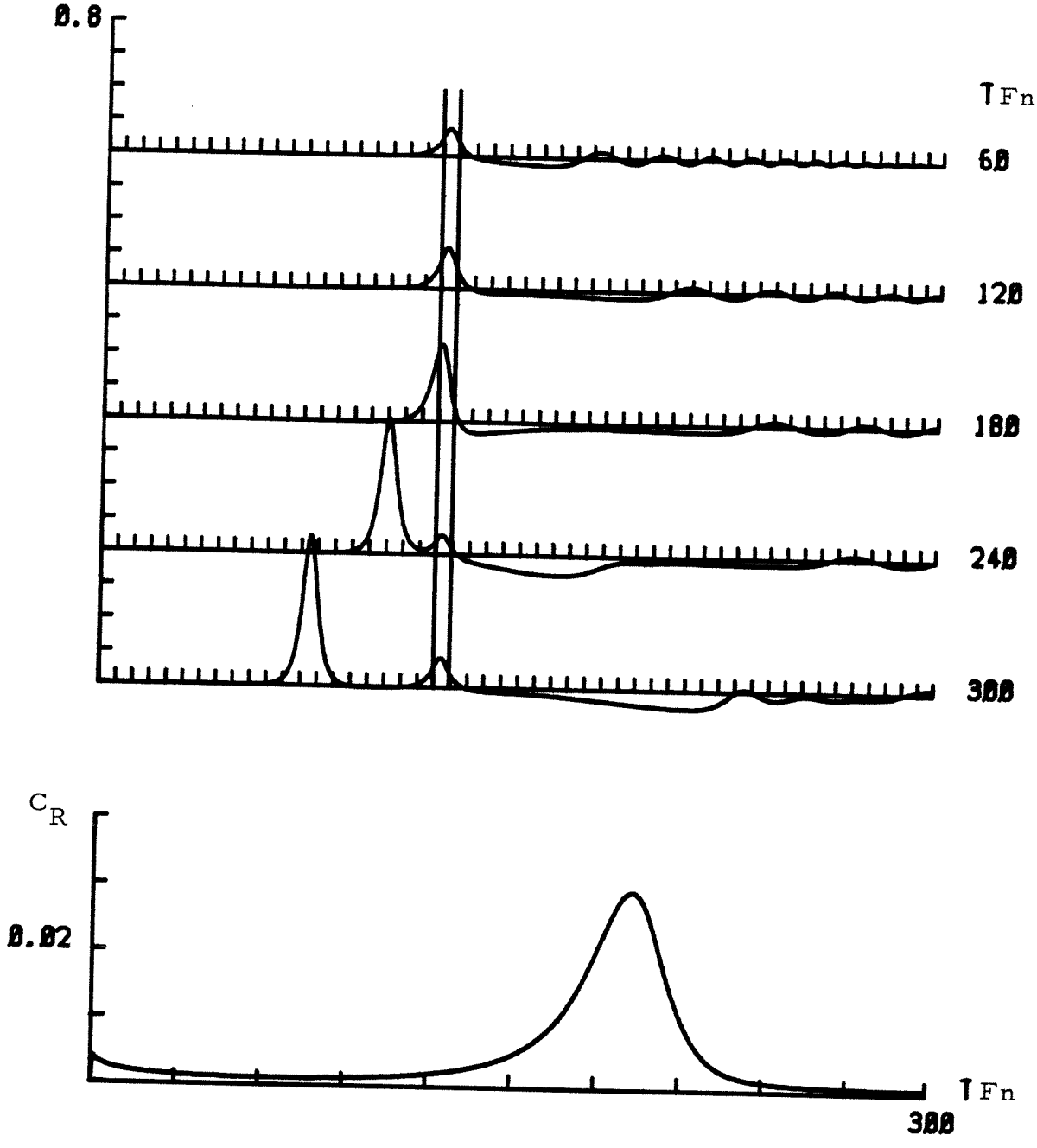

Fig. 4. 1. 15. The surface wave elevation and the wave resistance coefficient of the cosine surface pressure given by the numerical Boussinesq model for $p_m = 0.1$, $\epsilon = 0.5$ and Fn = 1. 15.

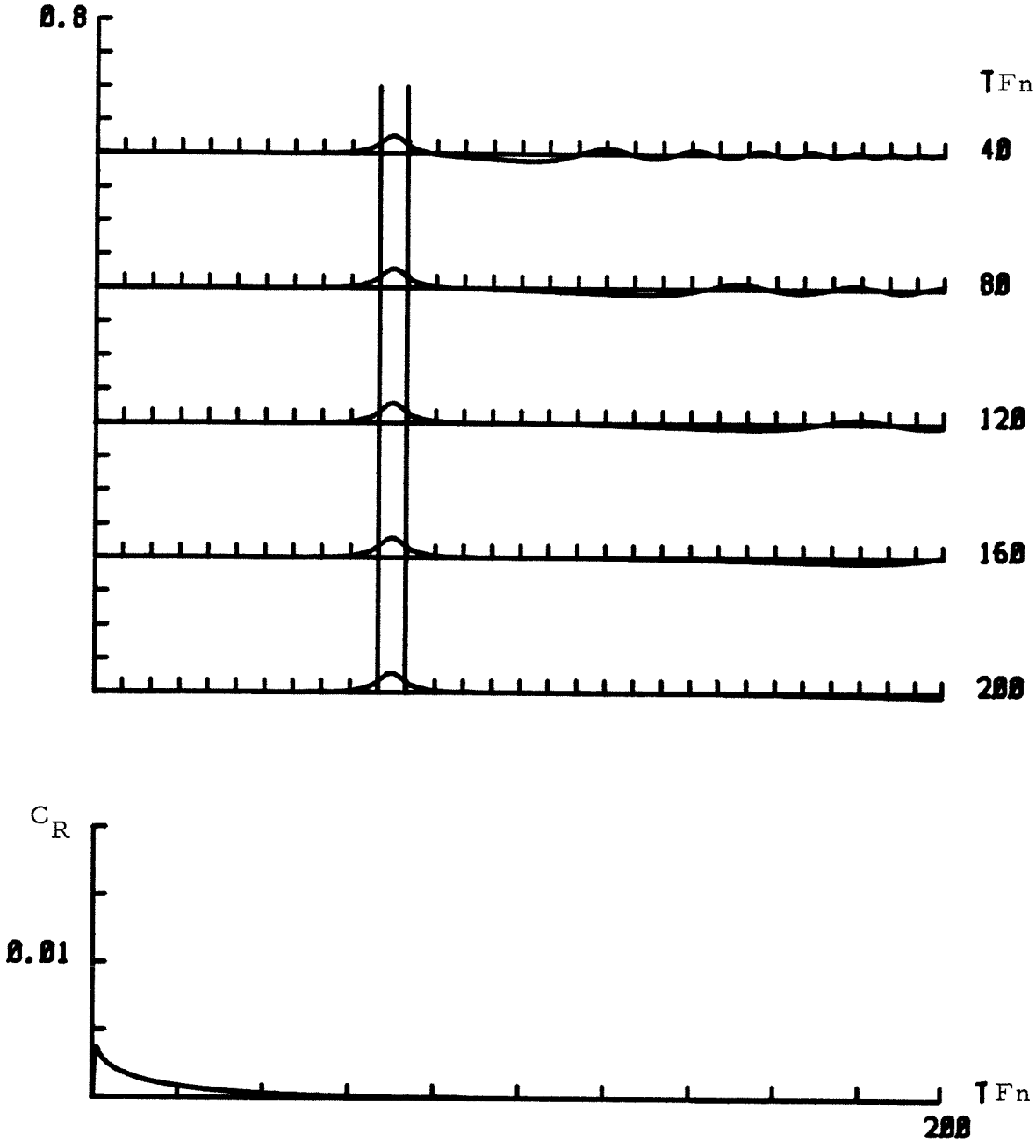

Fig. 4.1.16. The surface wave elevation and the wave resistance coefficient of the cosine surface pressure given by the numerical Boussinesq model for $p_m = 0.1$, $\epsilon = 0.5$ and $Fn = 1.2$.

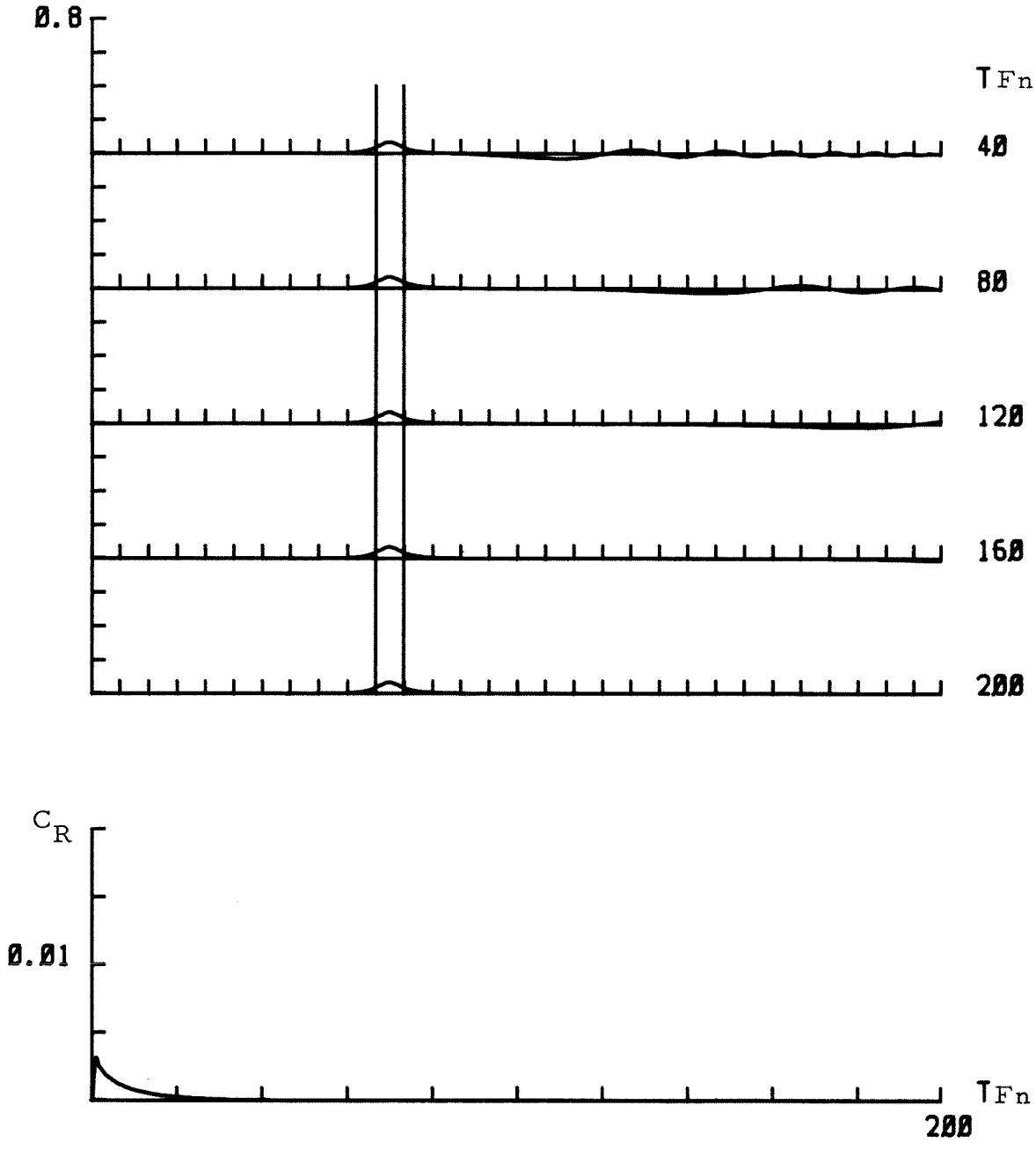

Fig. 4. 1. 17. The surface wave elevation and the wave resistance coefficient of the cosine surface pressure given by the numerical Boussinesq model for $p_m = 0.1$, $\epsilon = 0.5$ and $Fn = 1.3$.

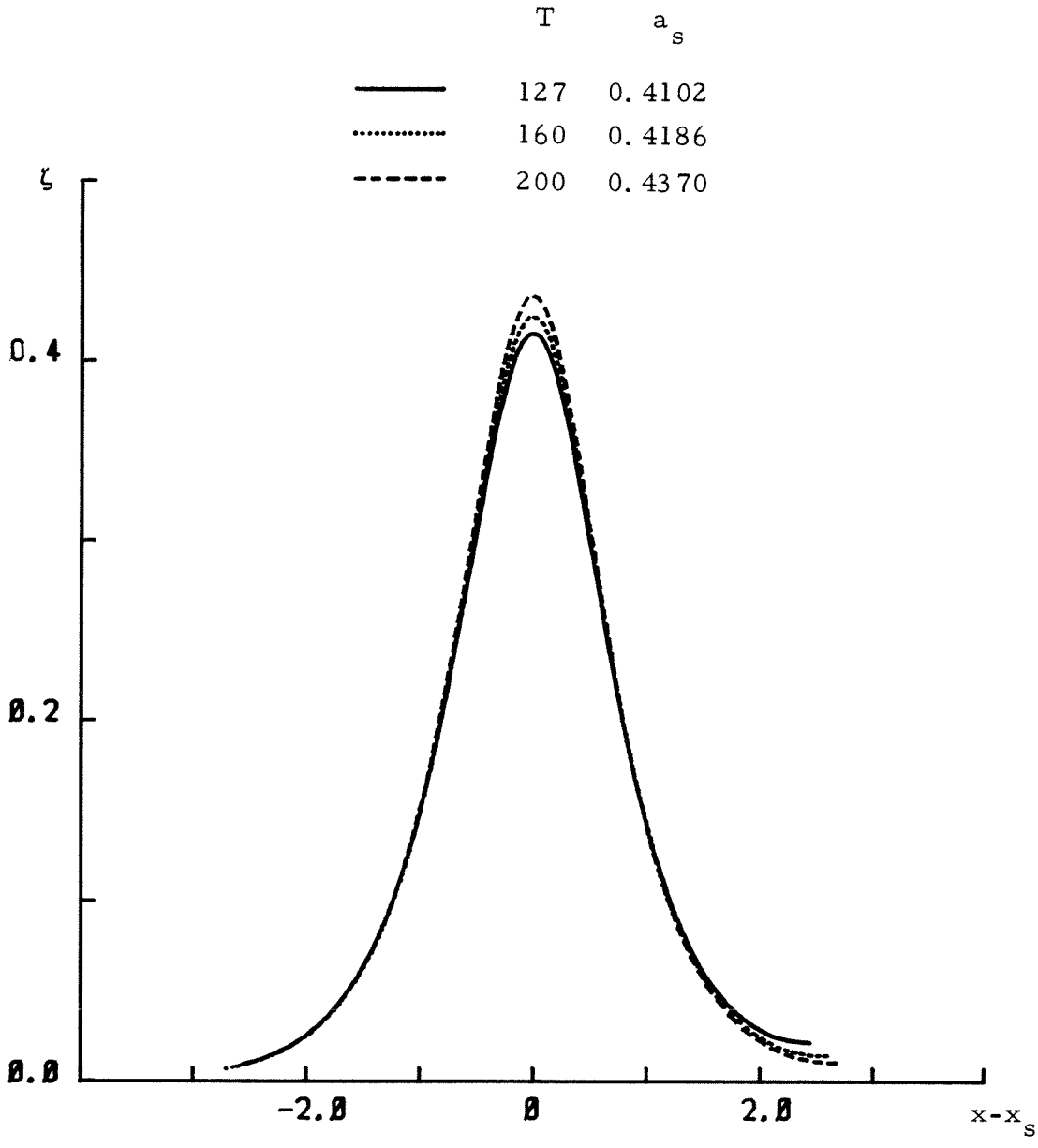

x_s = location of the peak.

Fig. 4.2.1. Evolving shape of the first runaway soliton at various times for Fn = 1.

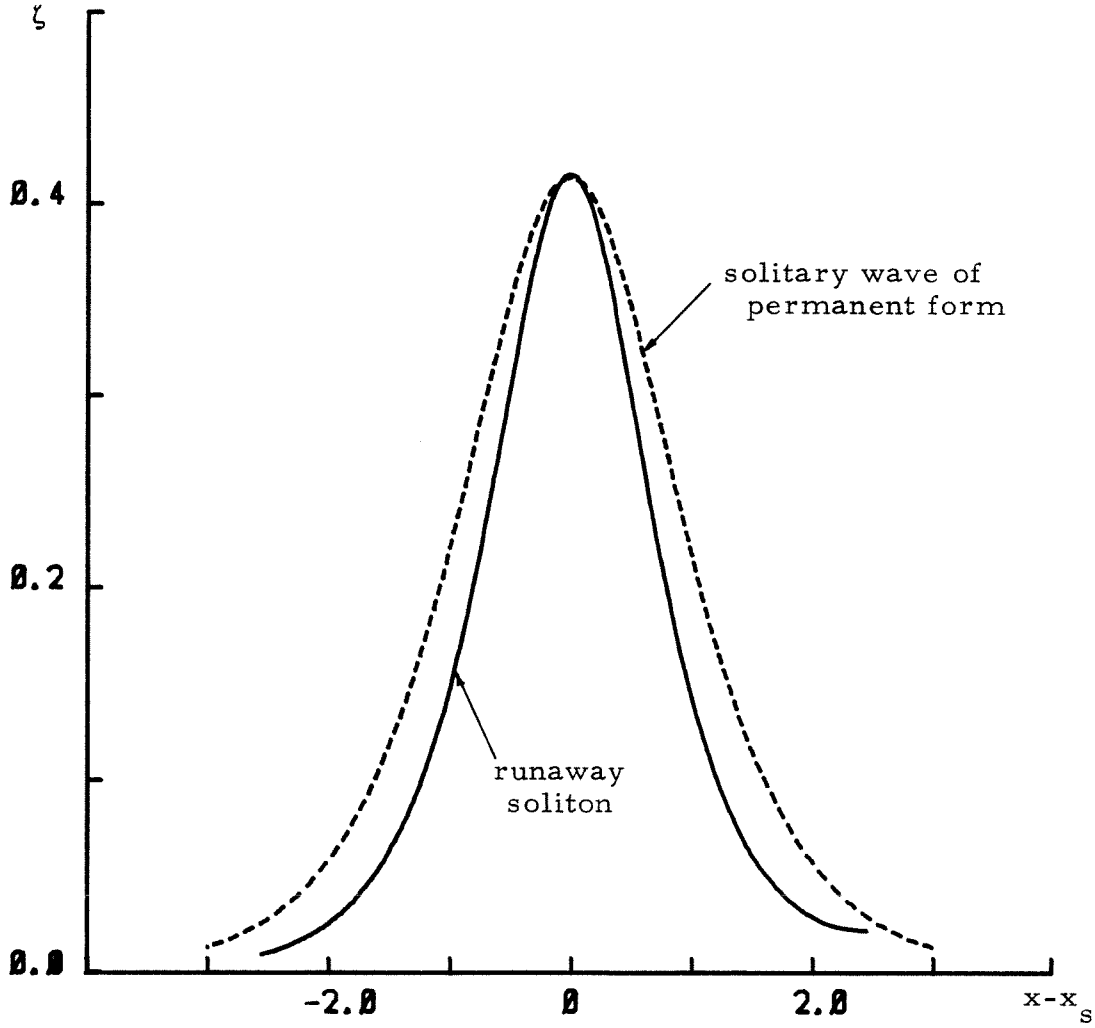

x_s = location of the peak.

Fig. 4.2.2. Comparison of wave shape between the first runaway soliton and the solitary wave of permanent form for Fn = 1.

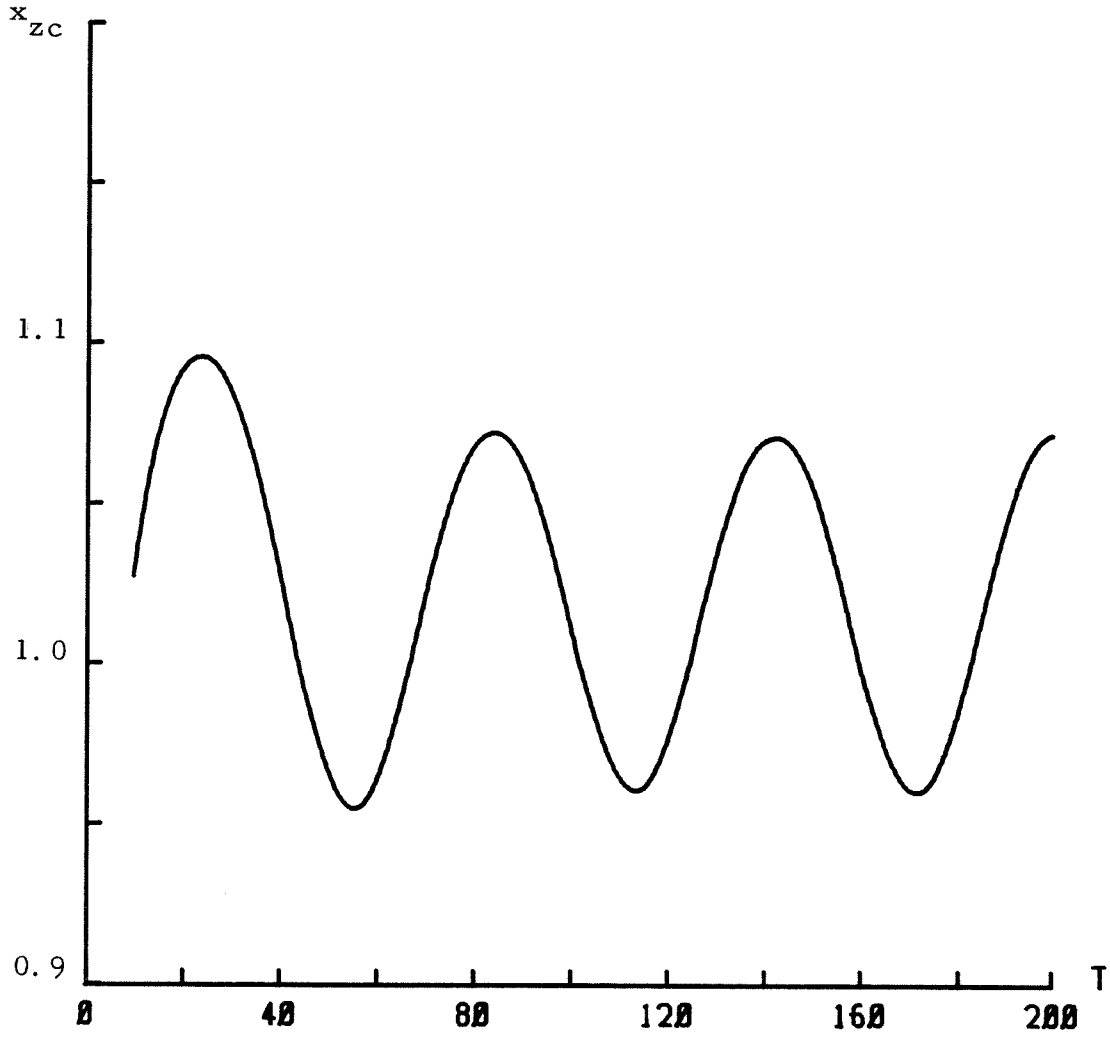

Fig. 4.2.3. Time history of the location of the first zero-crossing point of the surface elevation for Fn = 1.

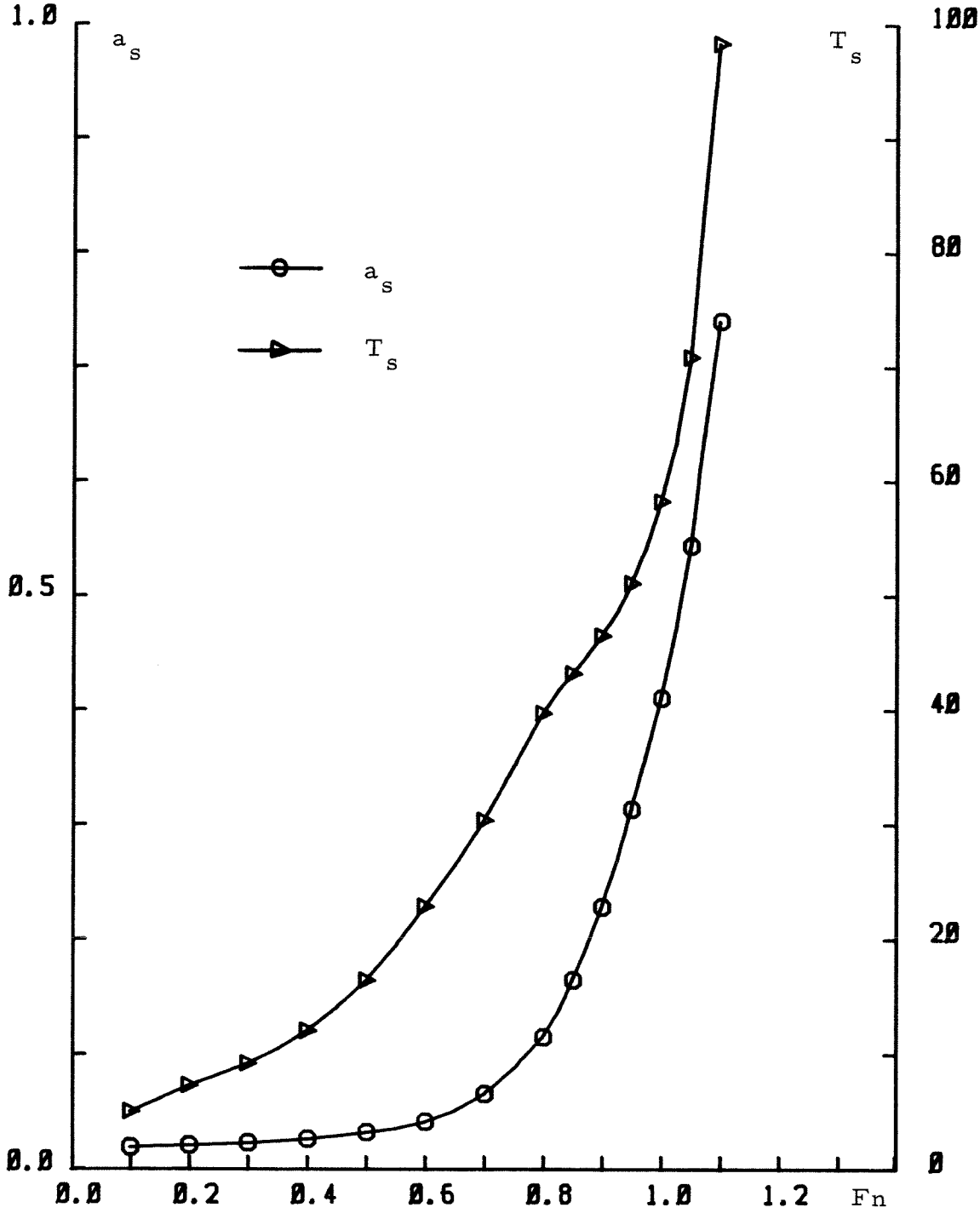

Fig. 4.3.1. Amplitude and the generation period of the first runaway soliton as functions of Fn, for $p_m = 0.1$.

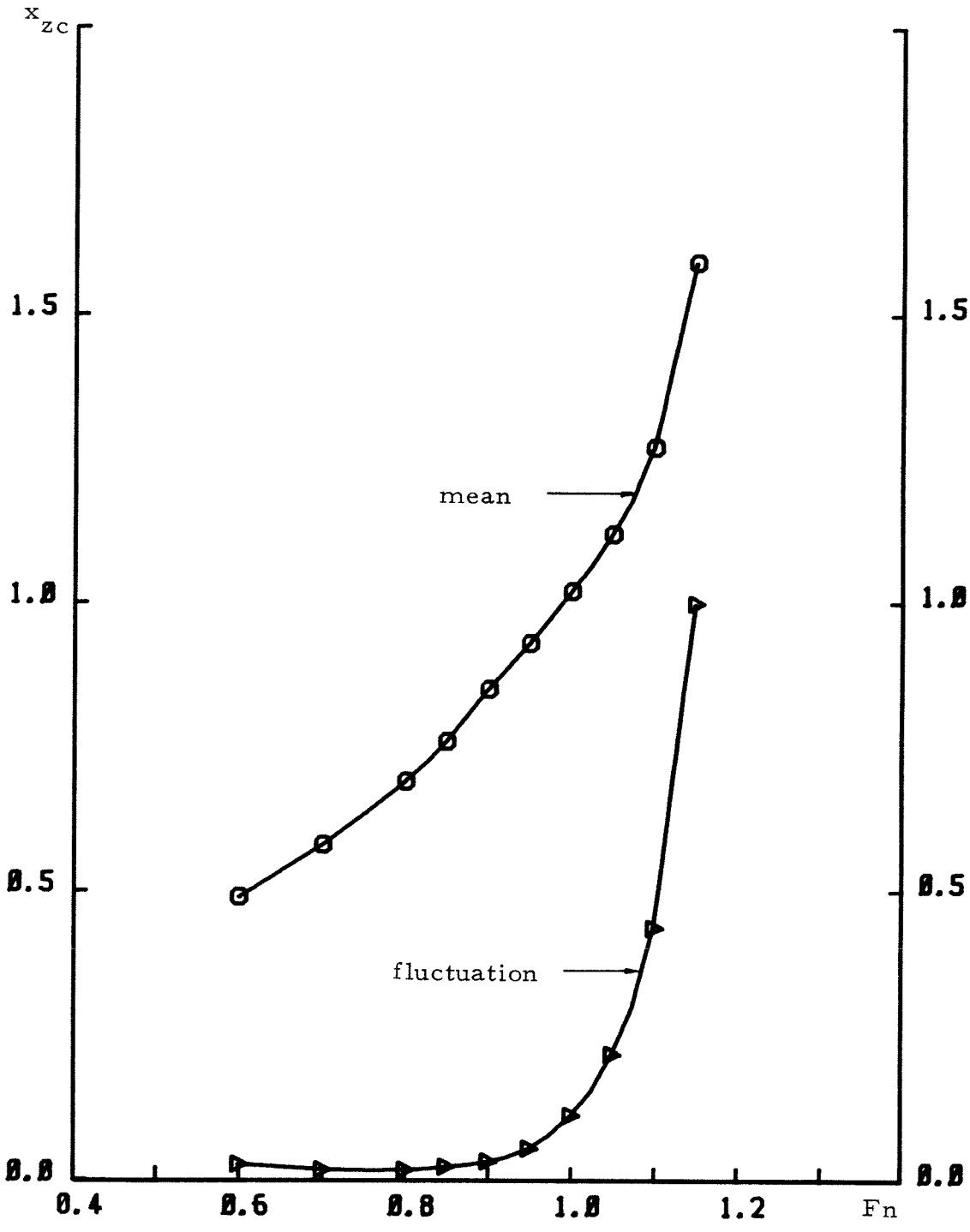

Fig. 4.3.2. Mean and fluctuation of the location of the first zero-crossing point of the surface elevation as functions of Fn.

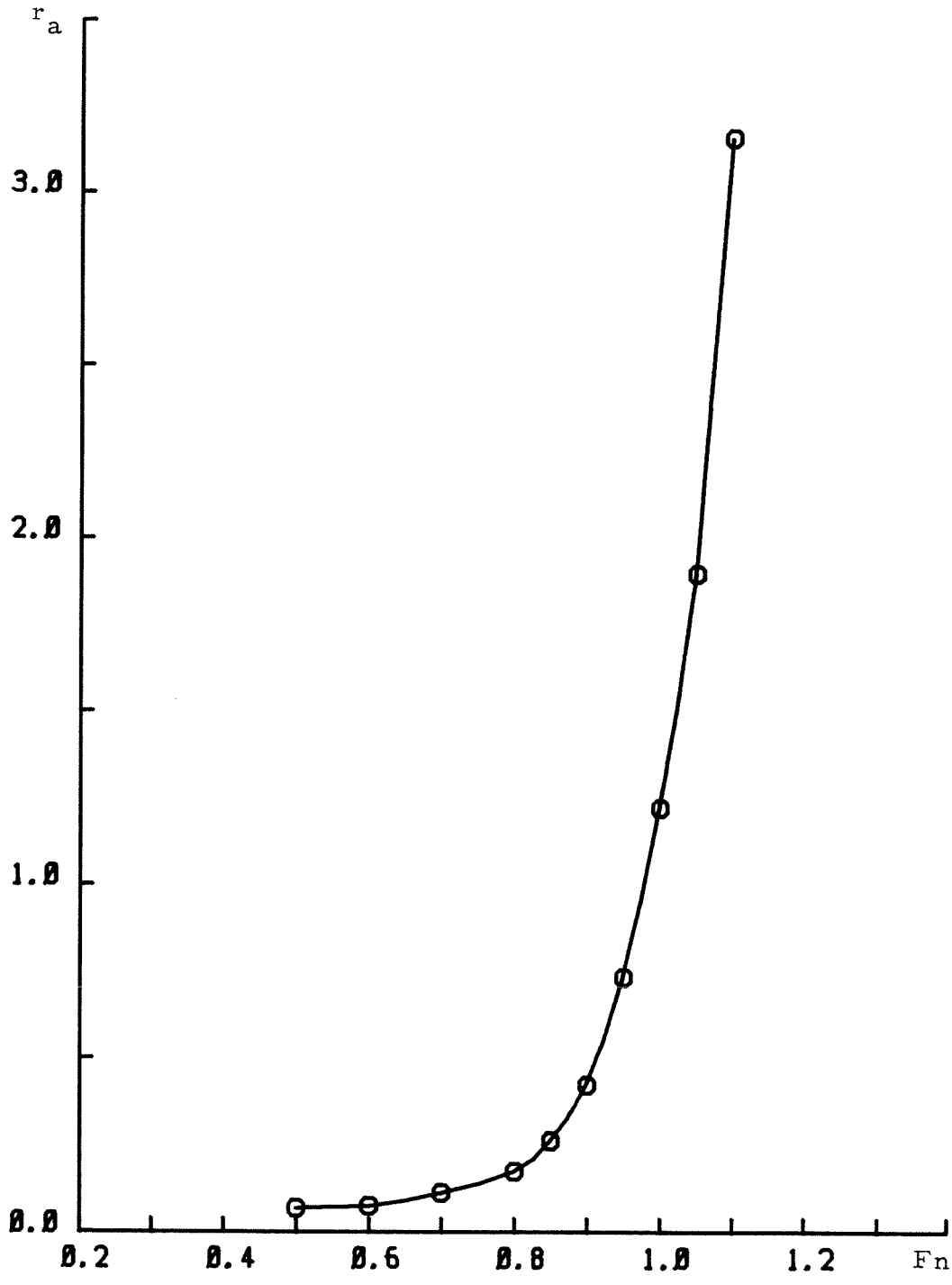

Fig. 4. 3. 3. The ratio between the amplitude of the first runaway soliton and the waveheight of the trailing wave closest to the disturbance as function of Fn.

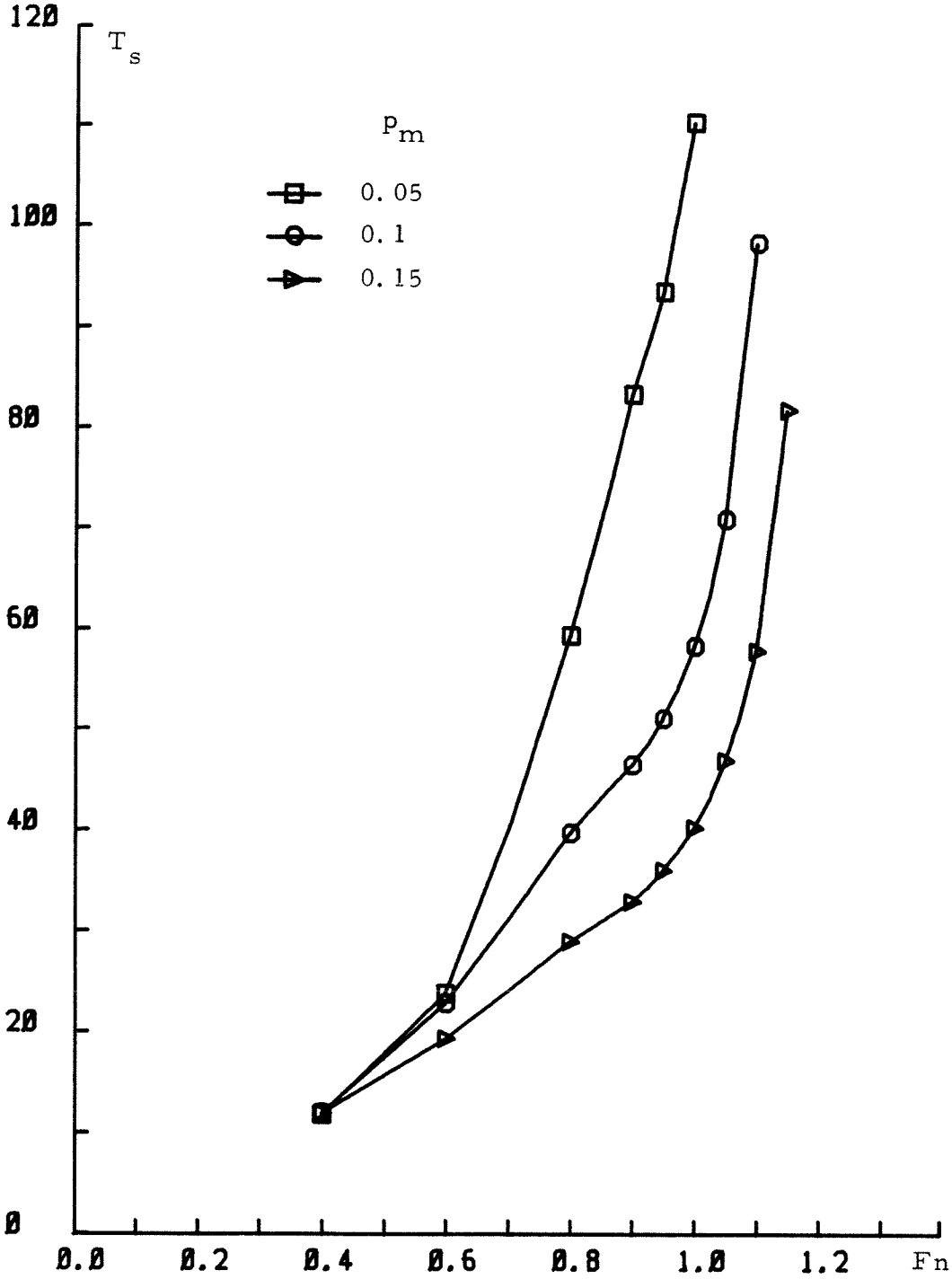

Fig. 4.3.4. Generation period of the first runaway soliton as a function of Fn for p_m = 0.05, 0.1 and 0.15.

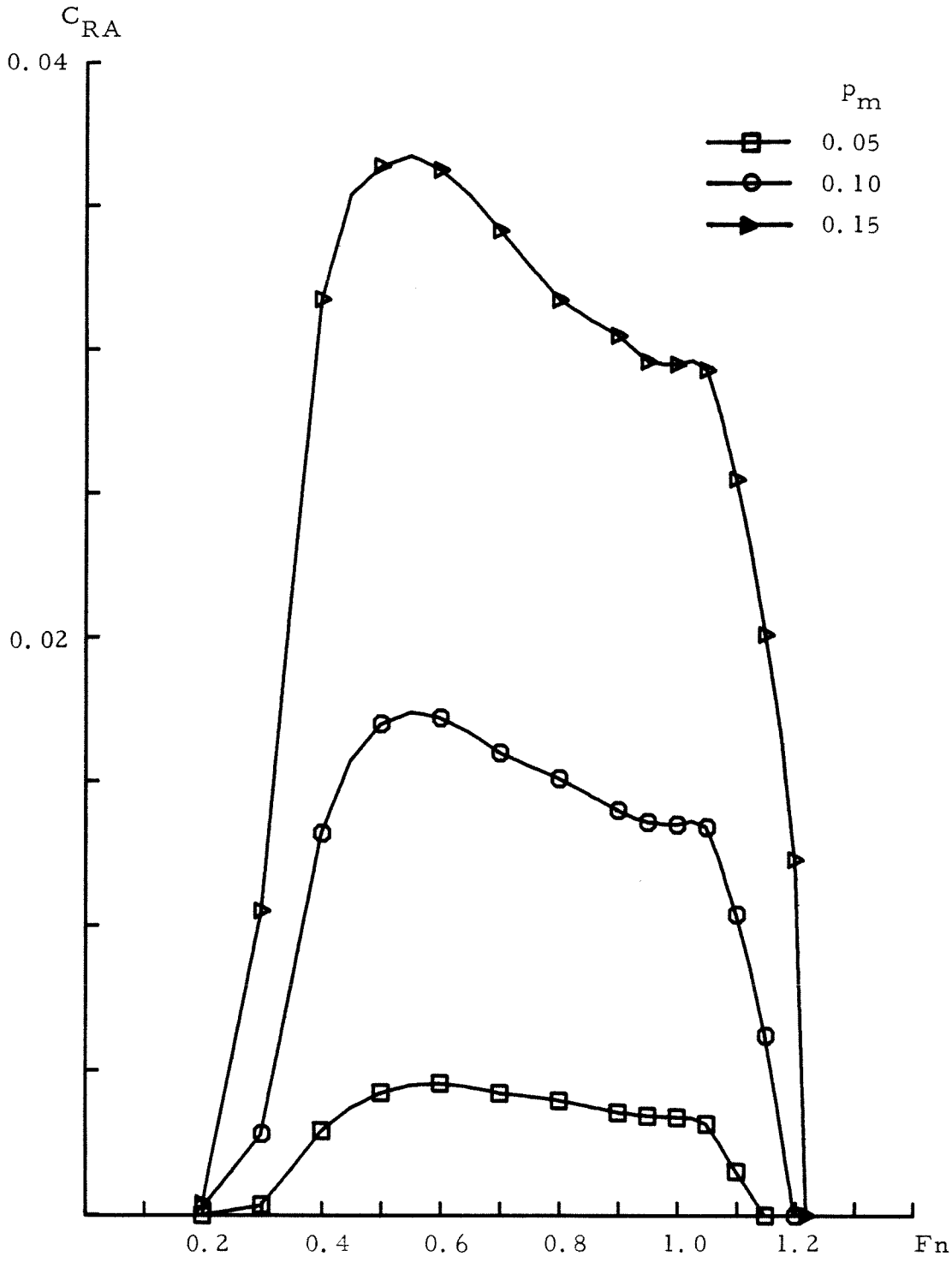

Fig. 4.4.1. Averaged wave resistance coefficient as a function of Fn for p_m = 0.05, 0.1 and 0.15.

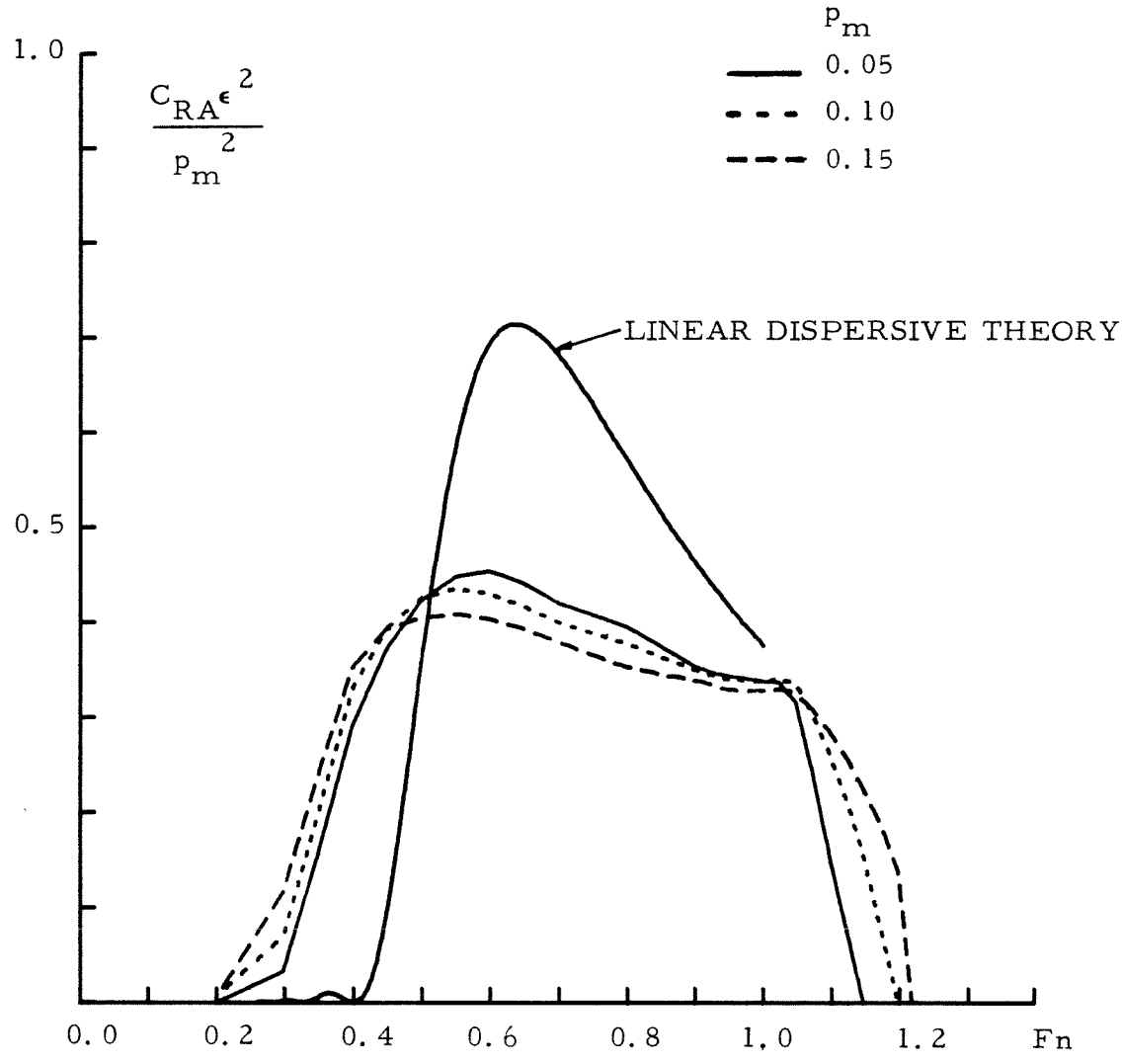

Fig. 4.4.2. Comparison of the normalized wave resistance coefficient between the nonlinear and linear theories.

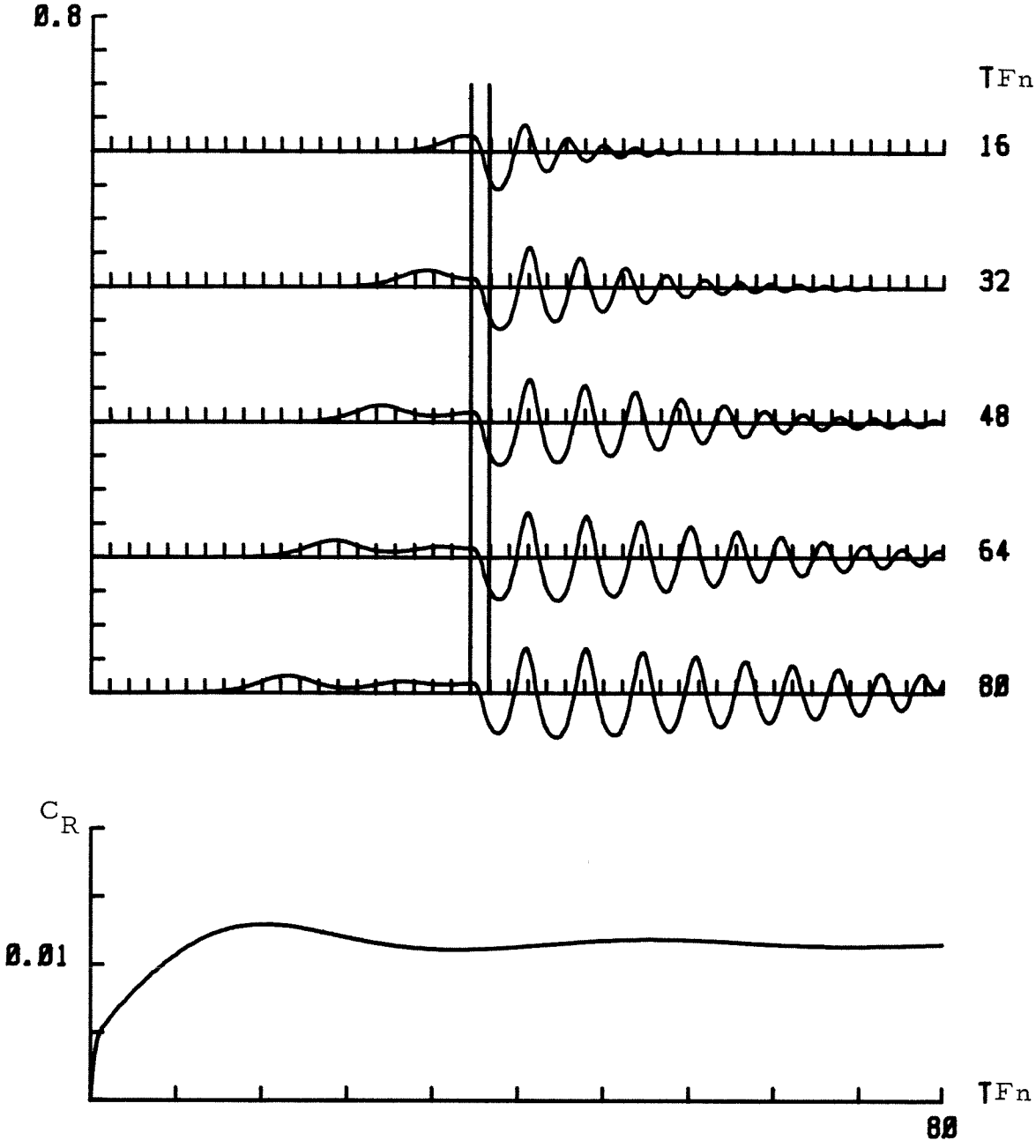

Fig. 4.5.1. The surface wave elevation and the wave resistance coefficient of the cosine disturbance given by the numerical KdV model for $p_m = 0.1$, $\epsilon = 0.5$ and Fn = 0.8.

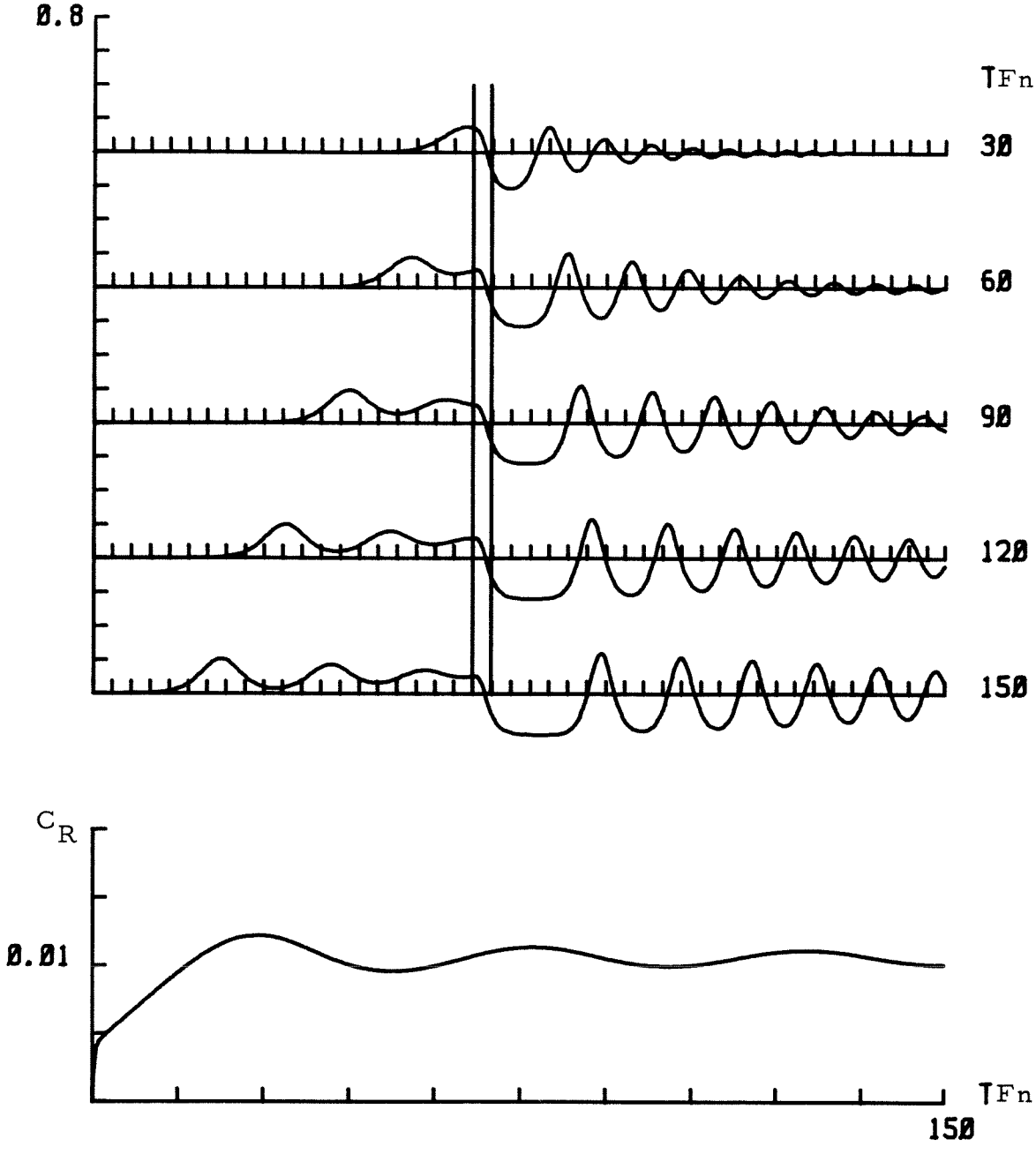

Fig. 4.5.2. The surface wave elevation and the wave resistance coefficient of the cosine disturbance given by the numerical KdV model for $p_m = 0.1$, $\epsilon = 0.5$ and Fn = 0.9.

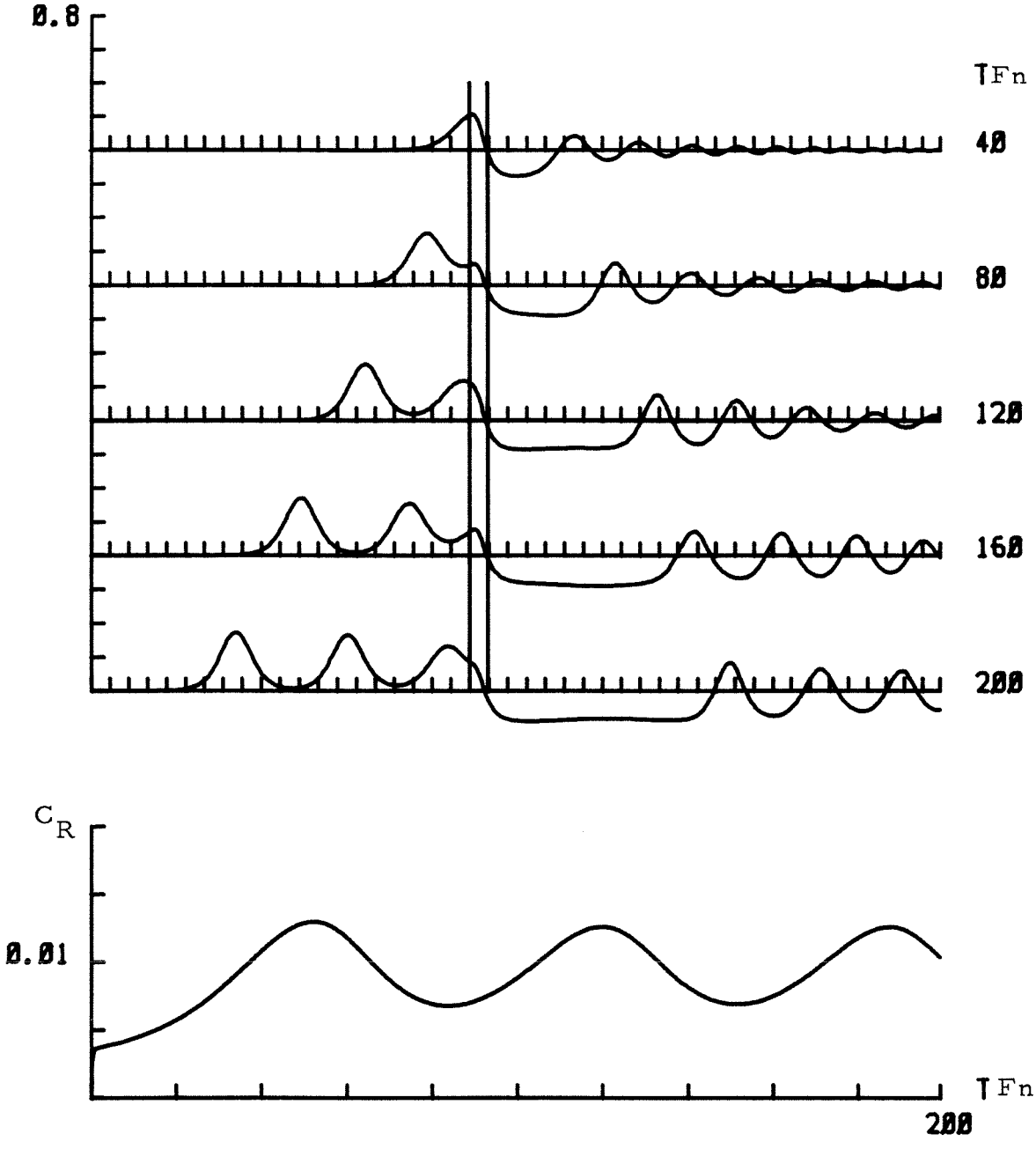

Fig. 4.5.3. The surface wave elevation and the wave resistance coefficient of the cosine disturbance given by the numerical KdV model for $p_m = 0.1$, $\epsilon = 0.5$ and Fn = 1.0.

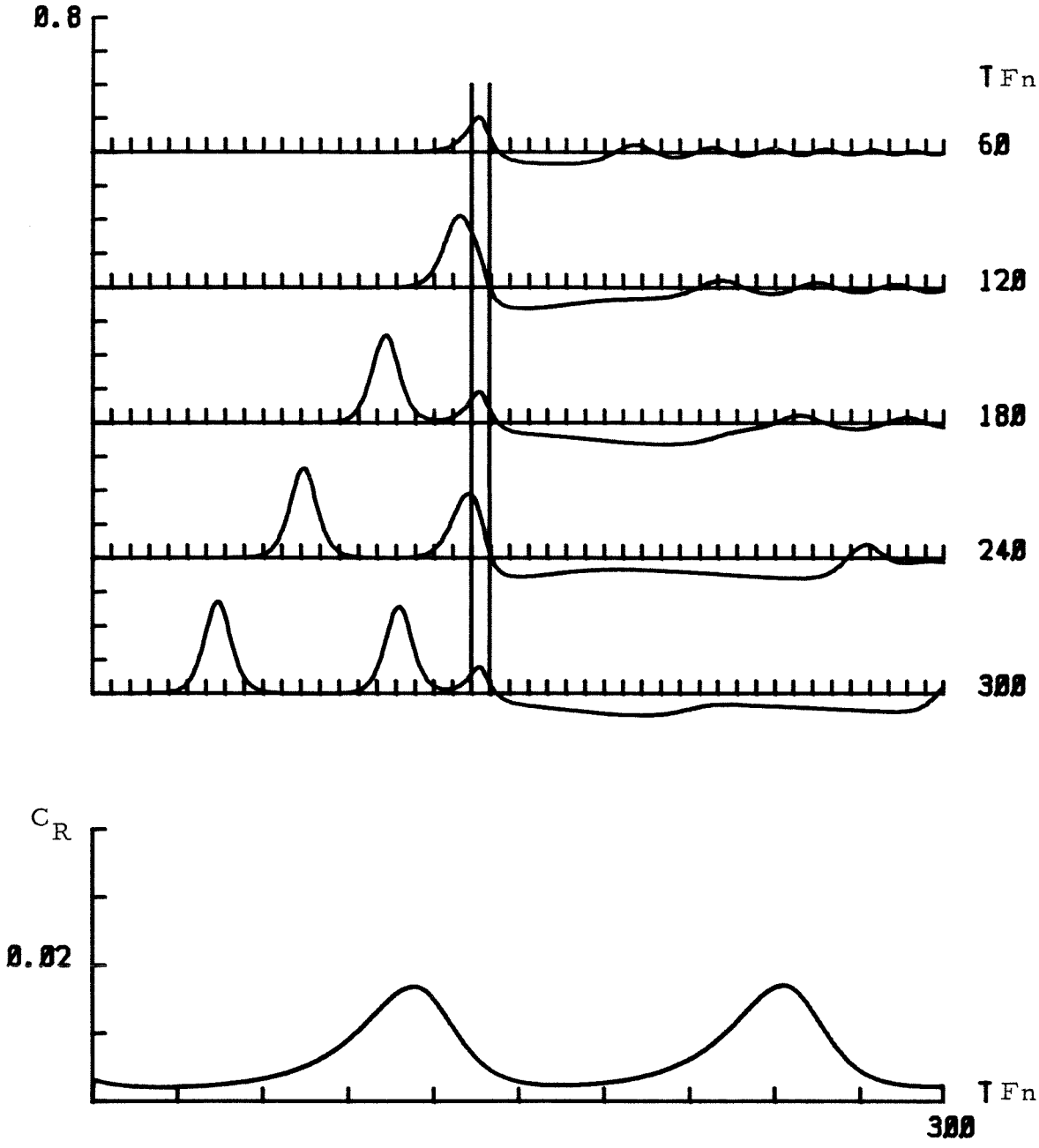

Fig. 4.5.4. The surface wave elevation and the wave resistance coefficient of the cosine disturbance given by the numerical KdV model for $p_m = 0.1$, $\epsilon = 0.5$ and Fn = 1.1.

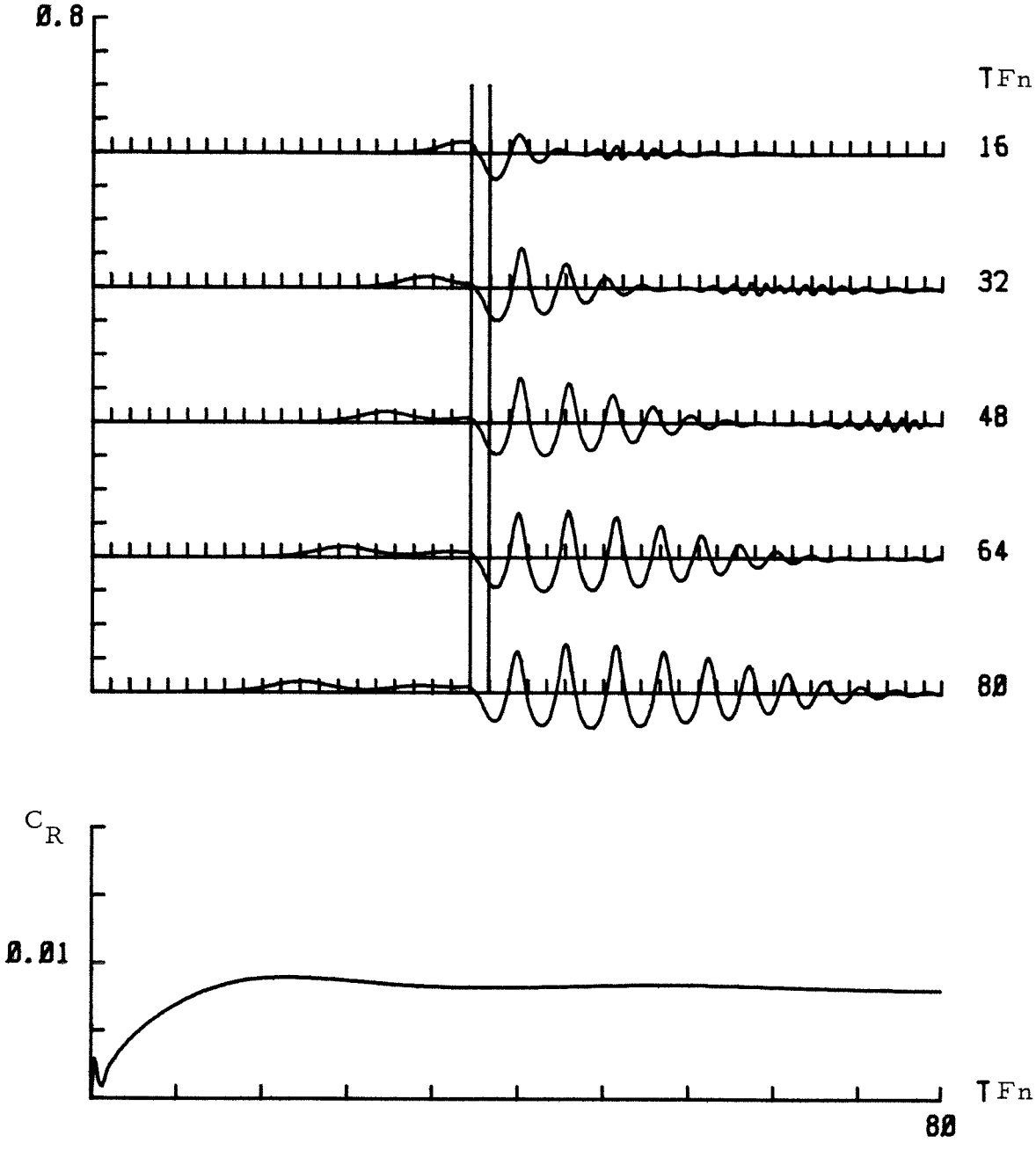

Fig. 4.6.1. The surface wave elevation and the wave resistance coefficient of the cosine bottom bump given by the numerical Boussinesq model for $p_m = 0.1$, $\epsilon = 0.5$ and $Fn = 0.8$.

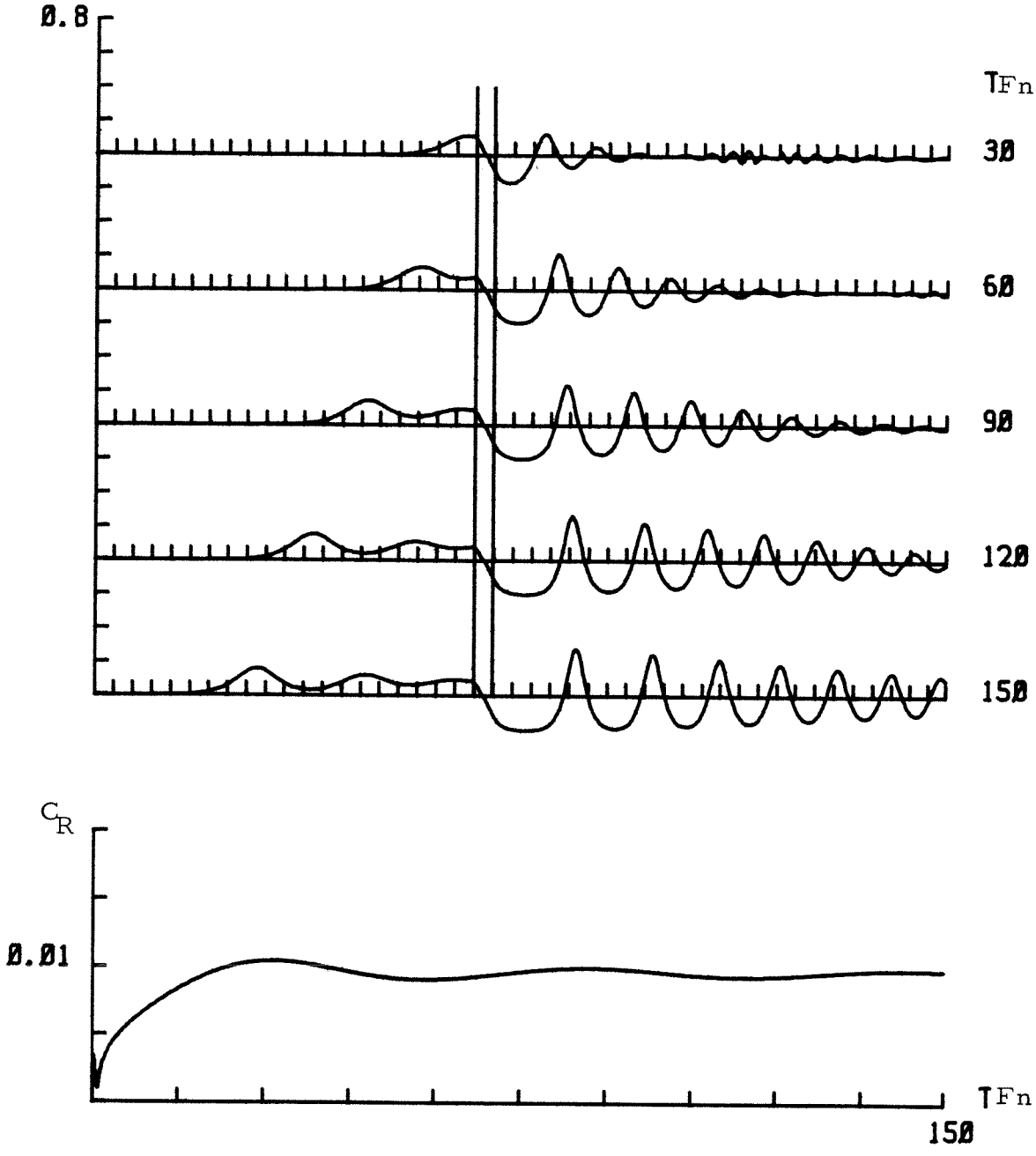

Fig. 4.6.2. The surface wave elevation and the wave resistance coefficient of the cosine bottom bump given by the numerical Boussinesq model for $p_m = 0.1$, $\epsilon = 0.5$ and $Fn = 0.9$.

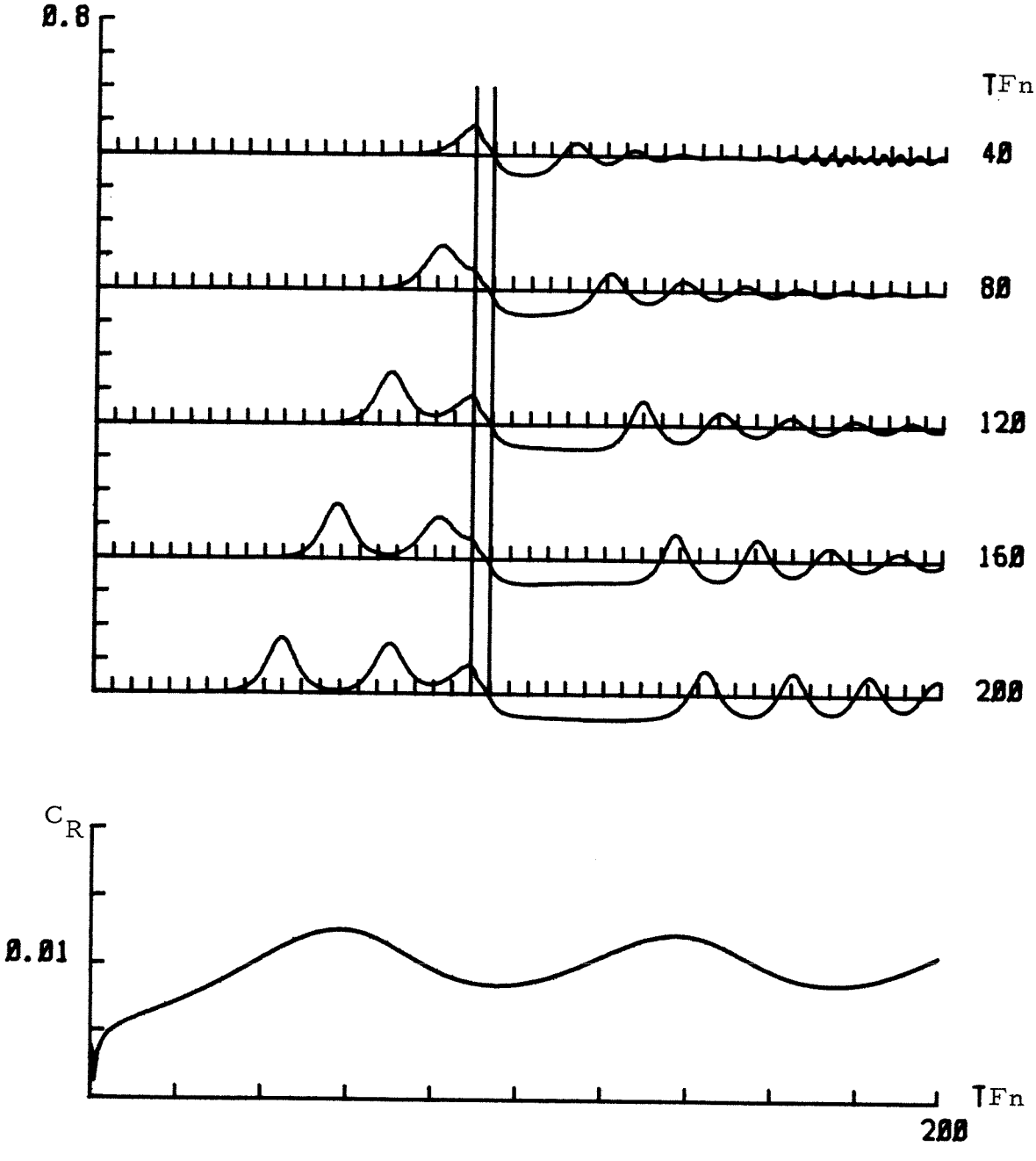

Fig. 4.6.3. The surface wave elevation and the wave resistance coefficient of the cosine bottom bump given by the numerical Boussinesq model for $p_m = 0.1$, $\epsilon = 0.5$ and $Fn = 1.0$.

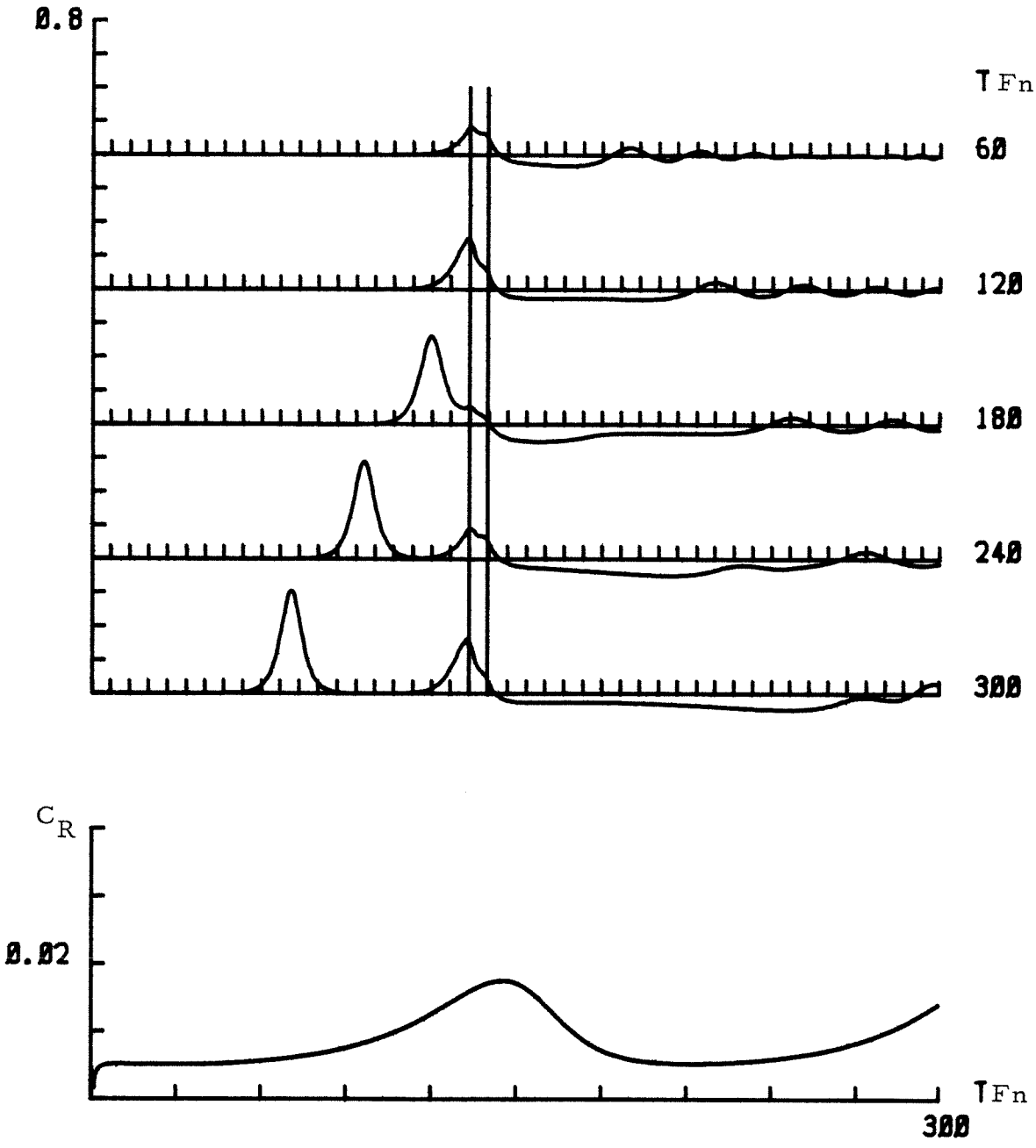

Fig. 4.6.4. The surface wave elevation and the wave resistance coefficient of the cosine bottom bump given by the numerical Boussinesq model for $p_m = 0.1$, $\epsilon = 0.5$ and Fn = 1.1.

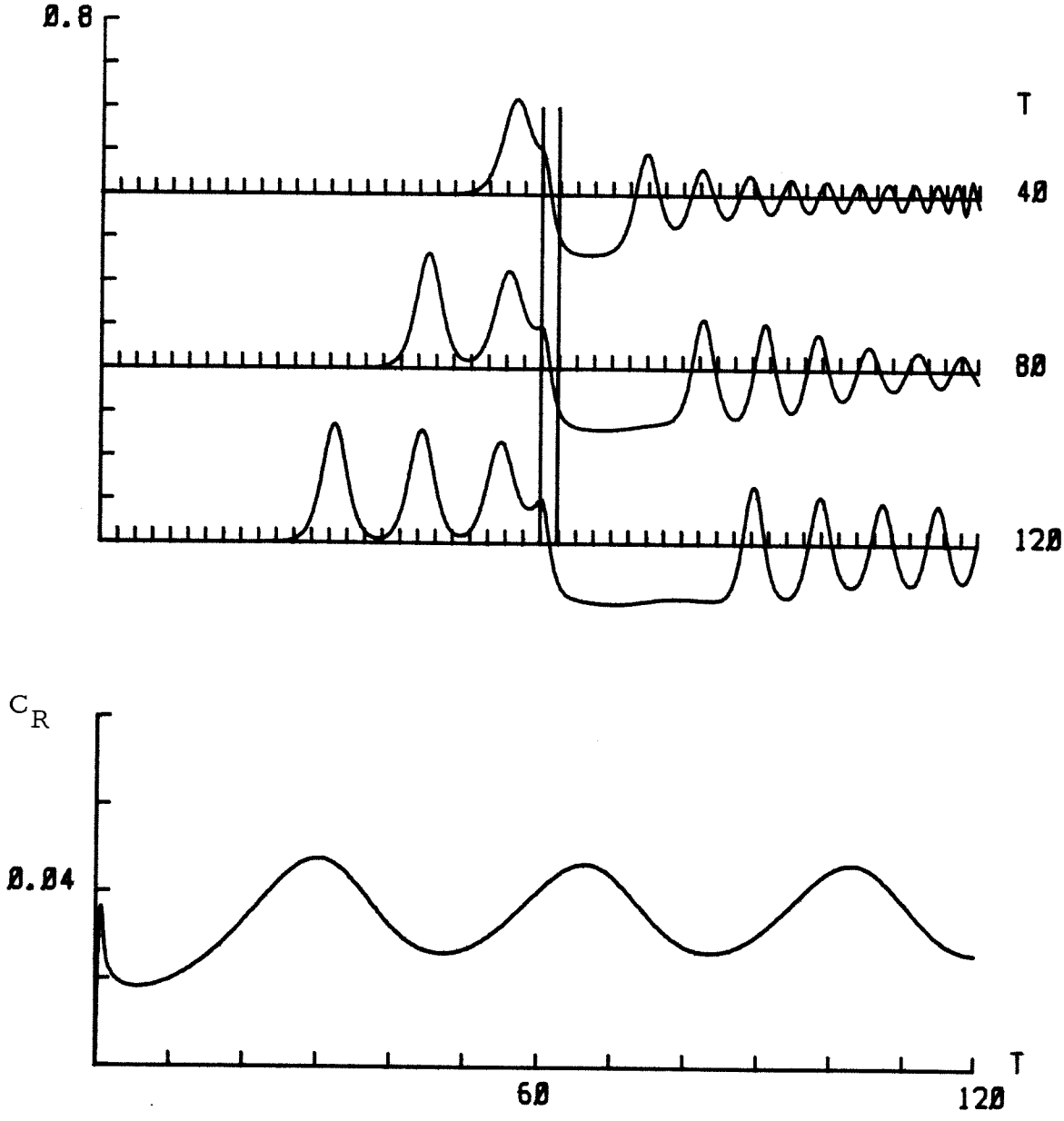

Fig. 4.7.1. The surface wave elevation and the wave resistance coefficient of the cosine disturbance given by the numerical KdV model for $p_m = 0.2$, $\epsilon = 0.5$ and Fn = 1.0.

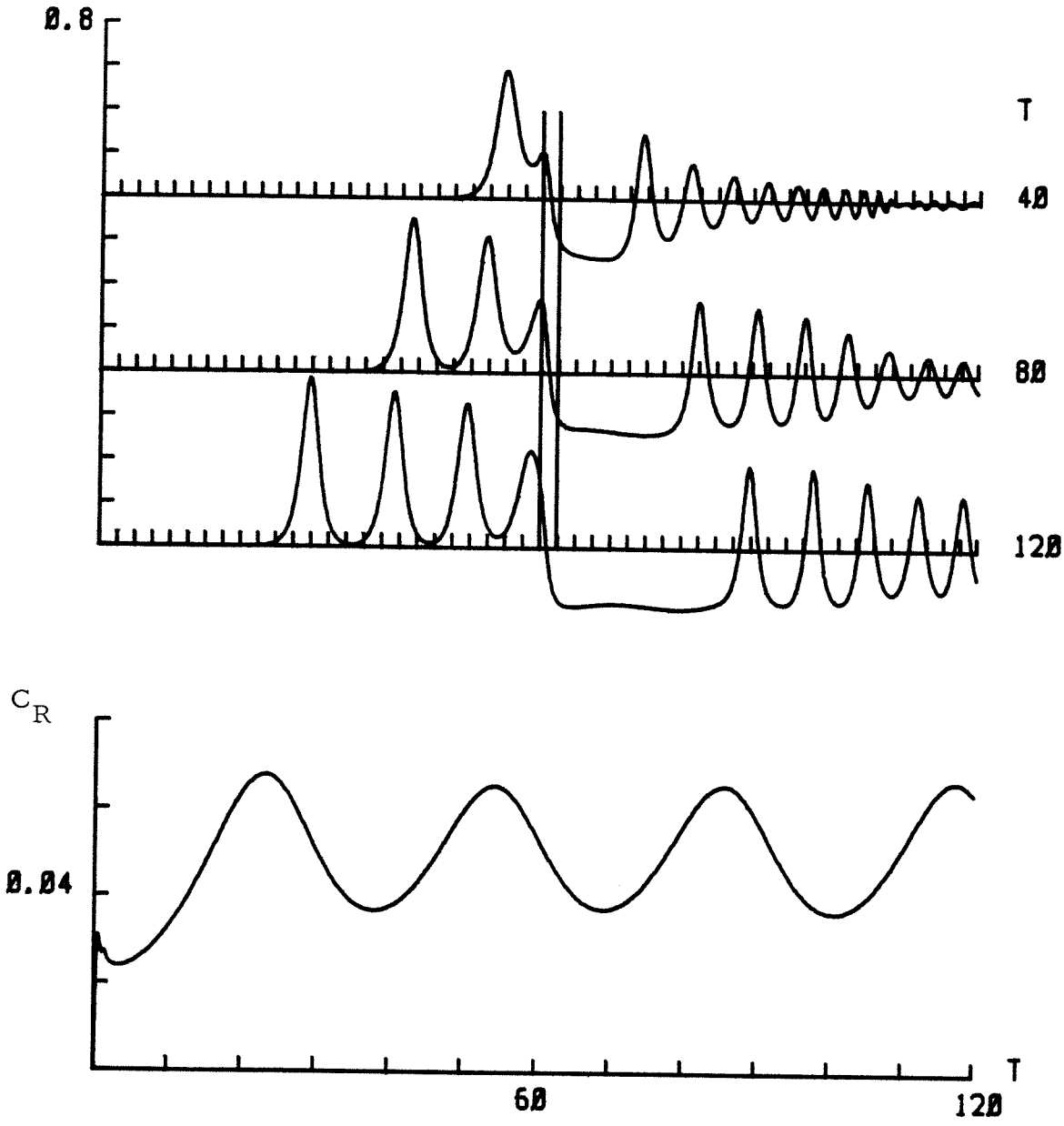

Fig. 4.7.2. The surface wave elevation and the wave resistance coefficient of the cosine surface pressure given by the numerical Boussinesq model for $p_m = 0.2$, $\epsilon = 0.5$ and $Fn = 1.0$.

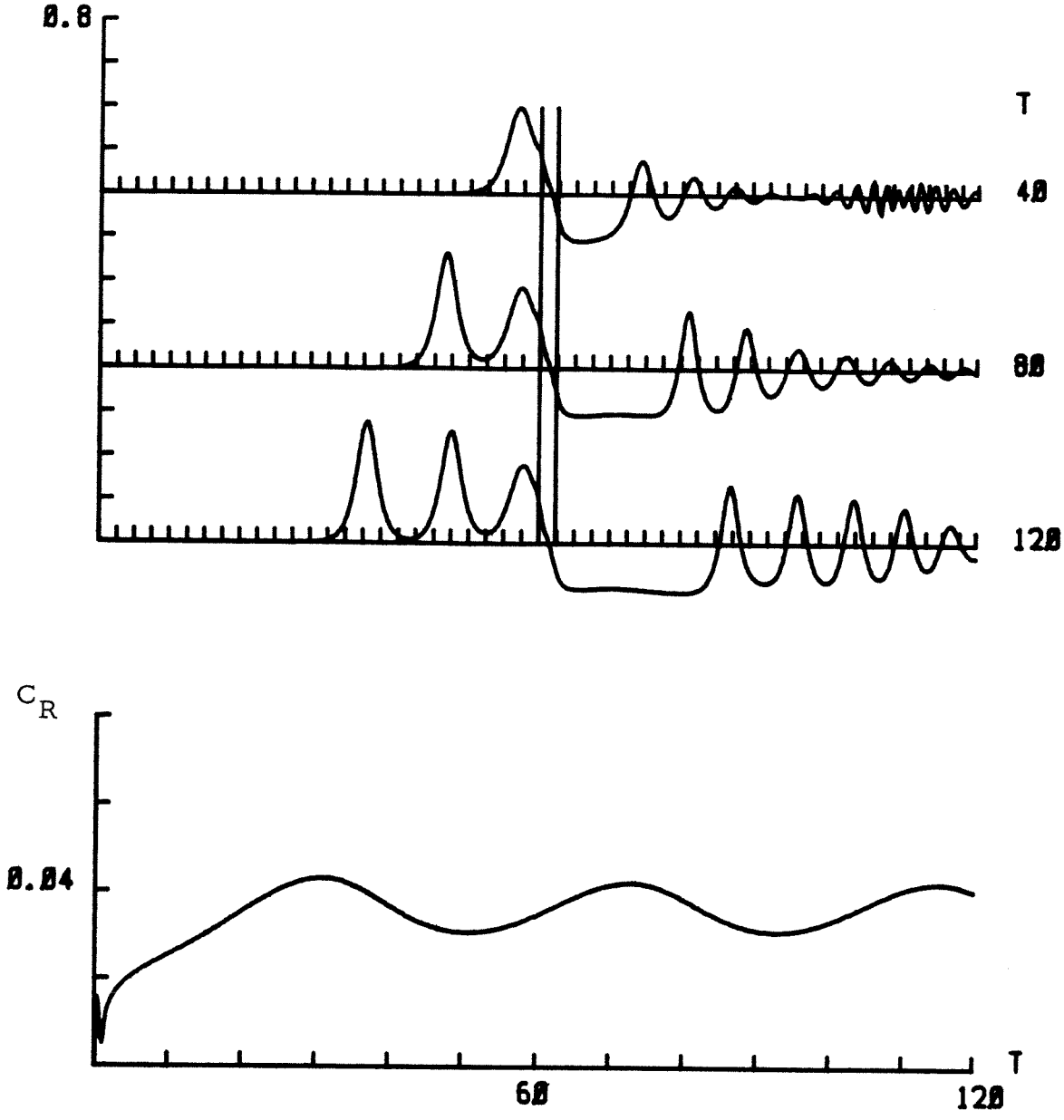

Fig. 4.7.3. The surface wave elevation and the wave resistance coefficient of the cosine bottom bump given by the numerical Boussinesq model for $b_m = 0.2$, $\epsilon = 0.5$ and $Fn = 1.0$.

Note: Holder is made of Plexiglass. Lengths are given in cm.

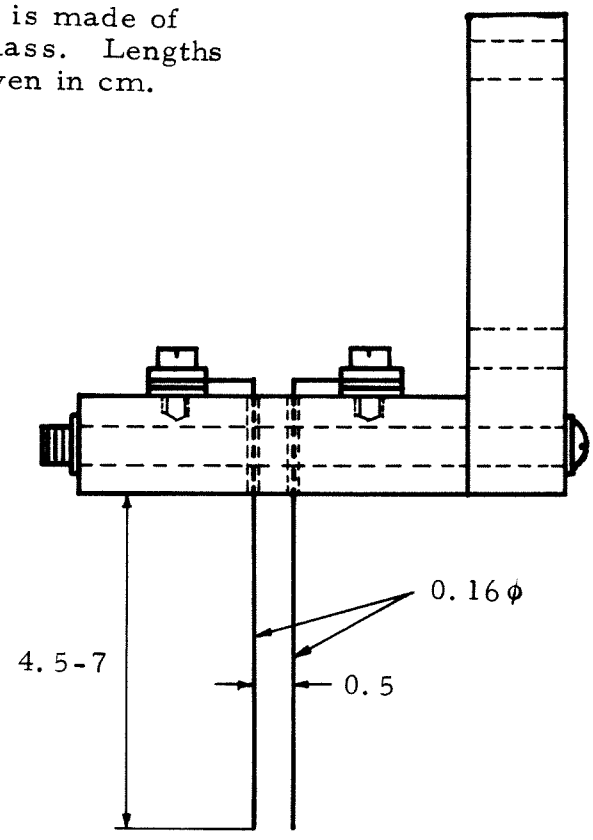

Fig. 5.1.1. Drawing of a typical wave gage.

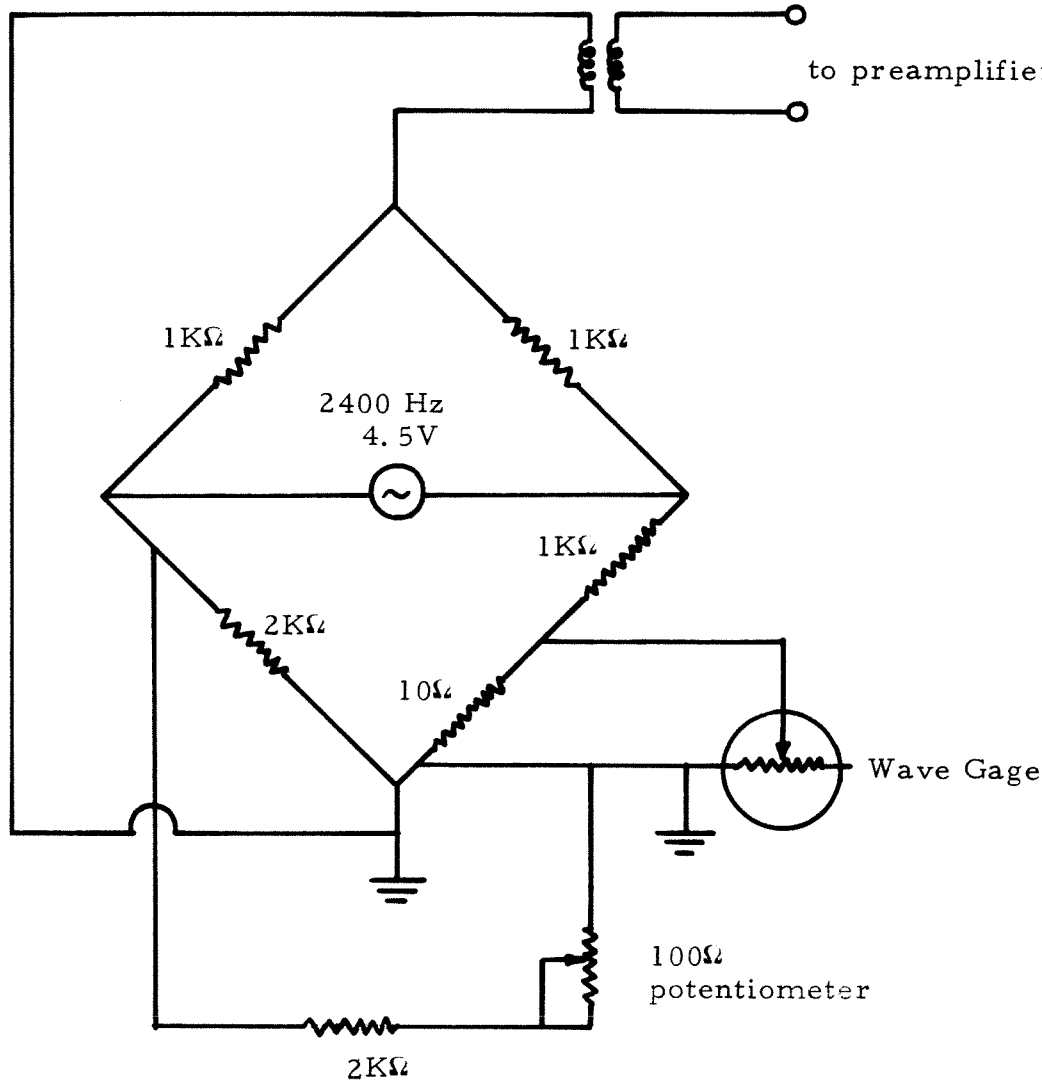

Fig. 5.1.2. Circuit diagram for wave gages.

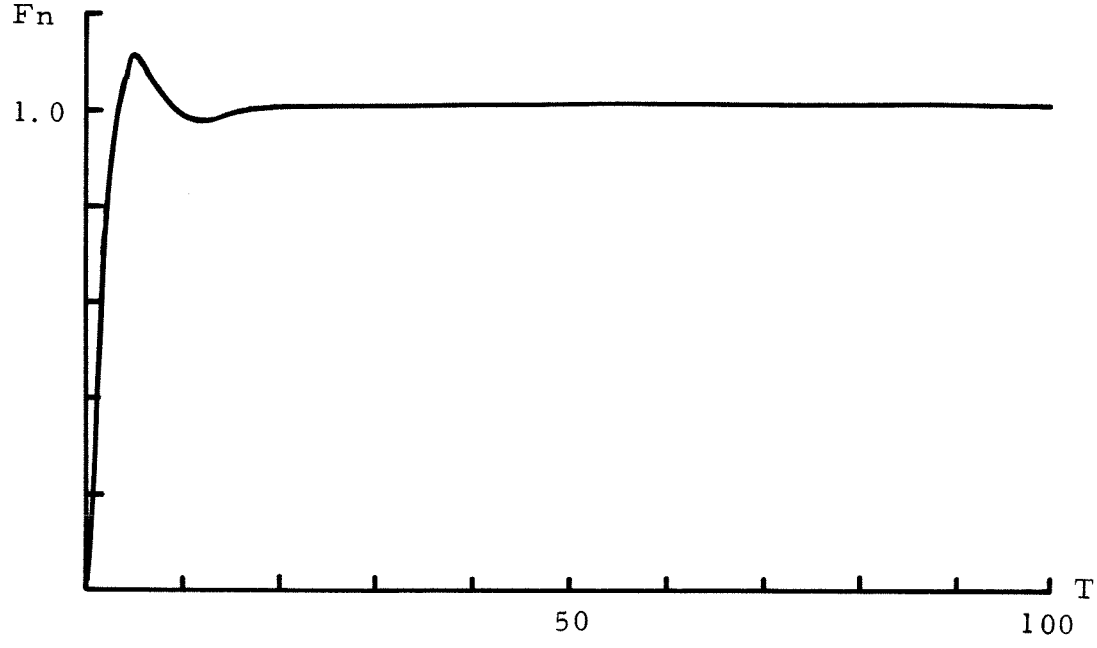

Fig. 5.1.3. Typical shape of speed vs. time curve obtained in the experiments.

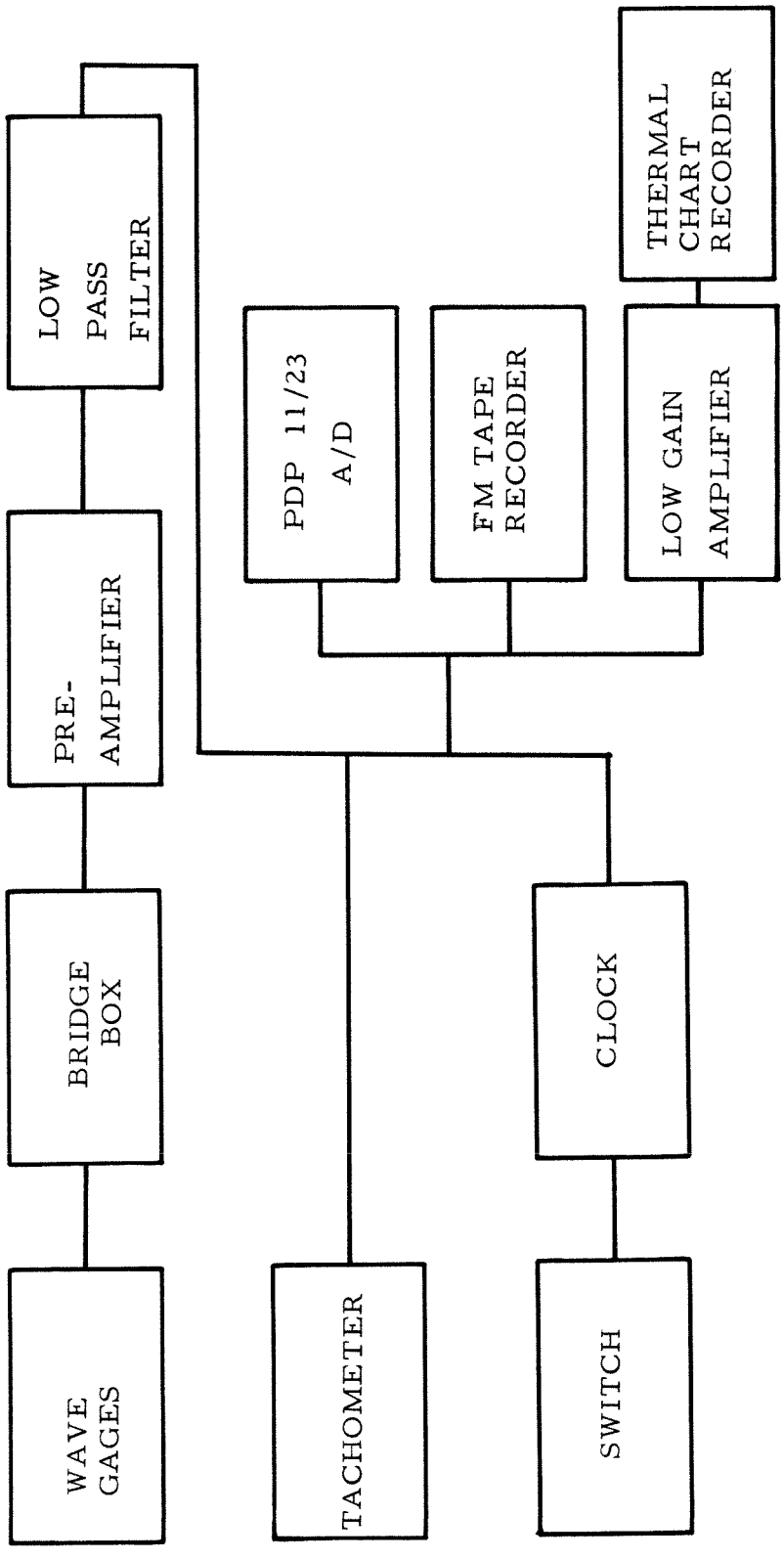

Fig. 5.1.4. Block diagram of the experimental setup.

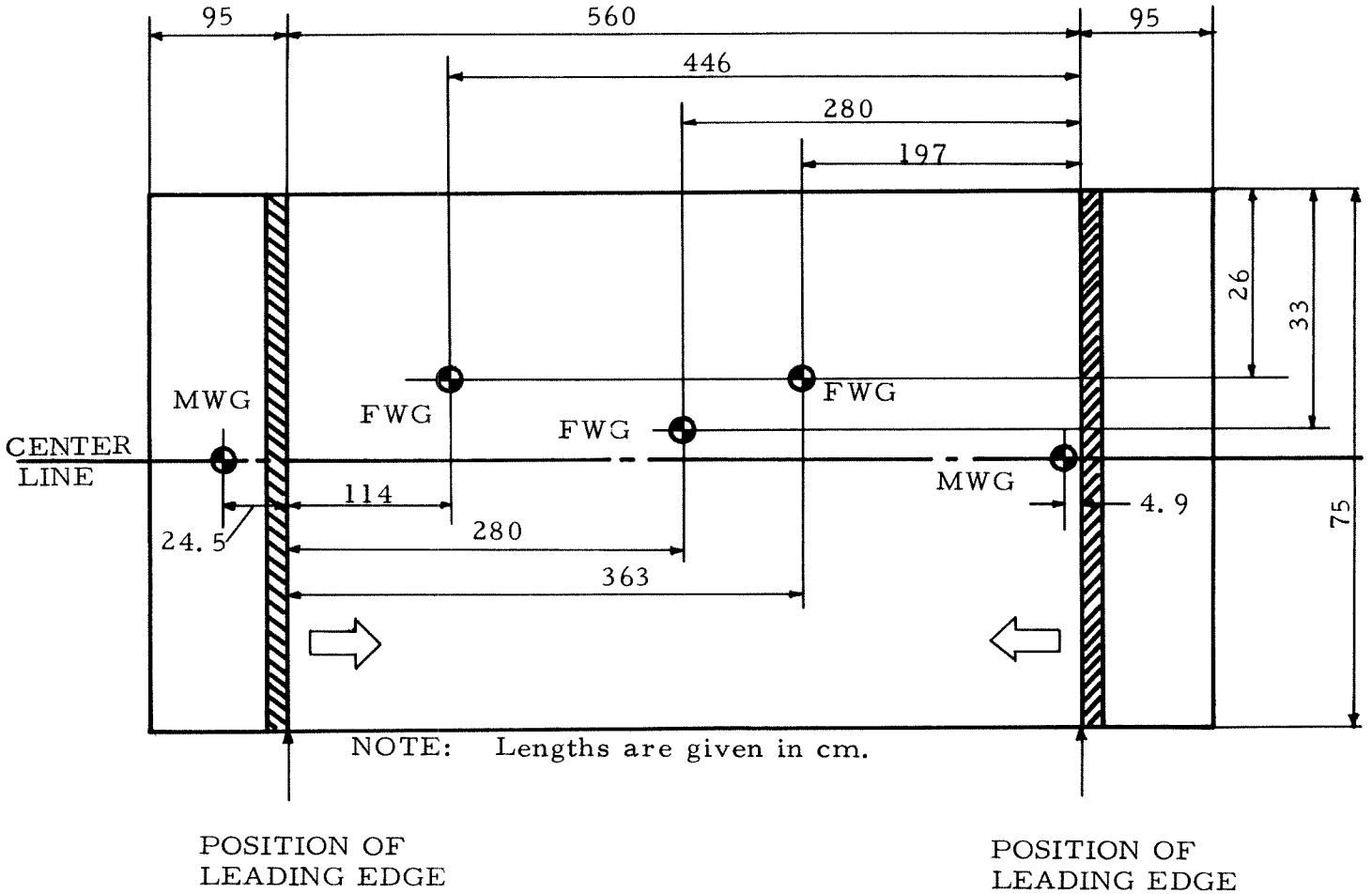

Fig. 5.1.5. Locations of the wave gages.

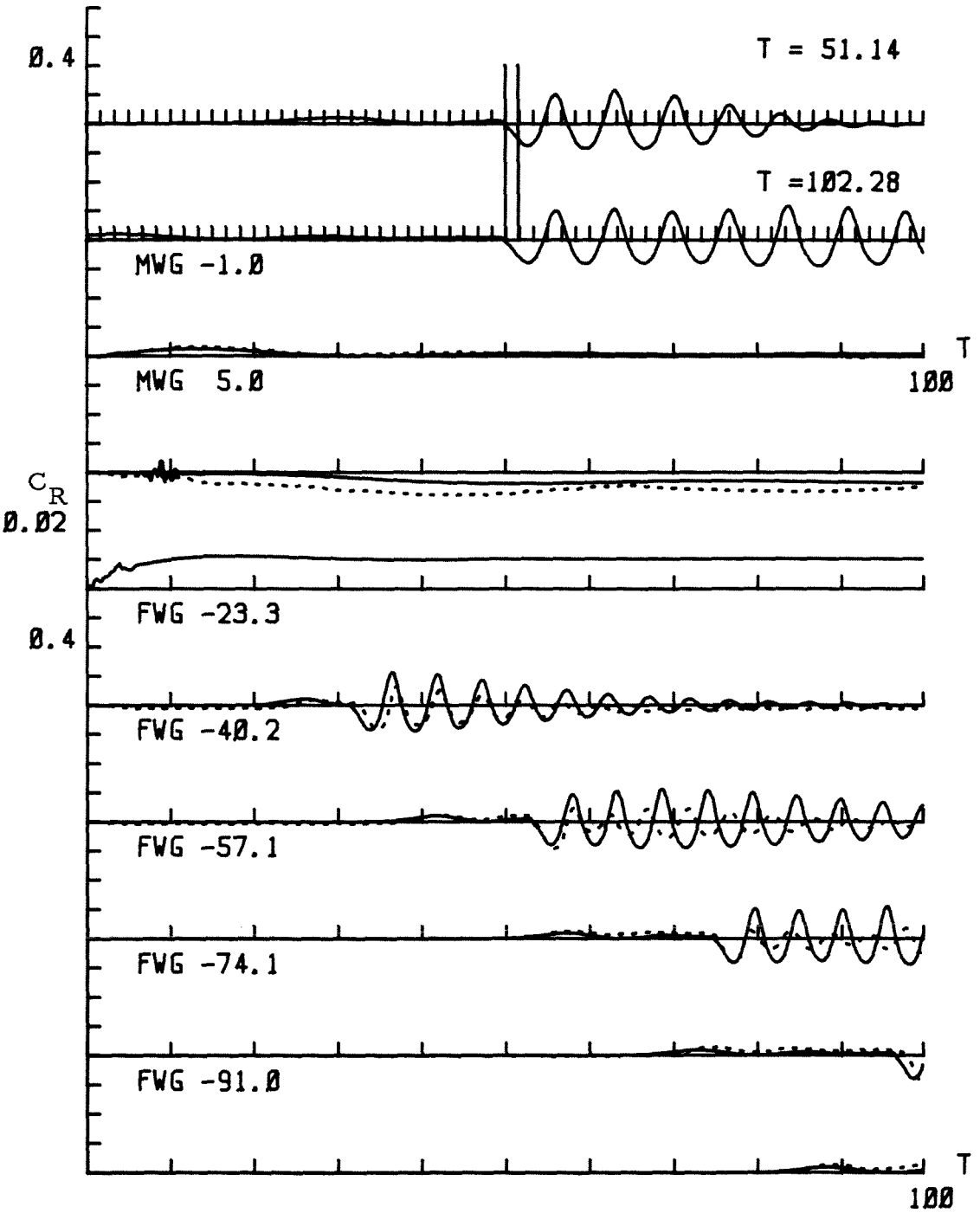

Fig. 5.2.1. Comparison of the surface elevations between the experimental data and the numerical solution given by the Boussinesq model for $Fn = 0.72$, $b_m = 0.15$ and $\epsilon = 1.09$.

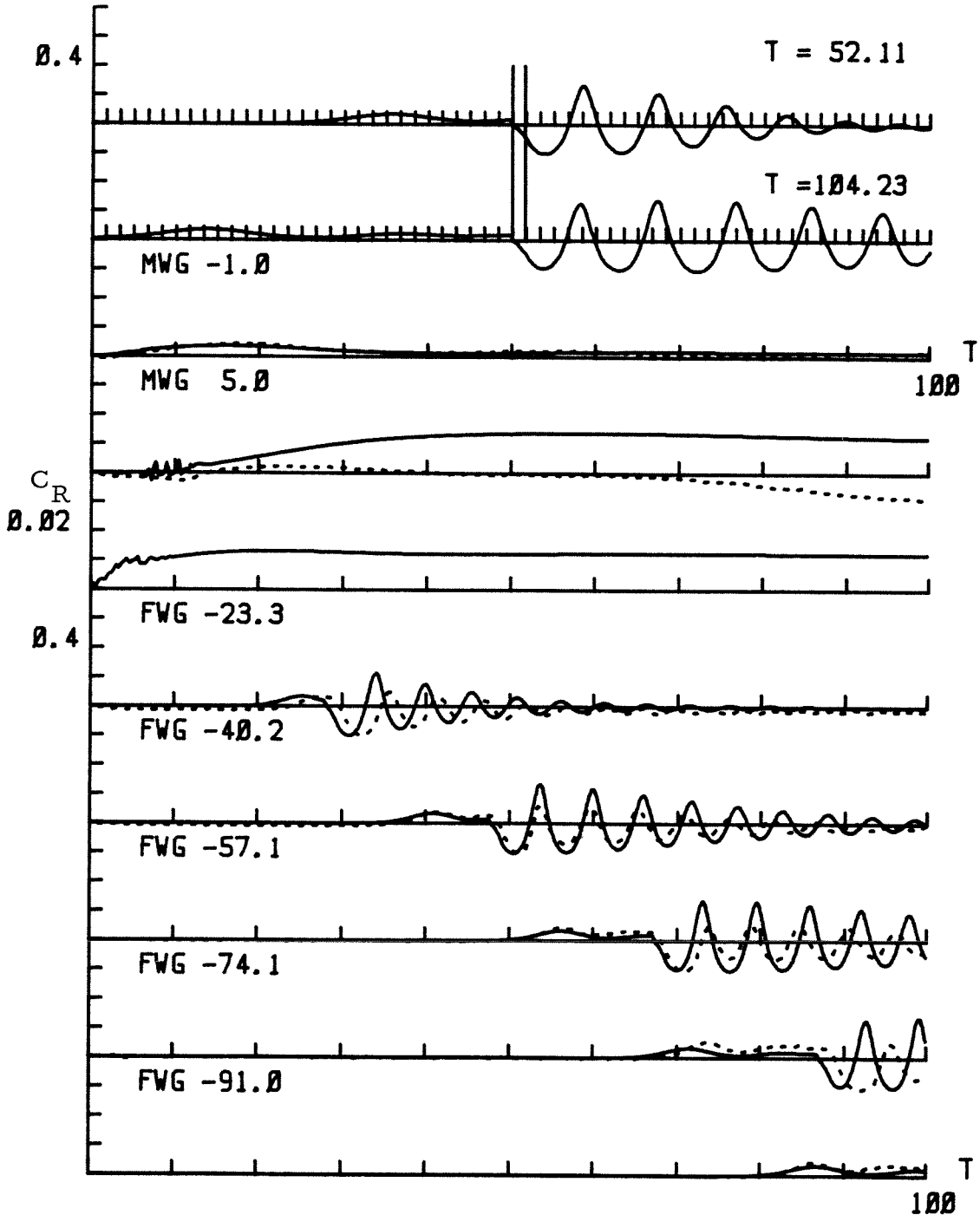

Fig. 5.2.2. Comparison of the surface elevations between the experimental data and the numerical solution given by the Boussinesq model for Fn = 0.79, b_m = 0.15 and ϵ = 1.09.

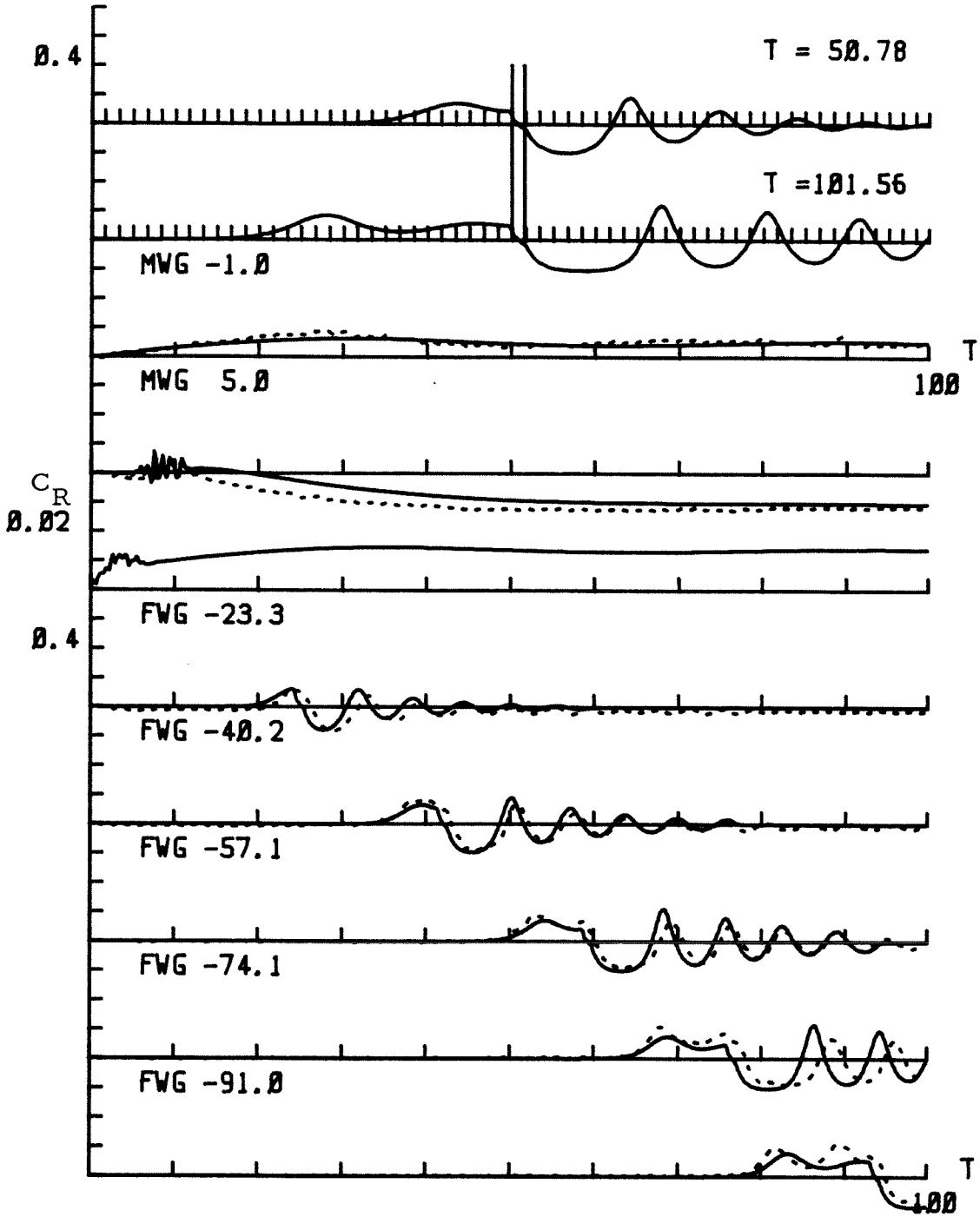

Fig. 5.2.3. Comparison of the surface elevations between the experimental data and the numerical solution given by the Boussinesq model for Fn = 0.90, b_m = 0.15 and ϵ = 1.09.

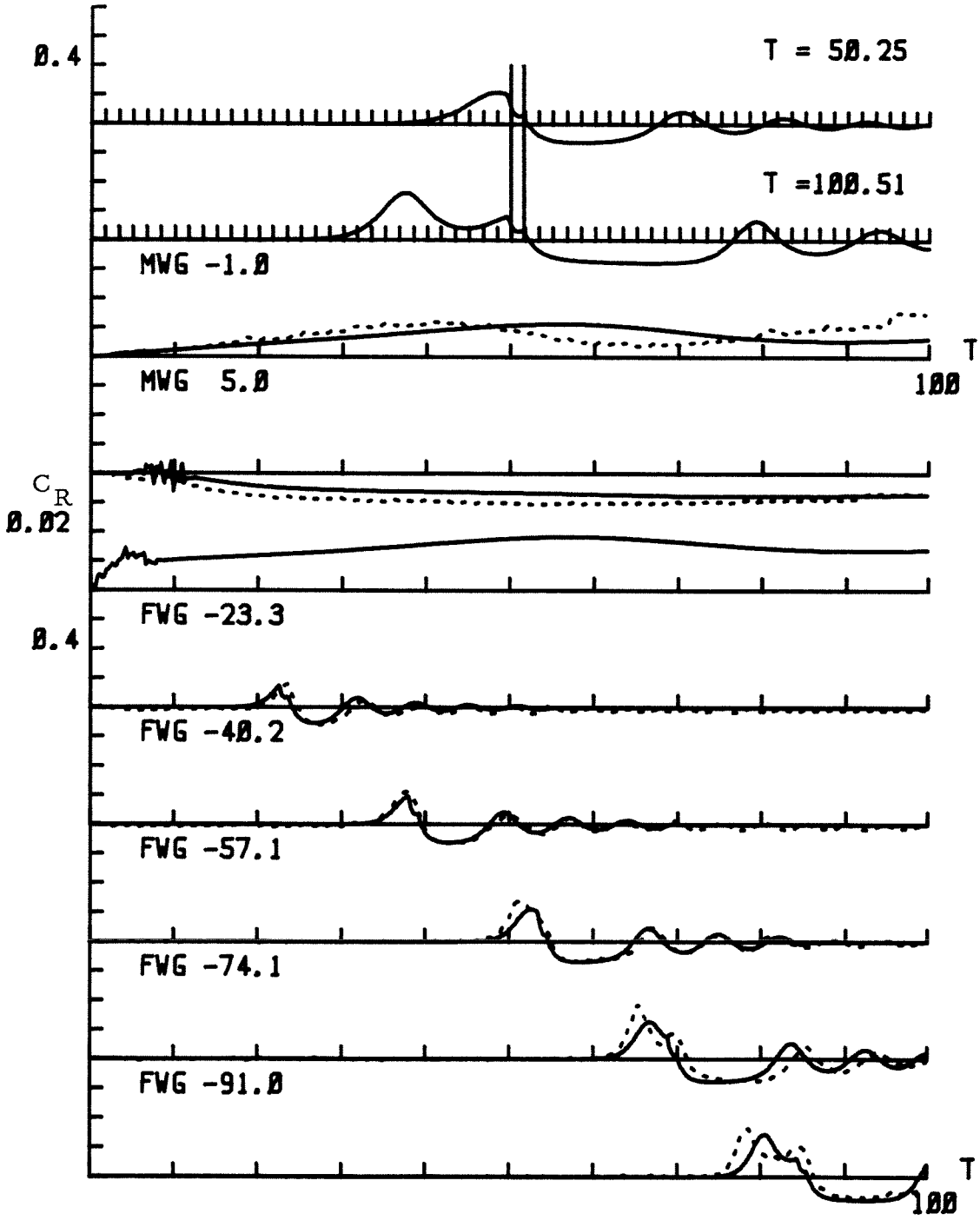

Fig. 5.2.4. Comparison of the surface elevations between the experimental data and the numerical solution given by the Boussinesq model for Fn = 1.01, b_m = 0.15 and ϵ = 1.09.

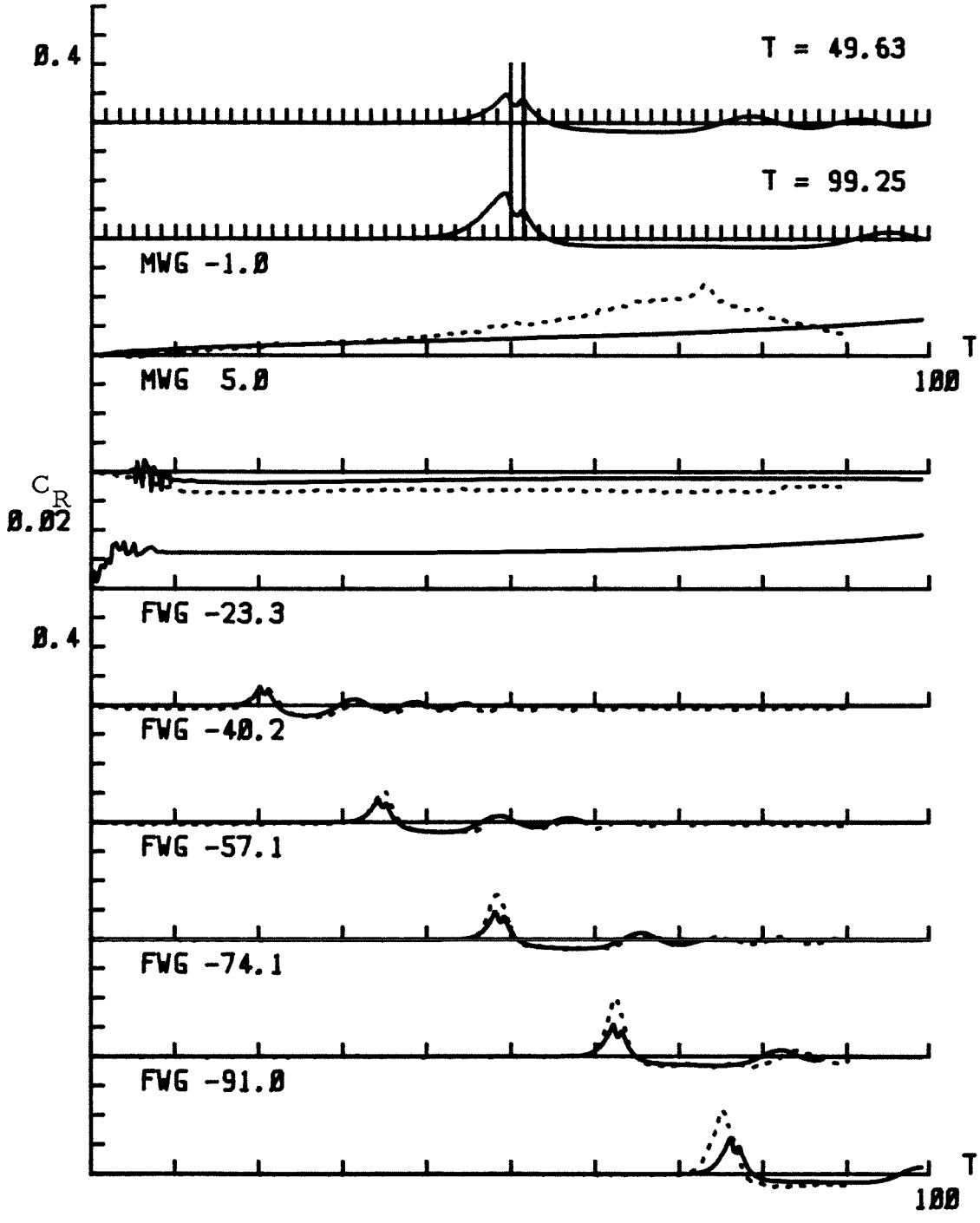

Fig. 5.2.5. Comparison of the surface elevations between the experimental data and the numerical solution given by the Boussinesq model for Fn = 1.11, b_m = 0.15 and ϵ = 1.09.

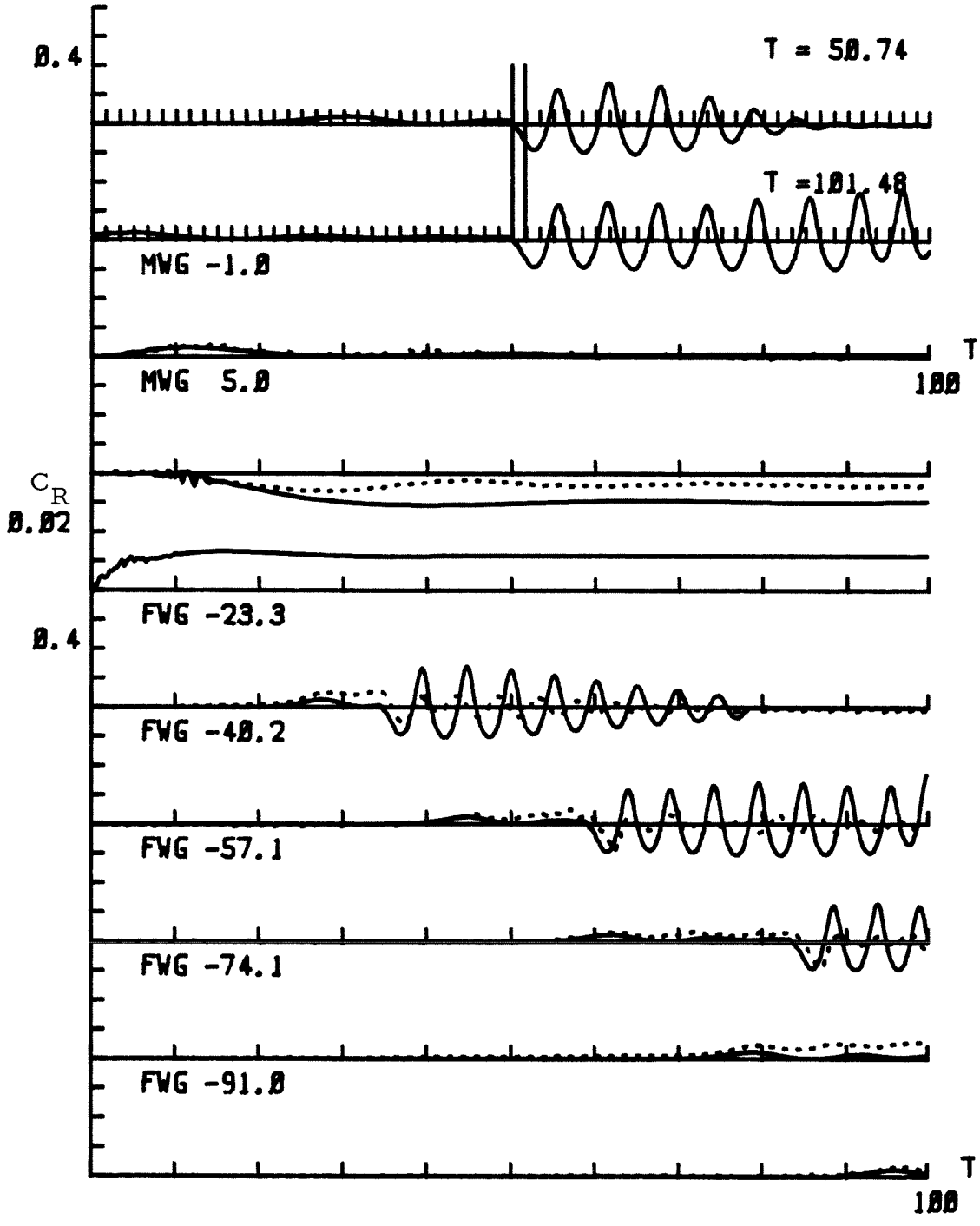

Fig. 5.2.6. Comparison of the surface elevations between the experimental data and the numerical solution given by the Boussinesq model for Fn = 0.70, b_m = 0.166 and ϵ = 0.99.

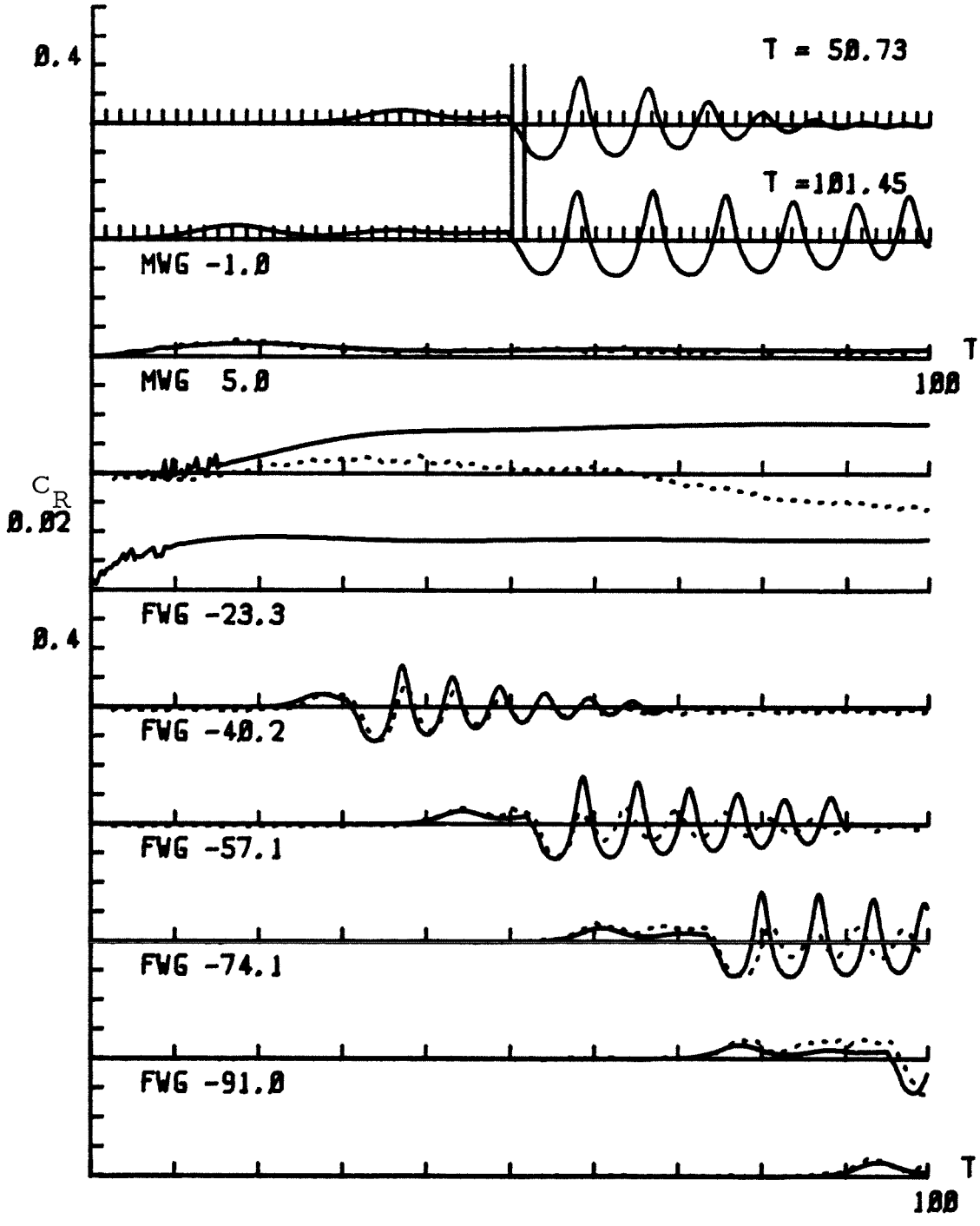

Fig. 5.2.7. Comparison of the surface elevations between the experimental data and the numerical solution given by the Boussinesq model for Fn = 0.80, b_m = 0.166 and ϵ = 0.99.

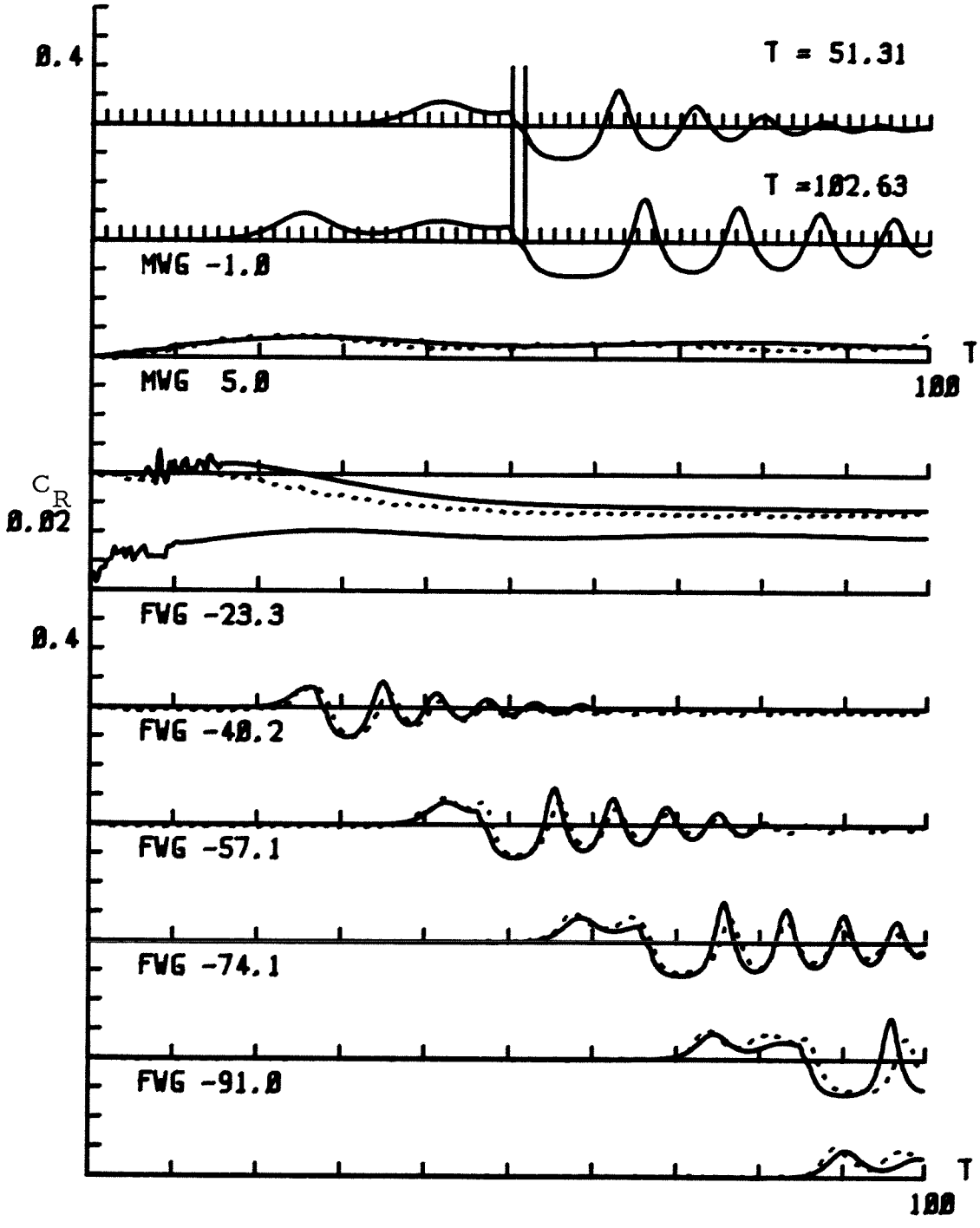

Fig. 5.2.8. Comparison of the surface elevations between the experimental data and the numerical solution given by the Boussinesq model for Fn = 0.89, b_m = 0.166 and ϵ = 0.99.

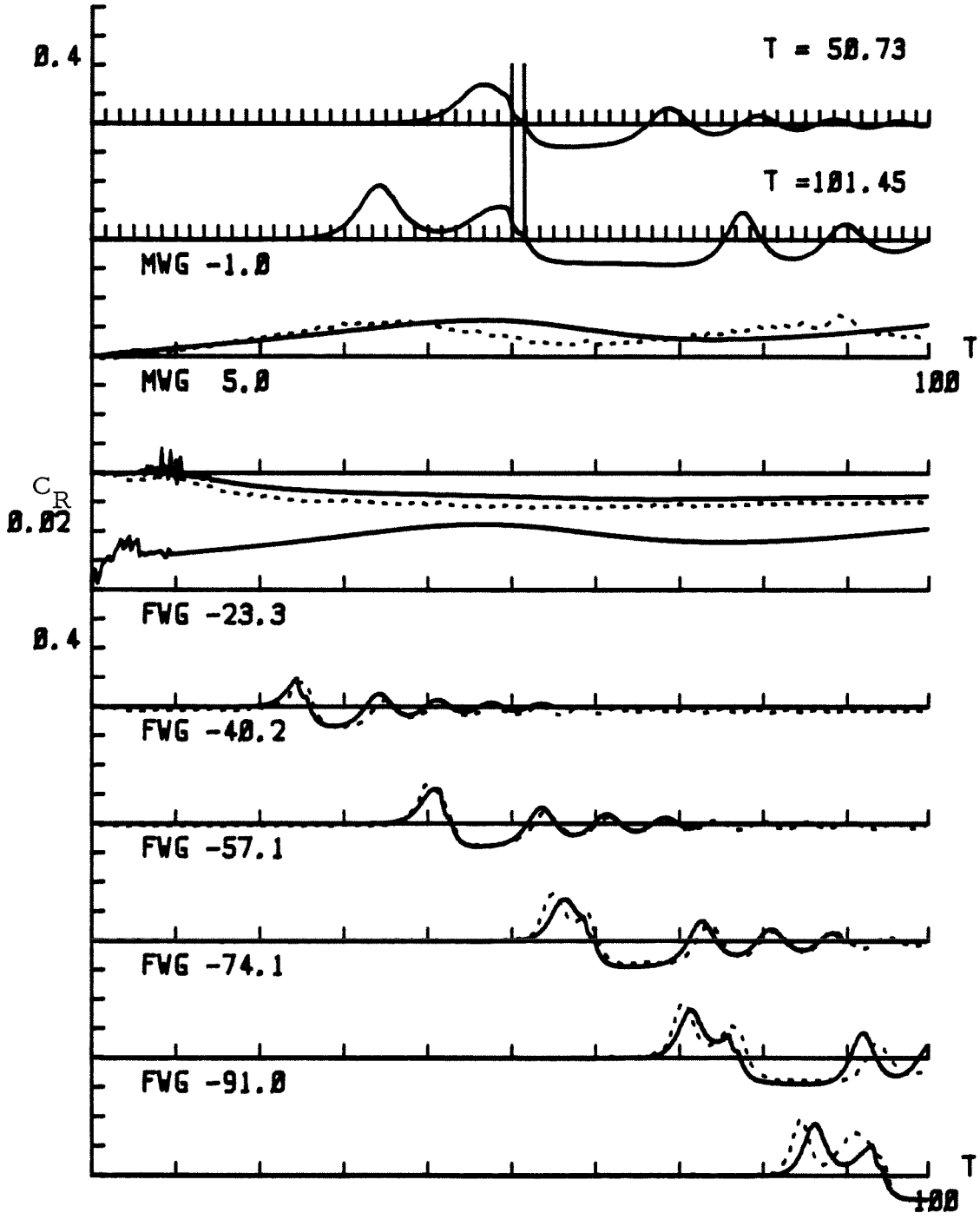

Fig. 5.2.9. Comparison of the surface elevations between the experimental data and the numerical solution given by the Boussinesq model for Fn = 1.00, b_m = 0.166 and ϵ = 0.99.

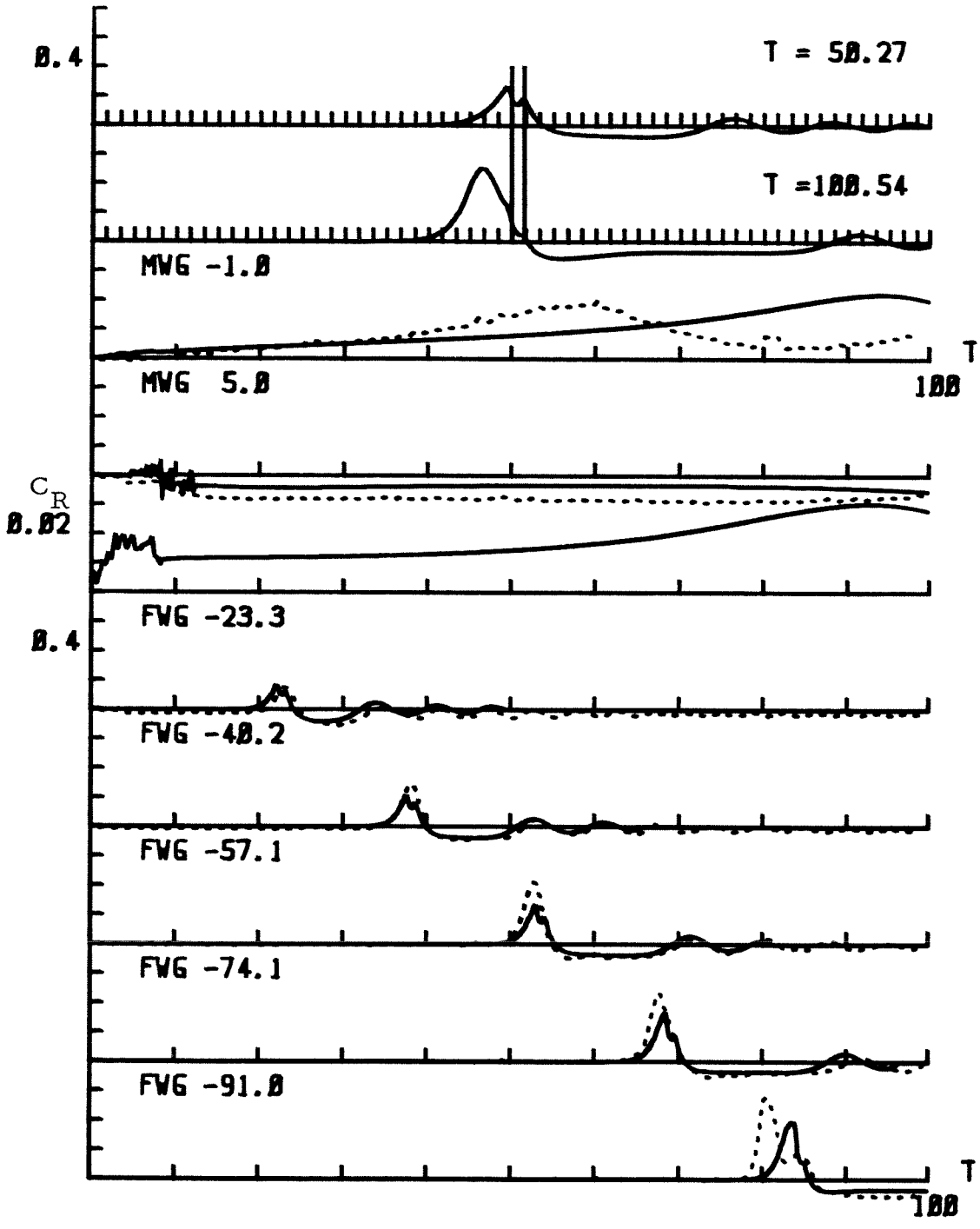

Fig. 5.2.10. Comparison of the surface elevations between the experimental data and the numerical solution given by the Boussinesq model for Fn = 1.11, b_m = 0.166 and ϵ = 0.99.

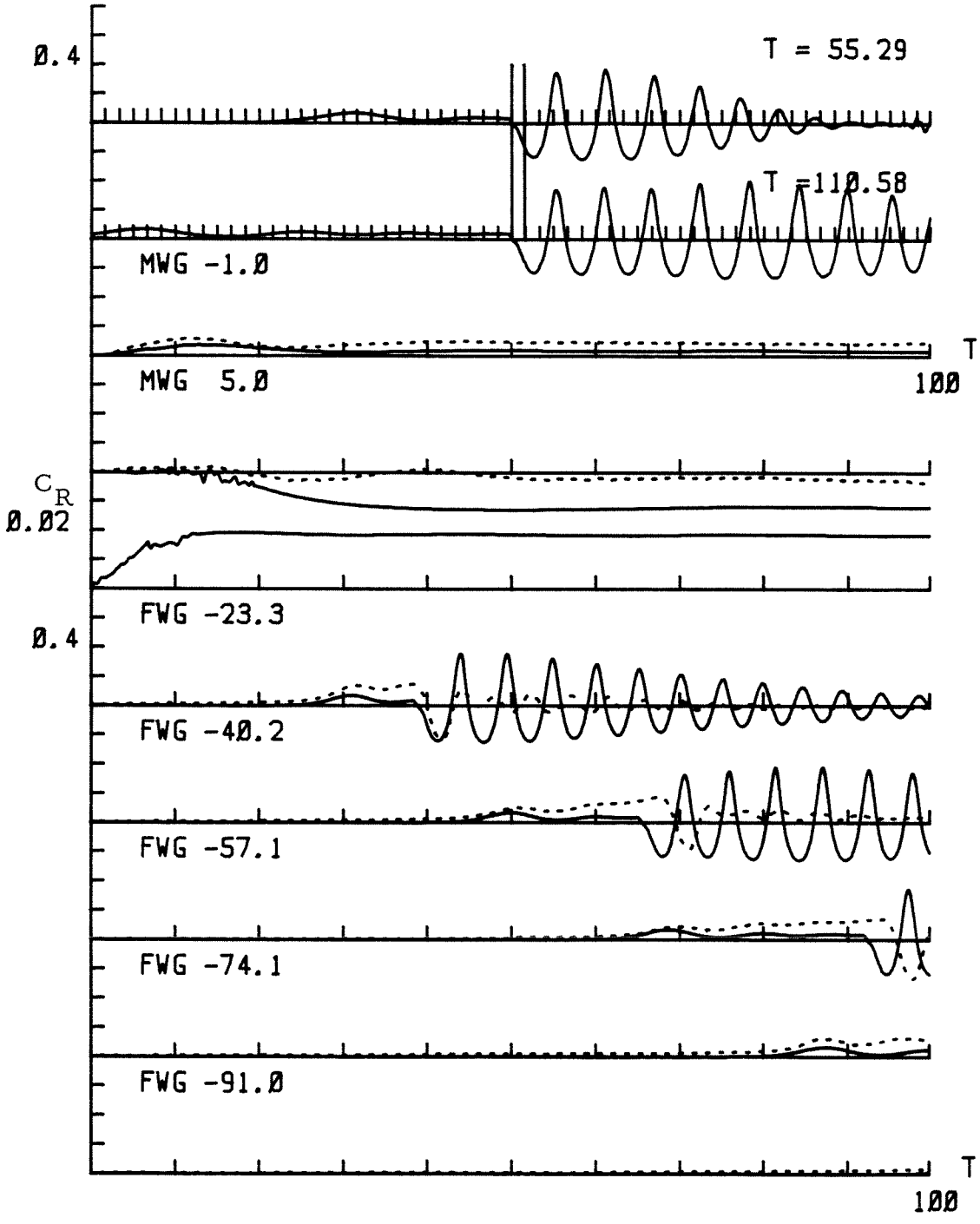

Fig. 5.2.11. Comparison of the surface elevations between the experimental data and the numerical solution given by the Boussinesq model for Fn = 0.72, b_m = 0.185 and ϵ = 0.88.

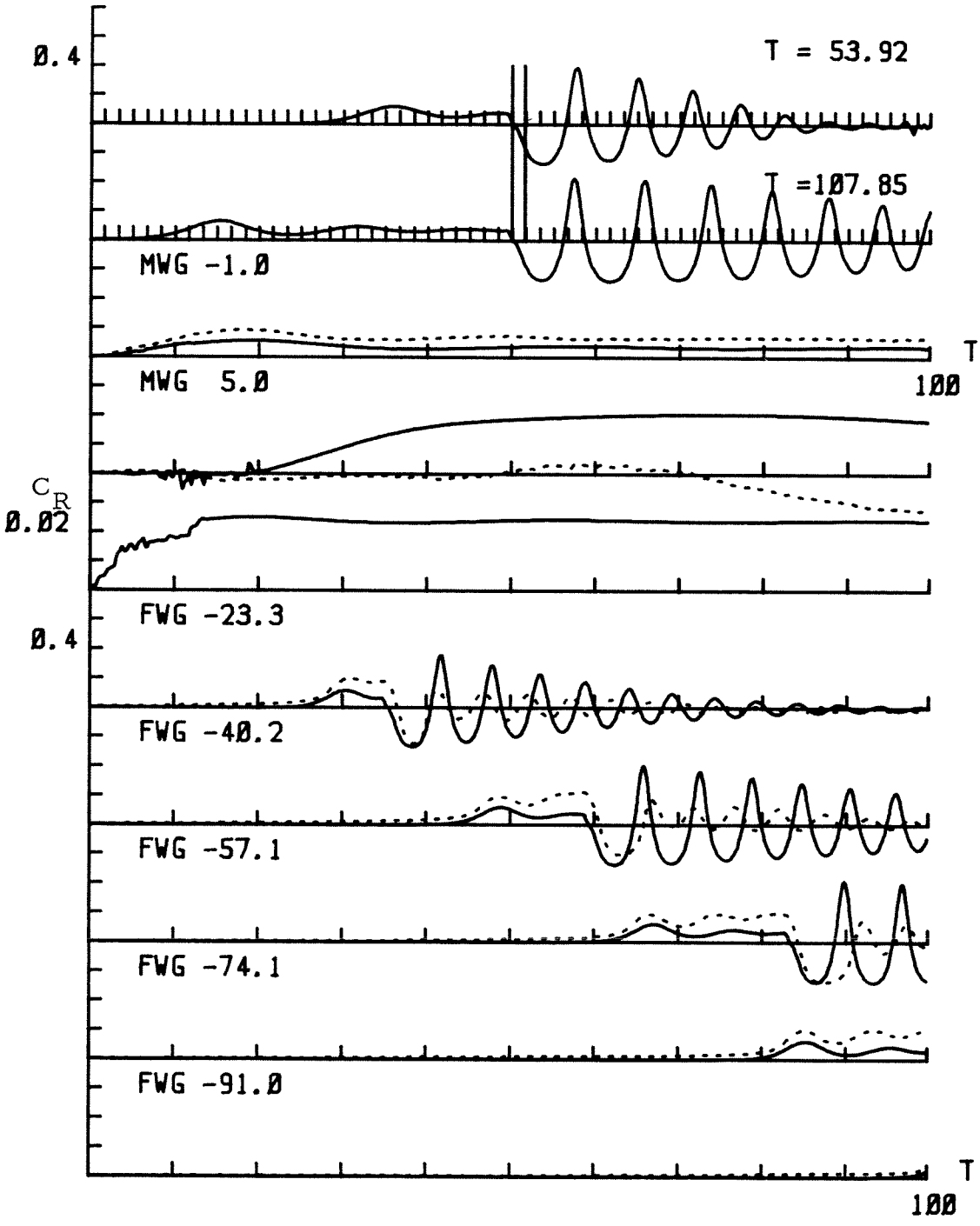

Fig. 5.2.12. Comparison of the surface elevations between the experimental data and the numerical solution given by the Boussinesq model for Fn = 0.80, b_m = 0.185 and ϵ = 0.88.

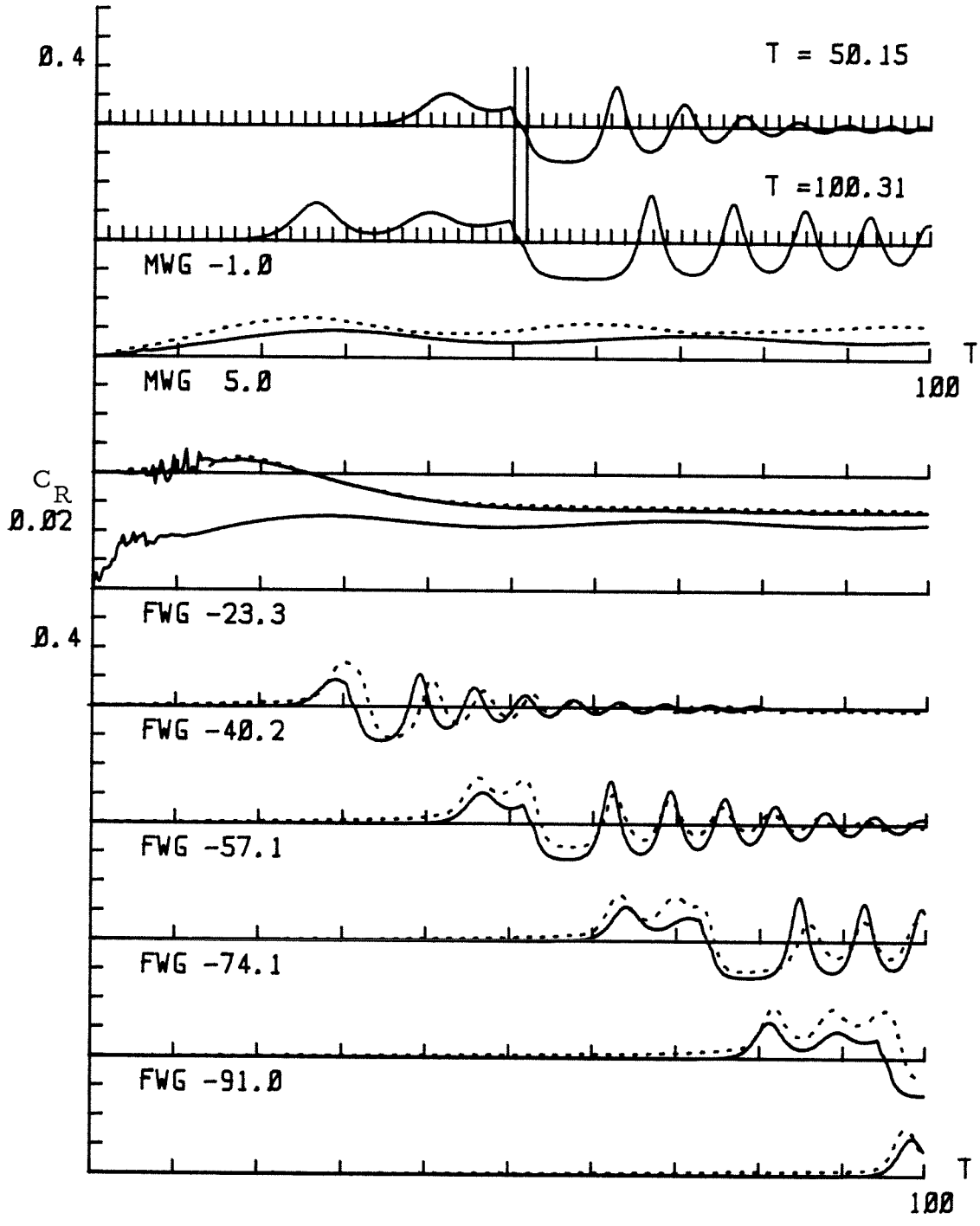

Fig. 5.2.13. Comparison of the surface elevations between the experimental data and the numerical solution given by the Boussinesq model for Fn = 0.90, b_m = 0.185 and ϵ = 0.88.

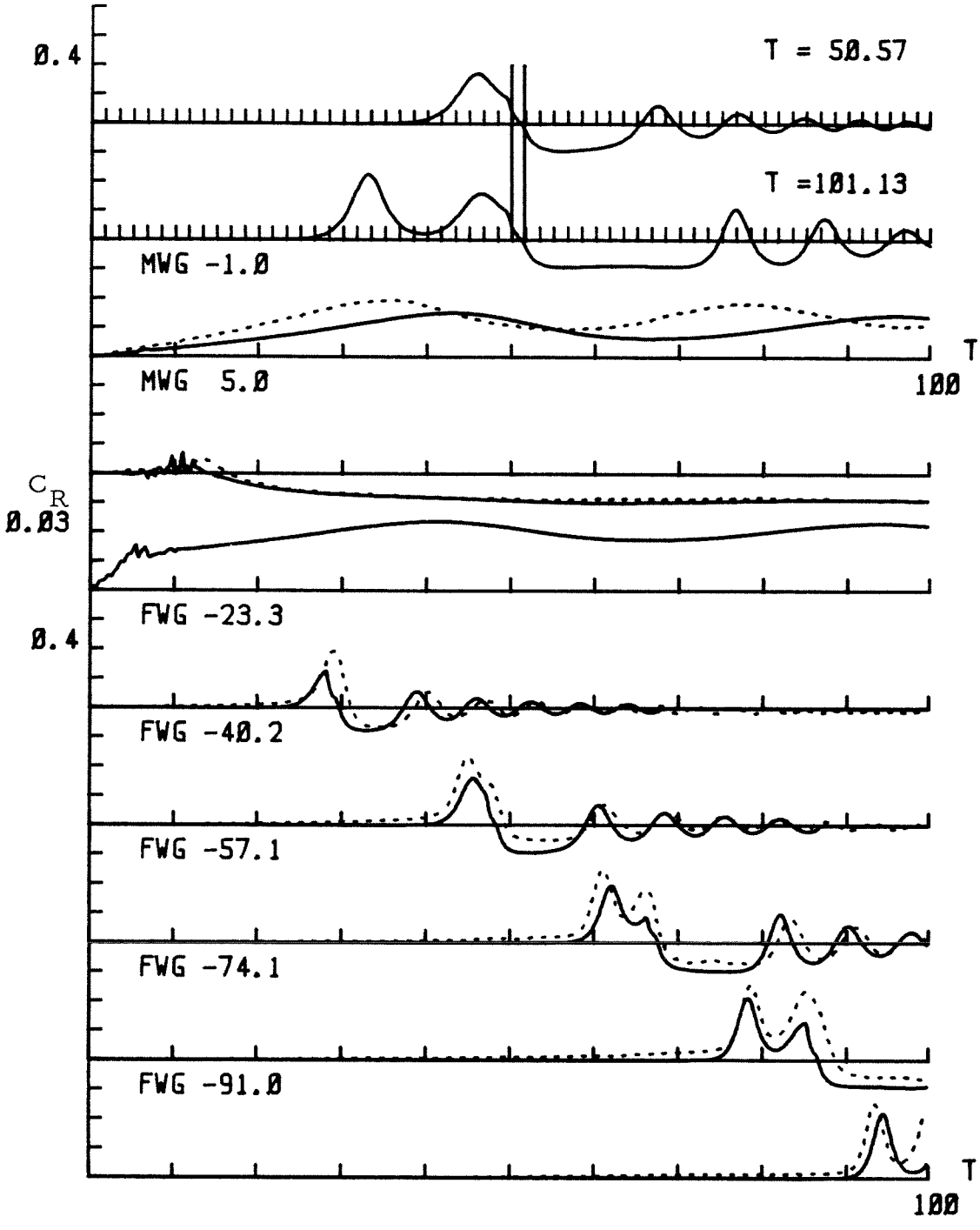

Fig. 5.2.14. Comparison of the surface elevations between the experimental data and the numerical solution given by the Boussinesq model for Fn = 1.01, b_m = 0.185 and ϵ = 0.88.

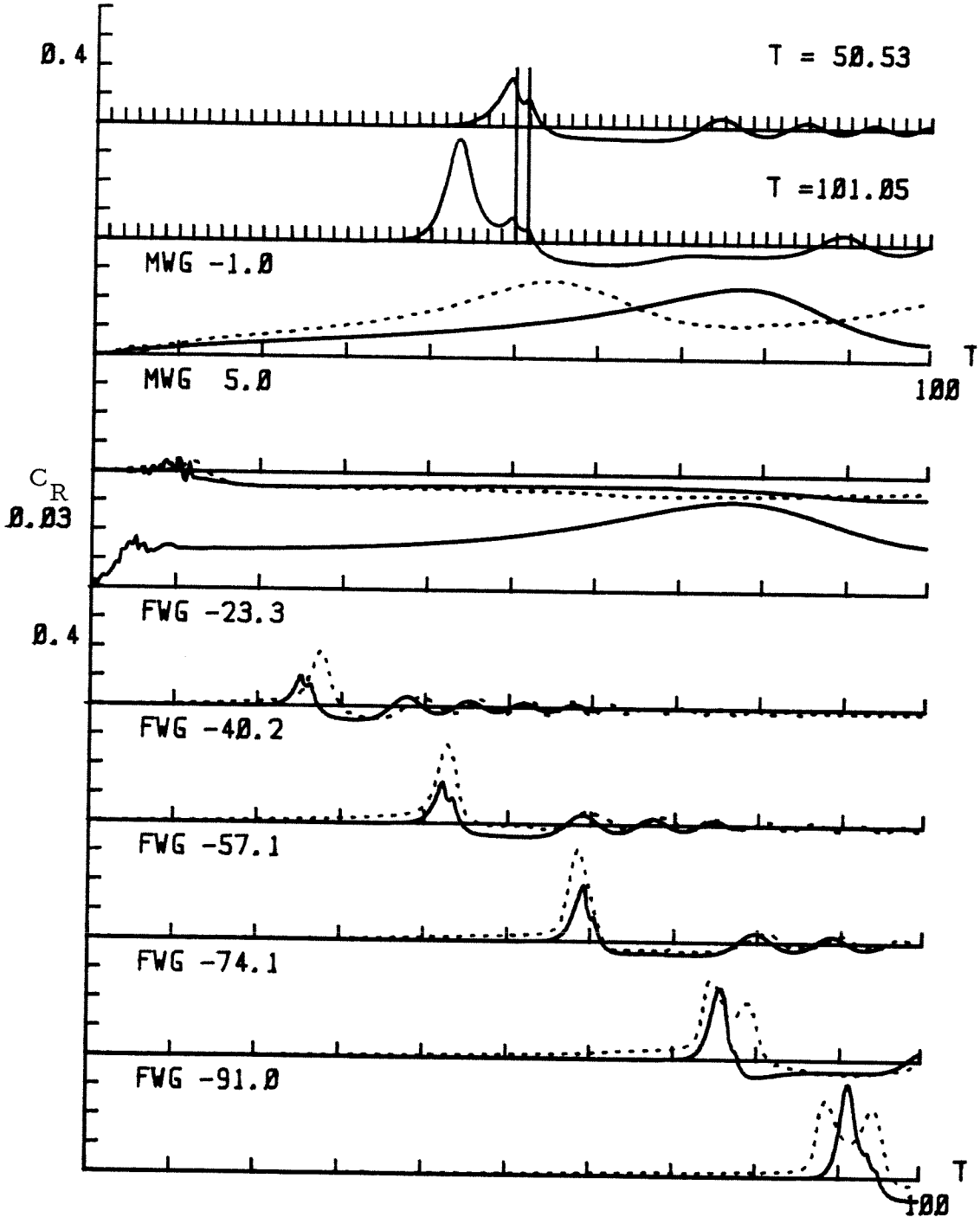

Fig. 5.2.15. Comparison of the surface elevations between the experimental data and the numerical solution given by the Boussinesq model for Fn = 1.12, b_m = 0.185 and ϵ = 0.88.

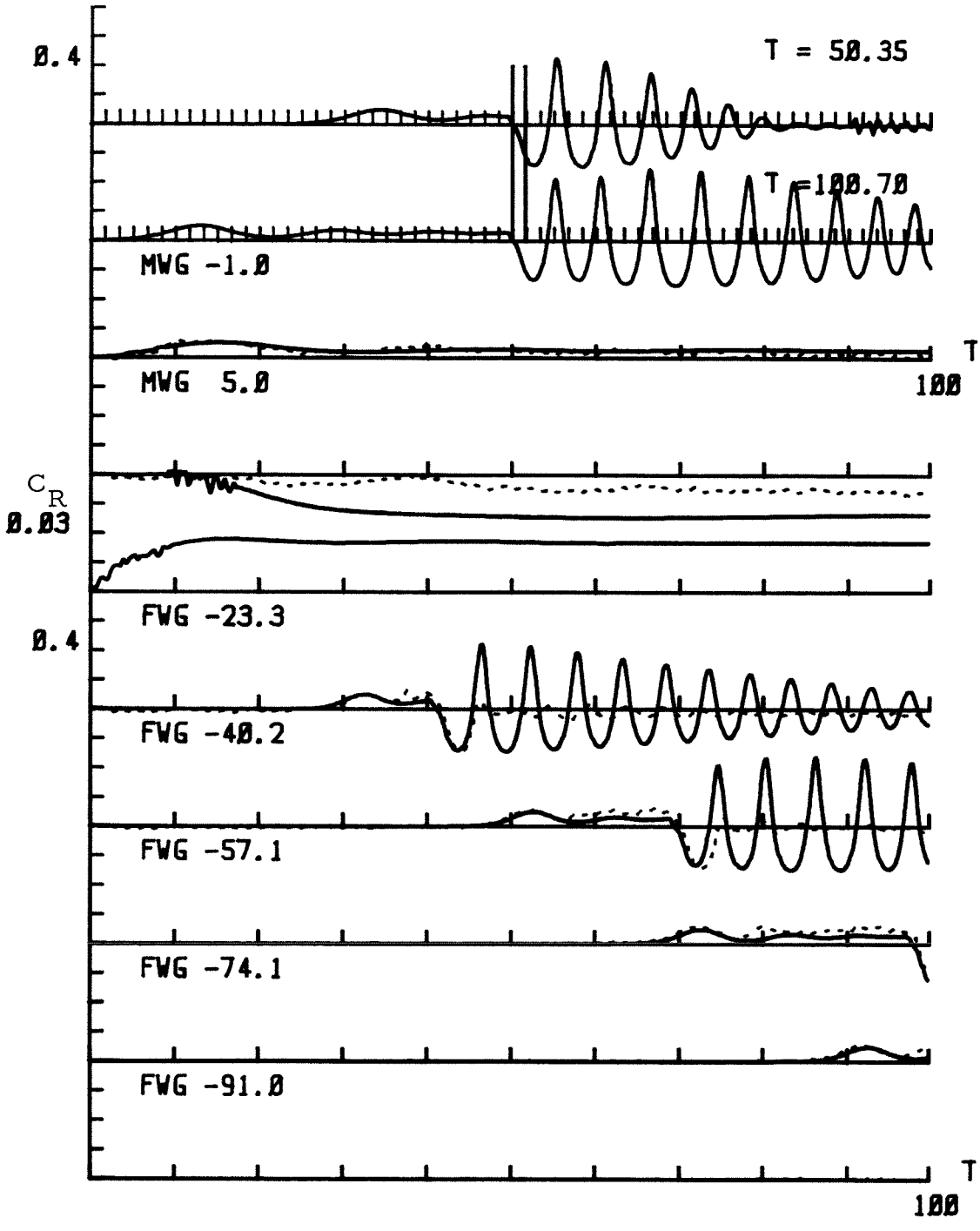

Fig. 5.2.16. Comparison of the surface elevations between the experimental data and the numerical solution given by the Boussinesq model for Fn = 0.73, b_m = 0.2 and ϵ = 0.82.

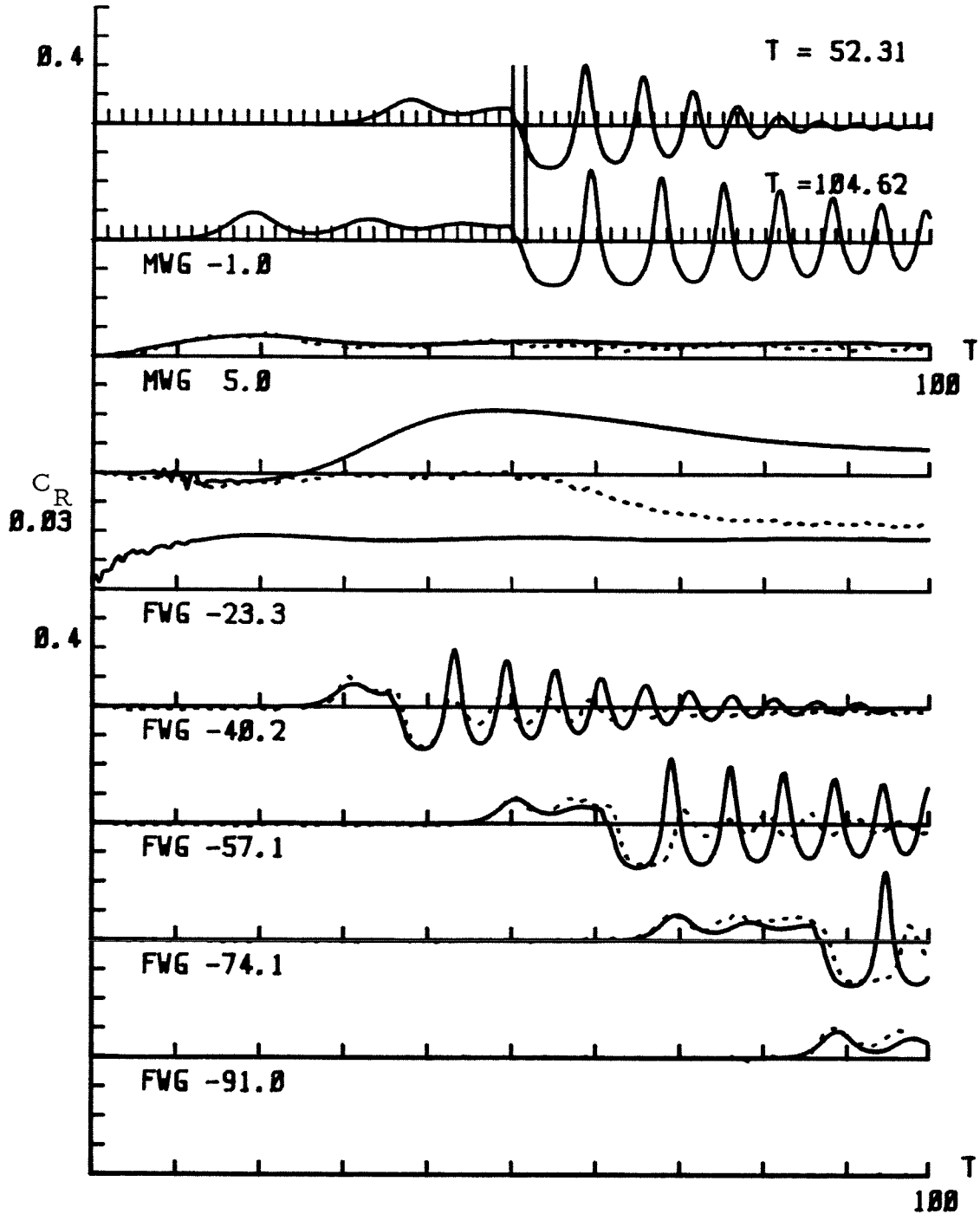

Fig. 5.2.17. Comparison of the surface elevations between the experimental data and the numerical solution given by the Boussinesq model for Fn = 0.82, b_m = 0.2 and ϵ = 0.82.

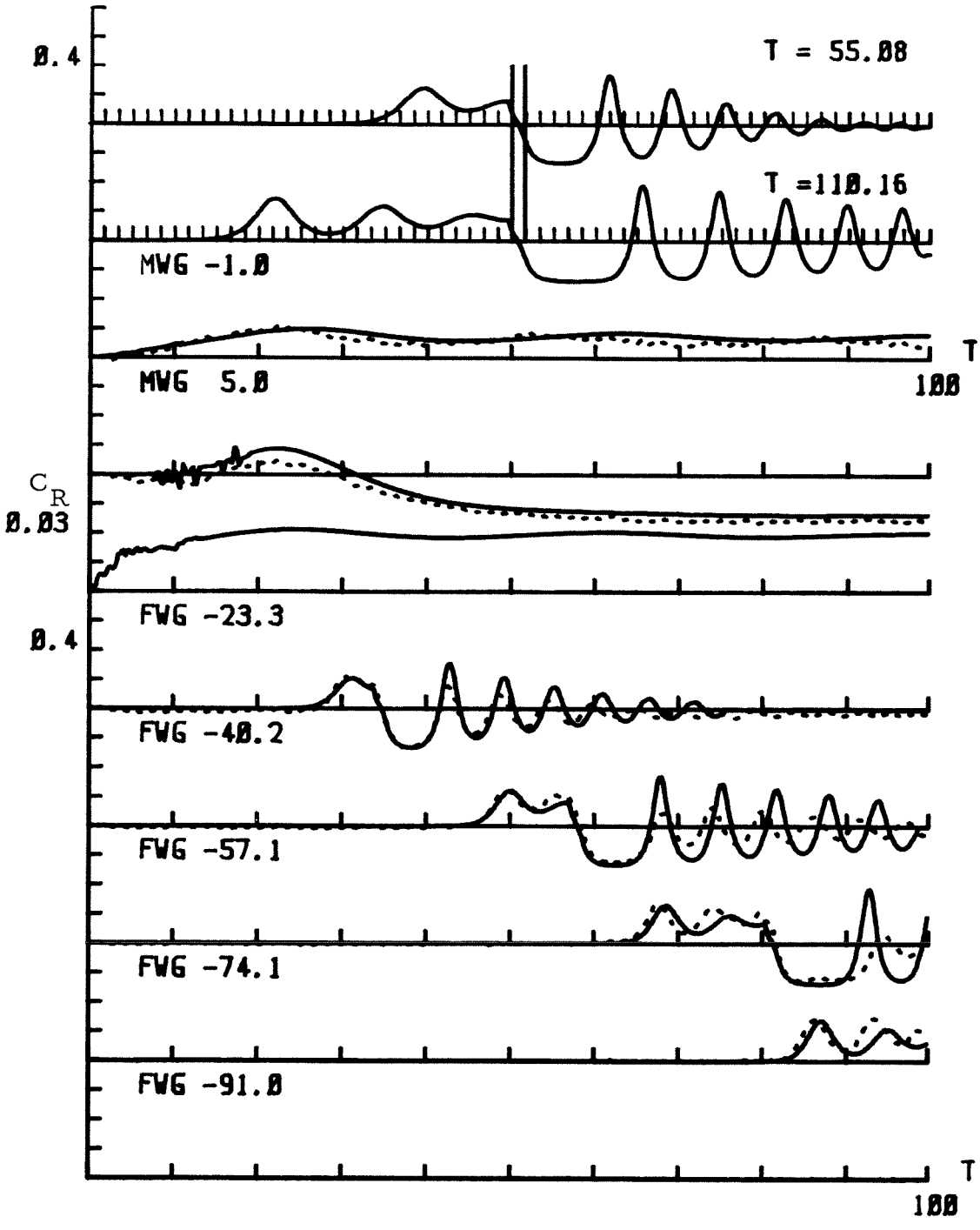

Fig. 5.2.18. Comparison of the surface elevations between the experimental data and the numerical solution given by the Boussinesq model for Fn = 0.89, b_m = 0.2 and ϵ = 0.82.

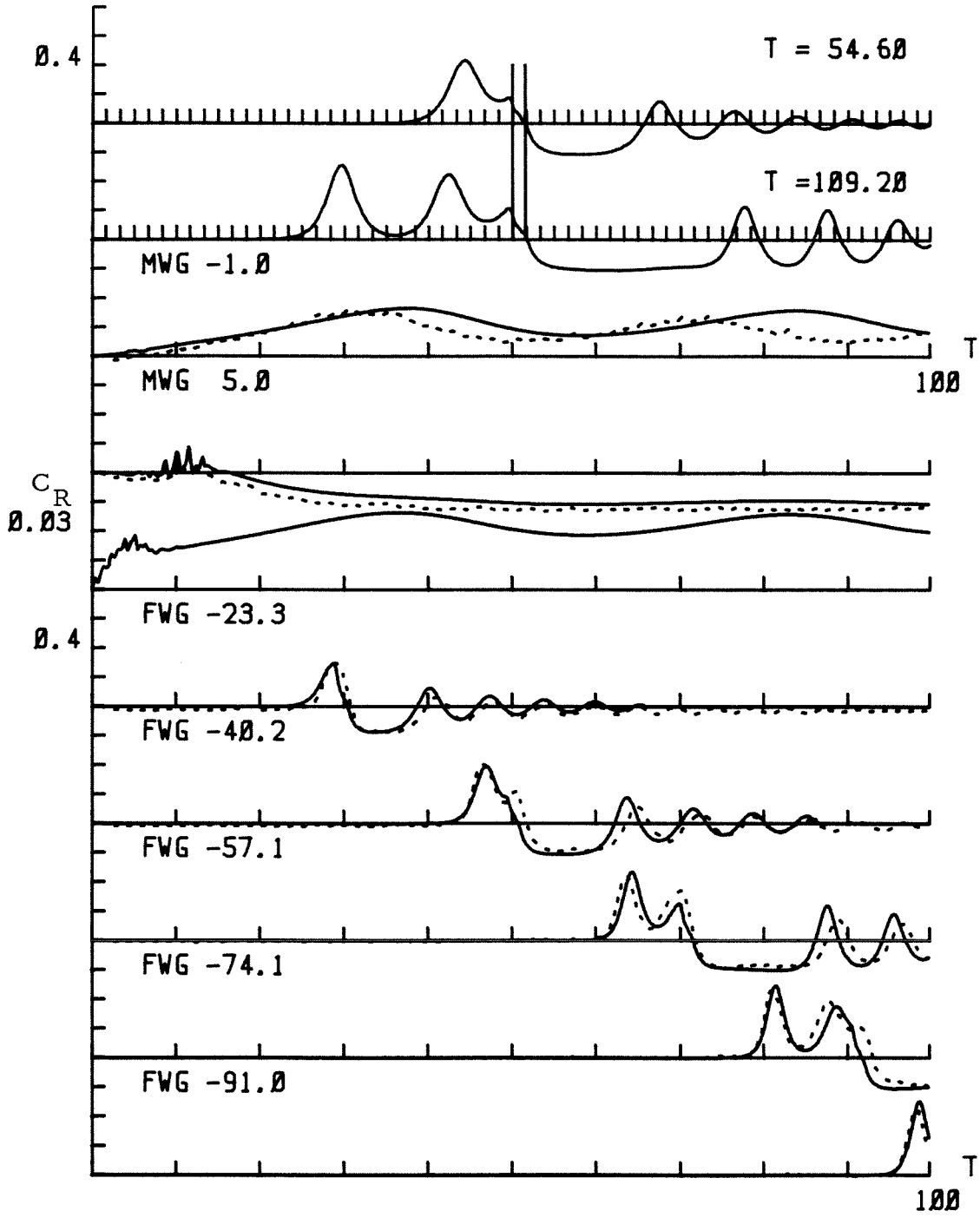

Fig. 5.2.19. Comparison of the surface elevations between the experimental data and the numerical solution given by the Boussinesq model for Fn = 1.01, b_m = 0.2 and ϵ = 0.82.

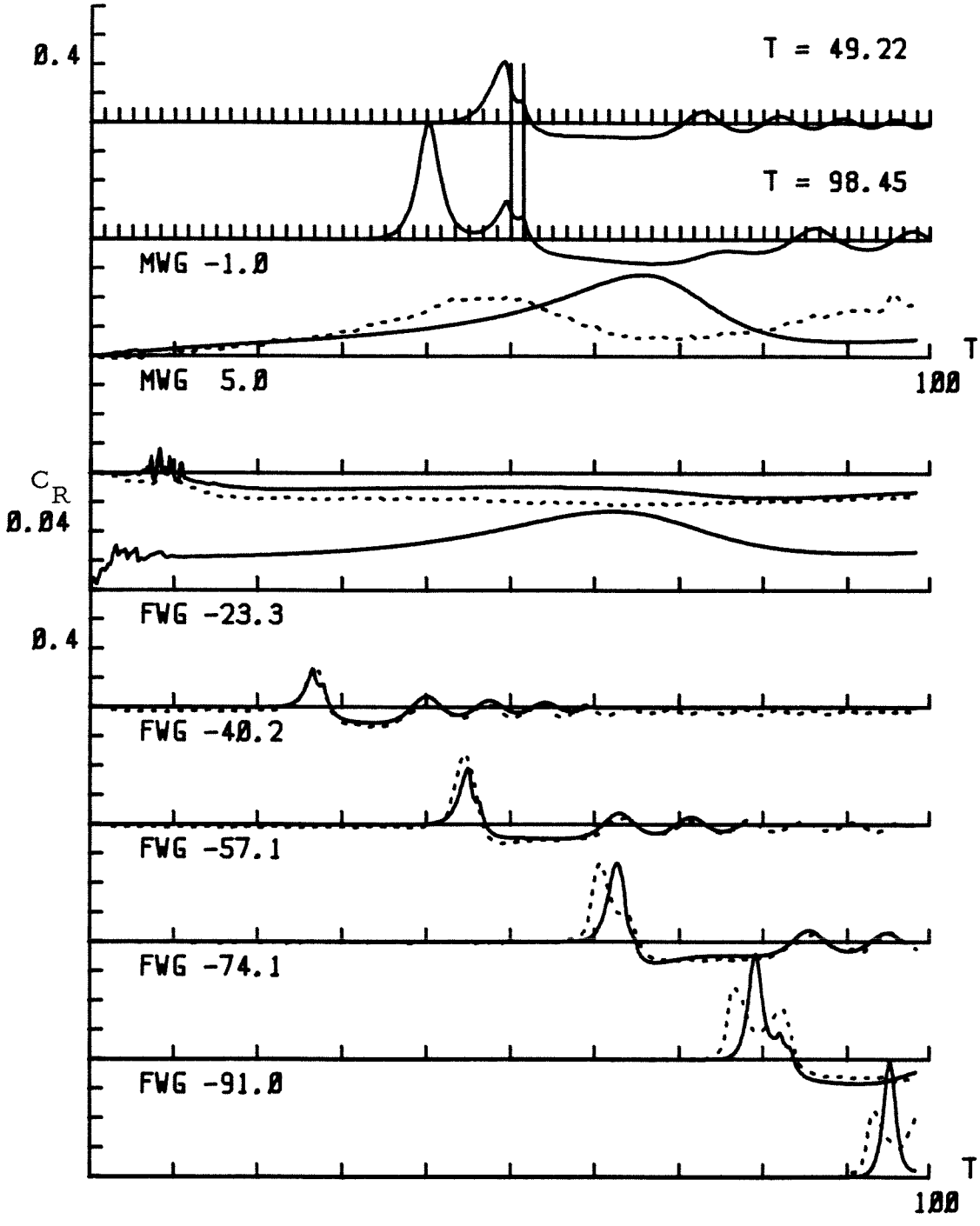

Fig. 5.2.20. Comparison of the surface elevations between the experimental data and the numerical solution given by the Boussinesq model for Fn = 1.12, b_m = 0.2 and ϵ = 0.82.

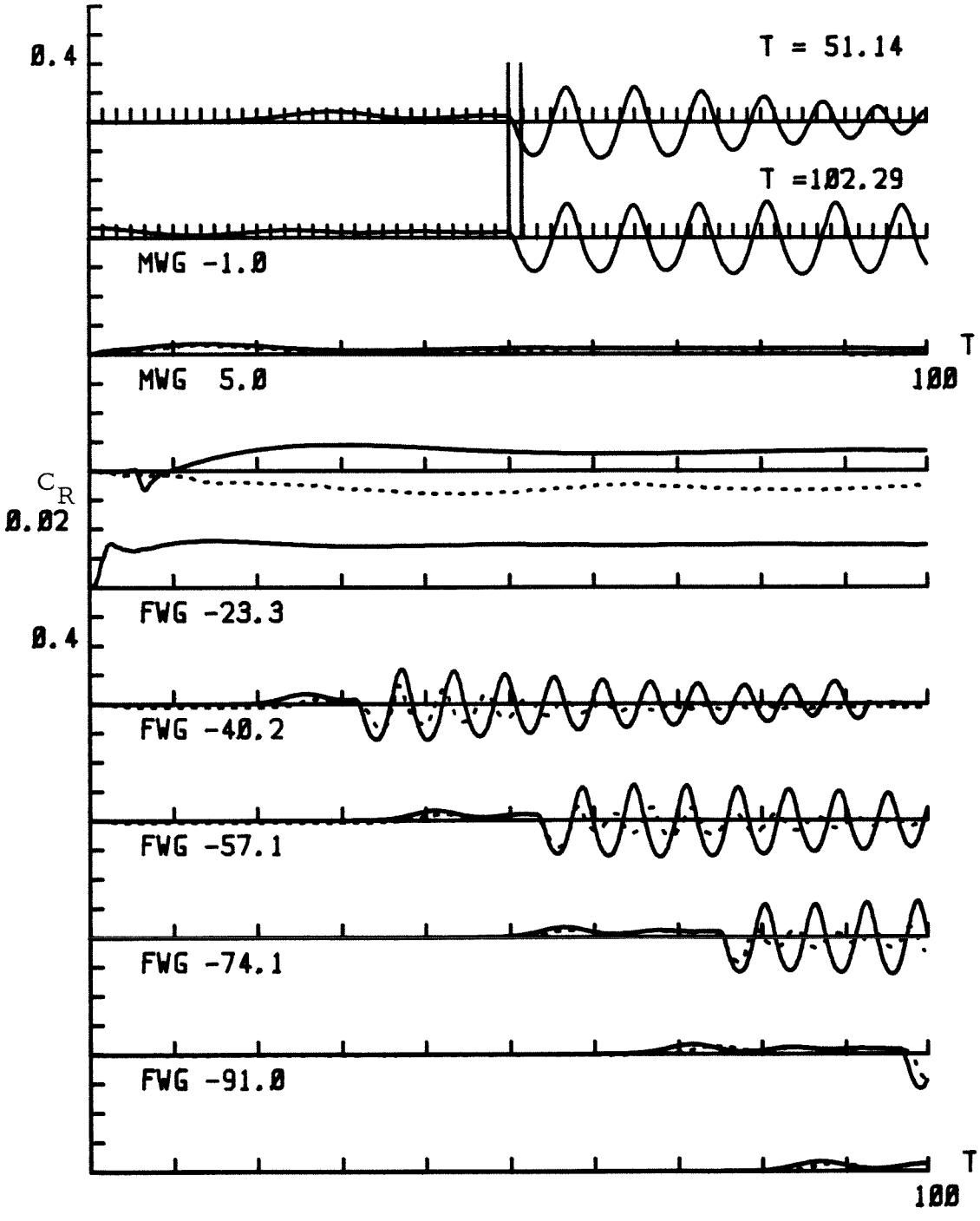

Fig. 5.3.1. Comparison of the surface elevations between the experimental data and the numerical solution given by the KdV model for Fn = 0.72, b_m = 0.15 and ϵ = 1.09.

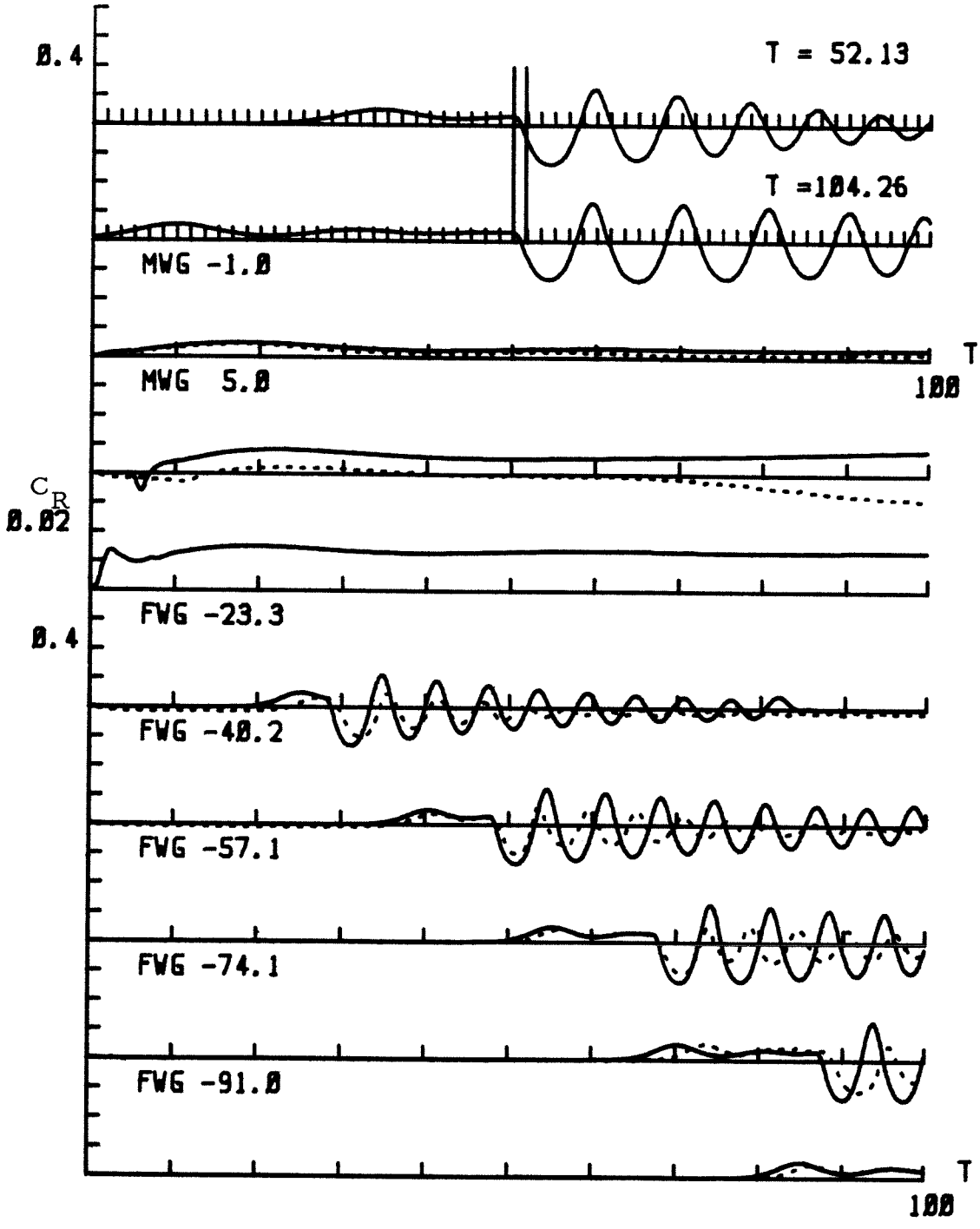

Fig. 5.3.2. Comparison of the surface elevations between the experimental data and the numerical solution given by the KdV model for Fn = 0.79, b_m = 0.15 and ϵ = 1.09.

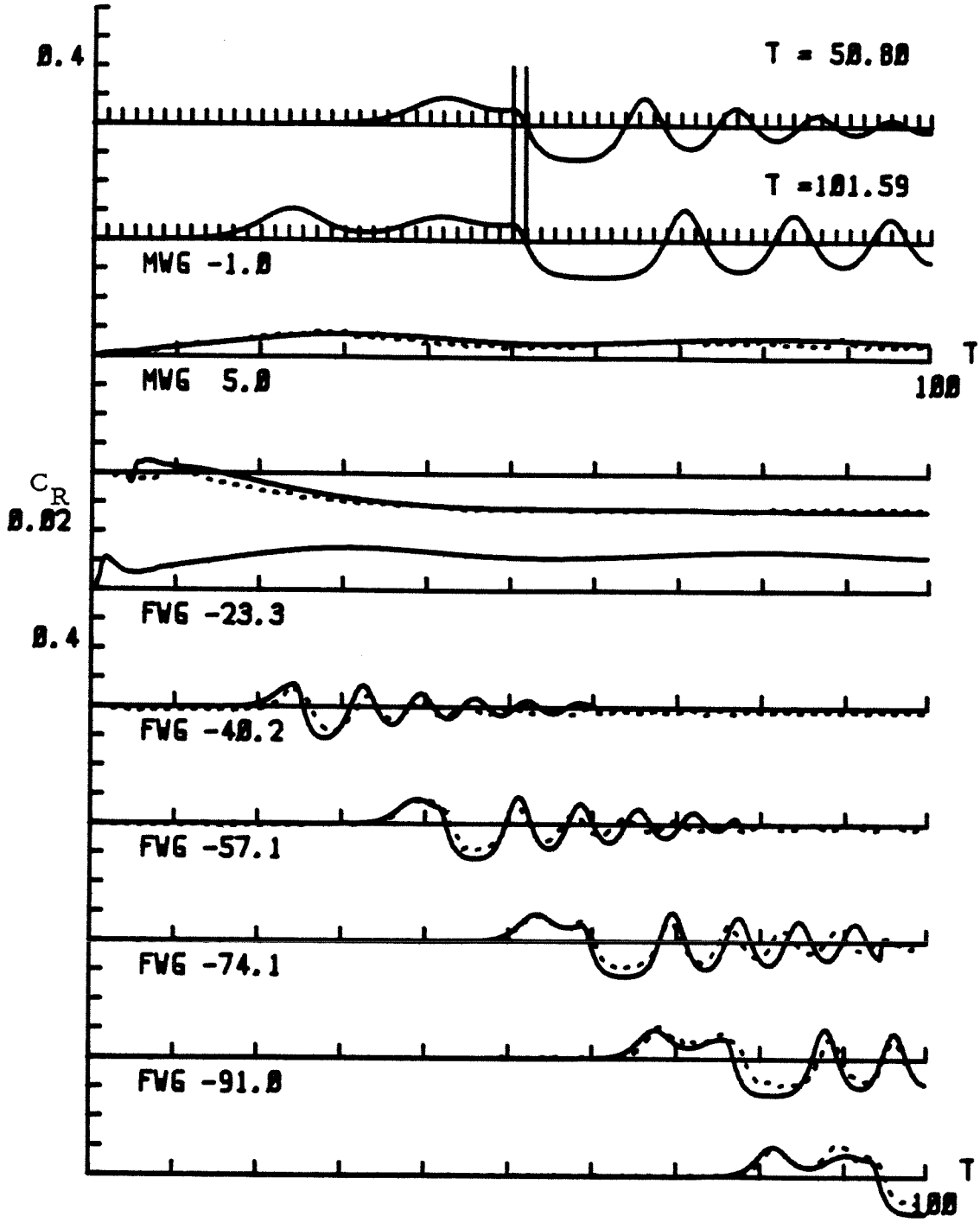

Fig. 5.3.3. Comparison of the surface elevations between the experimental data and the numerical solution given by the KdV model for Fn = 0.90, b_m = 0.15 and ϵ = 1.09.

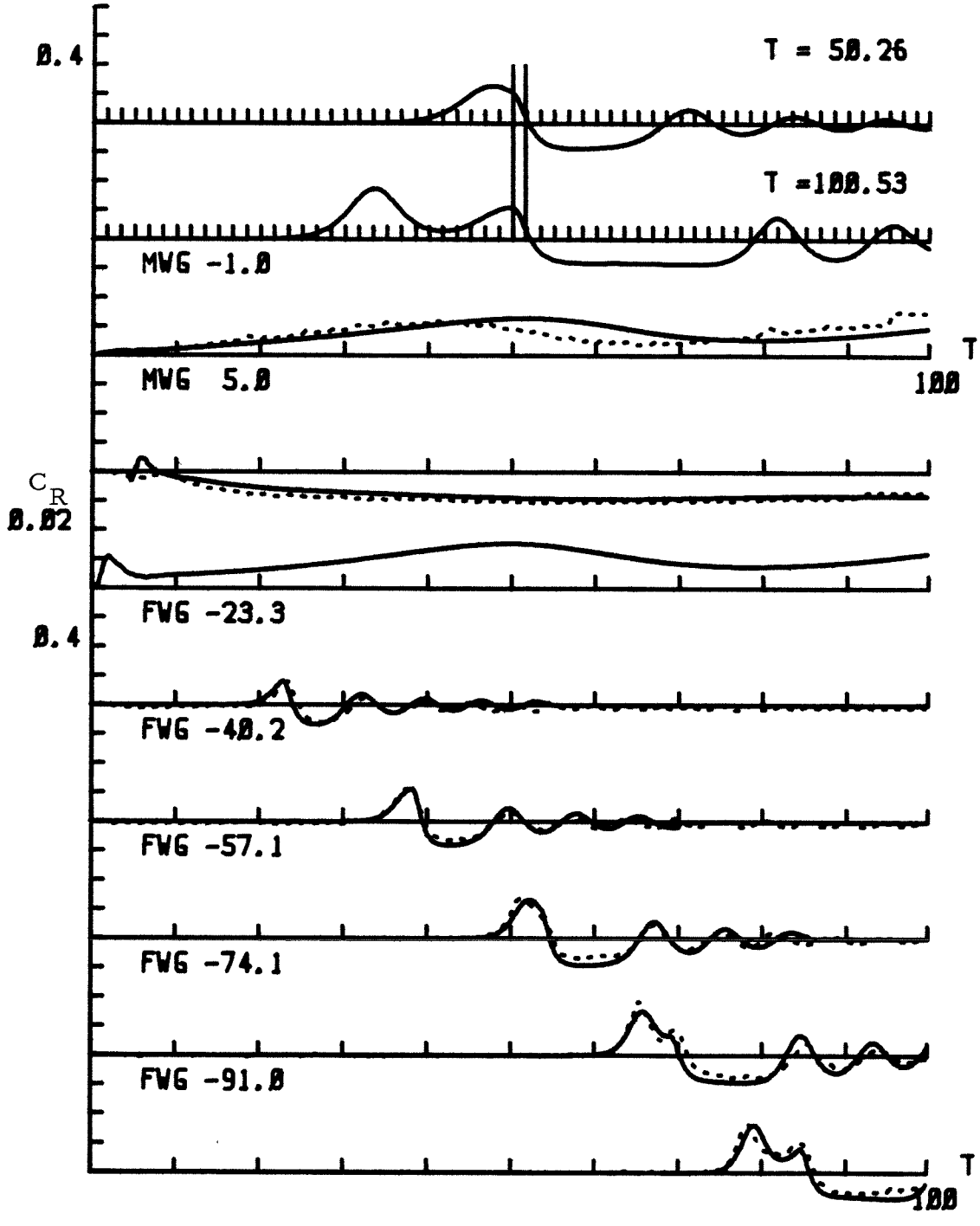

Fig. 5.3.4. Comparison of the surface elevations between the experimental data and the numerical solution given by the KdV model for Fn = 1.01, b_m = 0.15 and ϵ = 1.09.

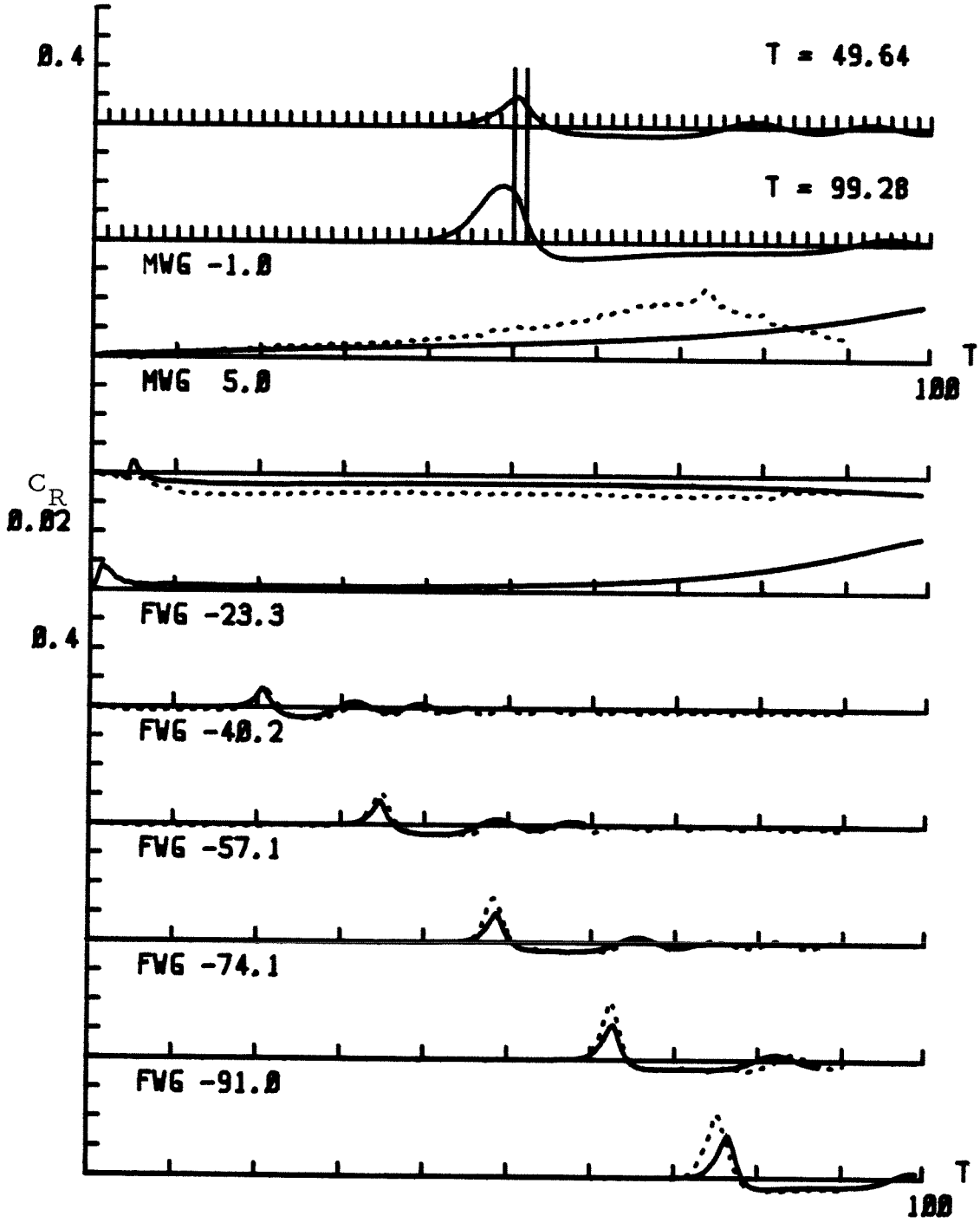

Fig. 5.3.5. Comparison of the surface elevations between the experimental data and the numerical solution given by the KdV model for Fn = 1.11, b_m = 0.15 and ϵ = 1.09.

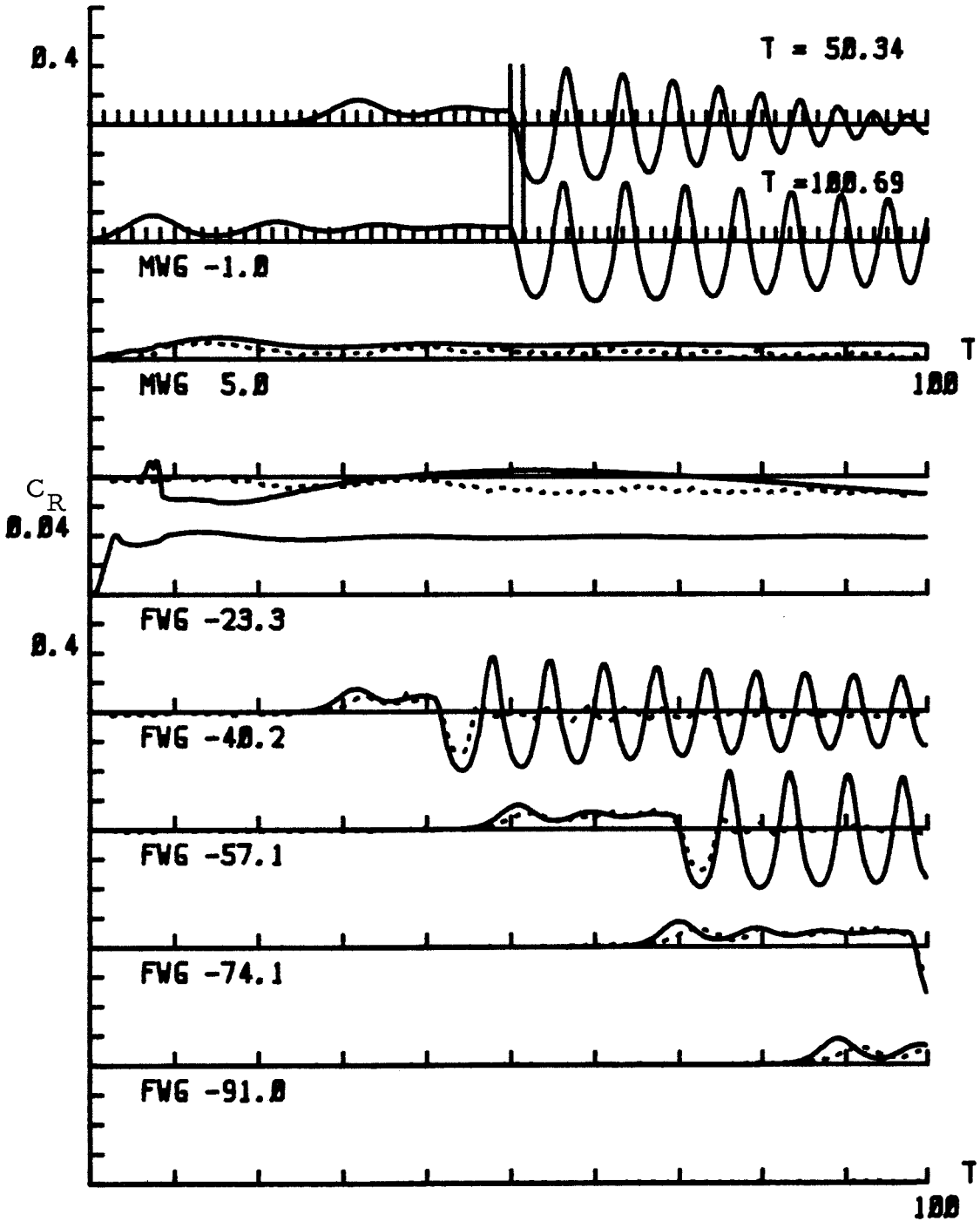

Fig. 5.3.6. Comparison of the surface elevations between the experimental data and the numerical solution given by the KdV model for Fn = 0.73, b_m = 0.2 and ϵ = 0.82.

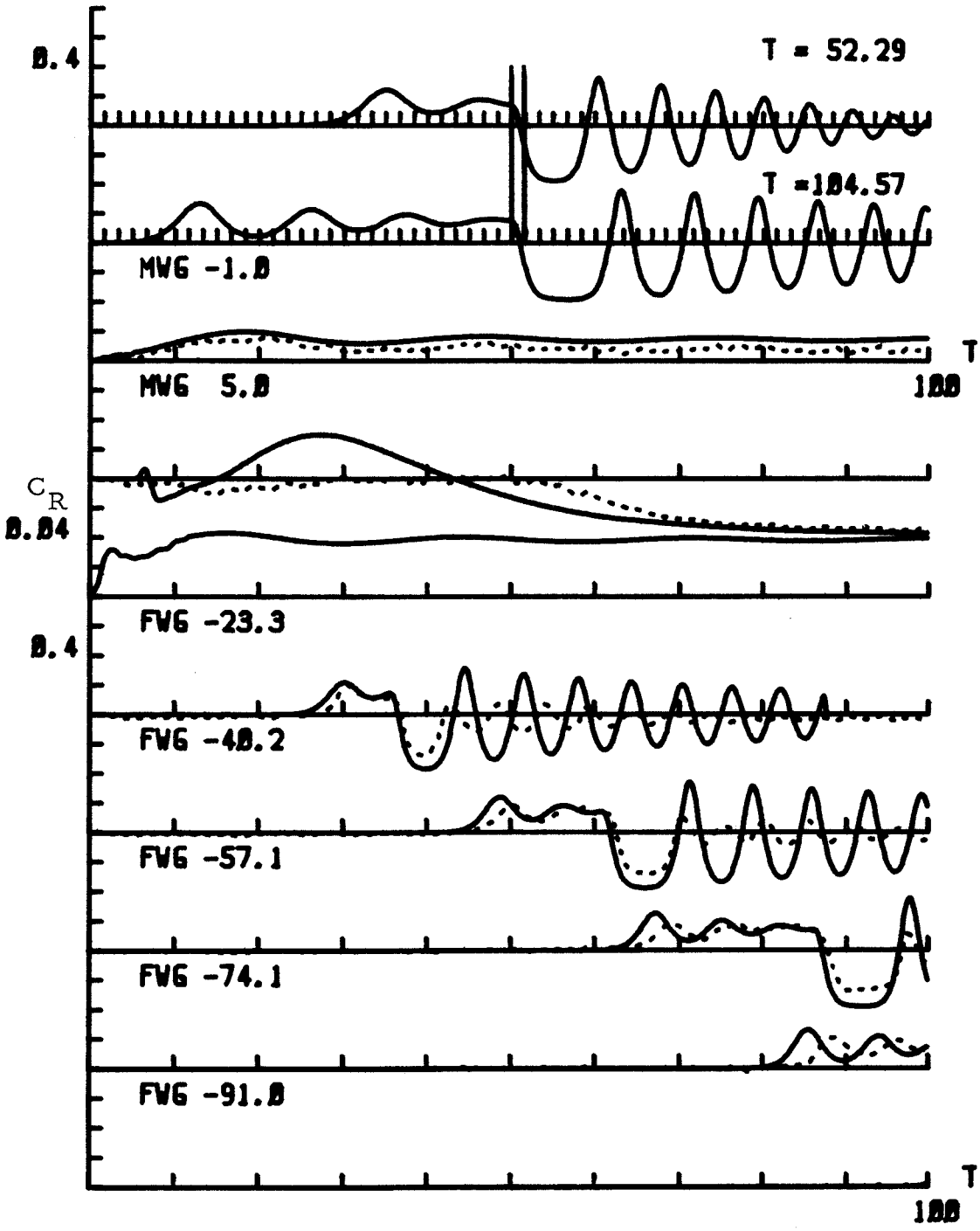

Fig. 5.3.7. Comparison of the surface elevations between the experimental data and the numerical solution given by the KdV model for Fn = 0.82, b_m = 0.2 and ϵ = 0.82.

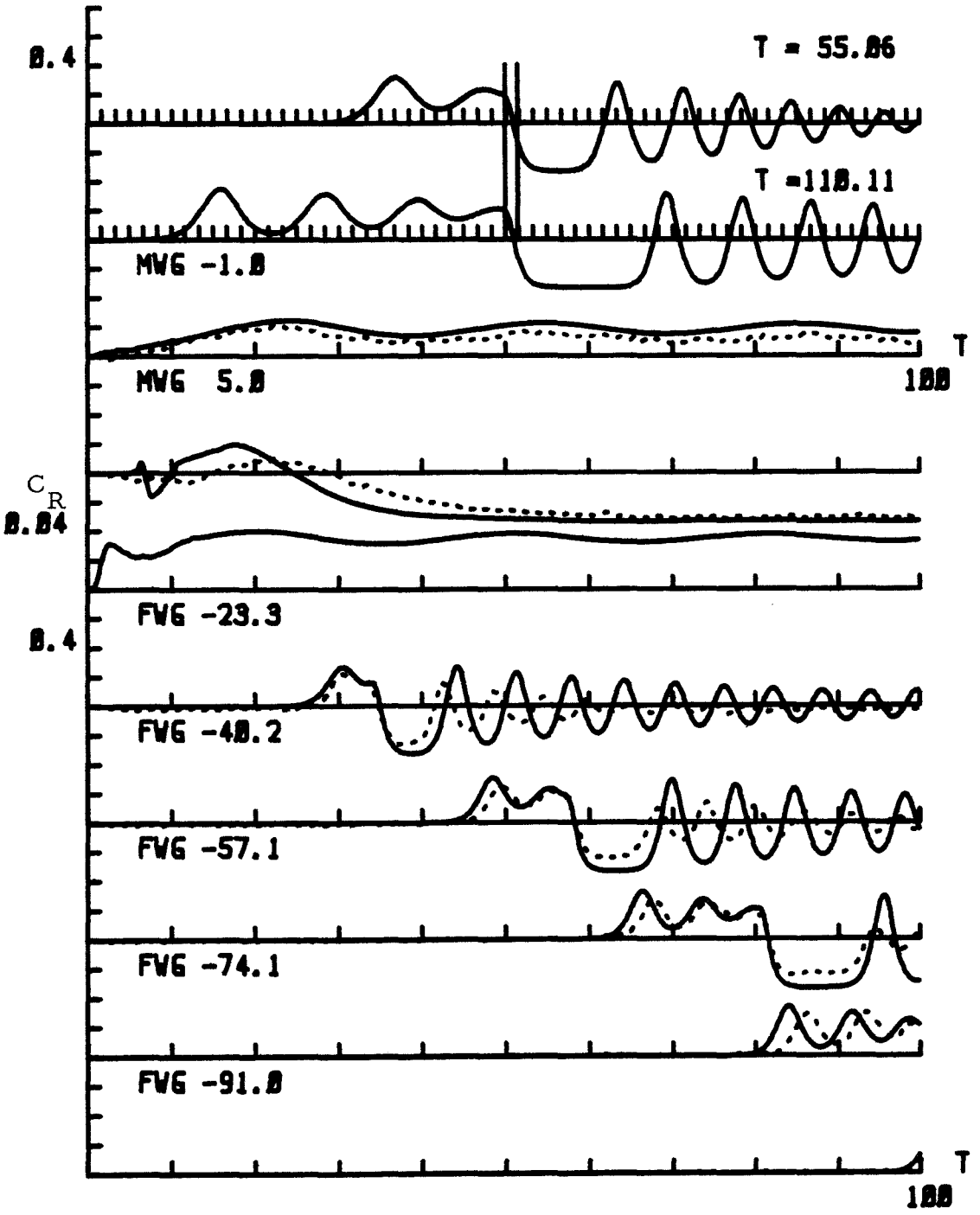

Fig. 5.3.8. Comparison of the surface elevations between the experimental data and the numerical solution given by the KdV model for Fn = 0.89, b_m = 0.2 and ϵ = 0.82.

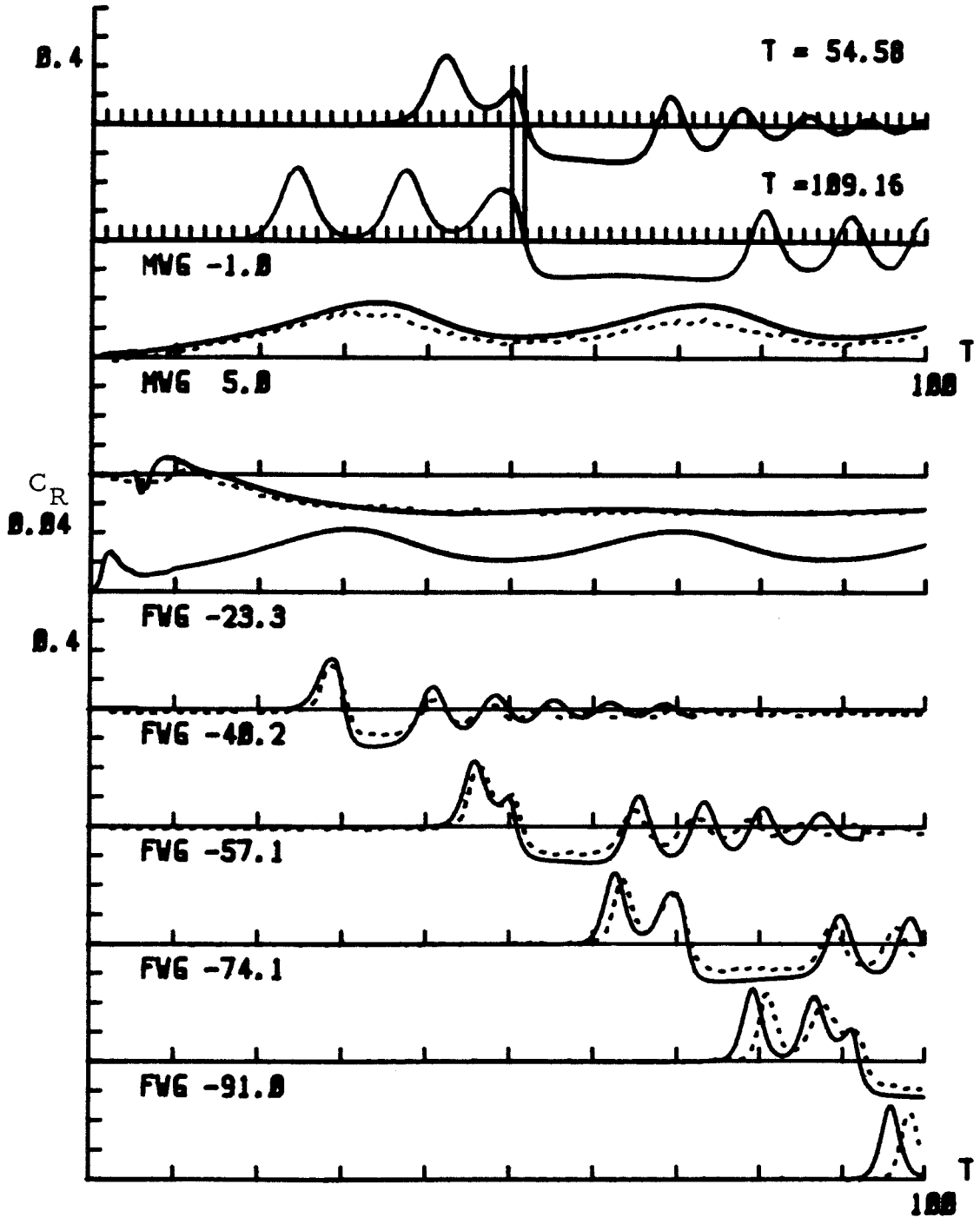

Fig. 5.3.9. Comparison of the surface elevations between the experimental data and the numerical solution given by the KdV model for Fn = 1.01, b_m = 0.2 and ϵ = 0.82.

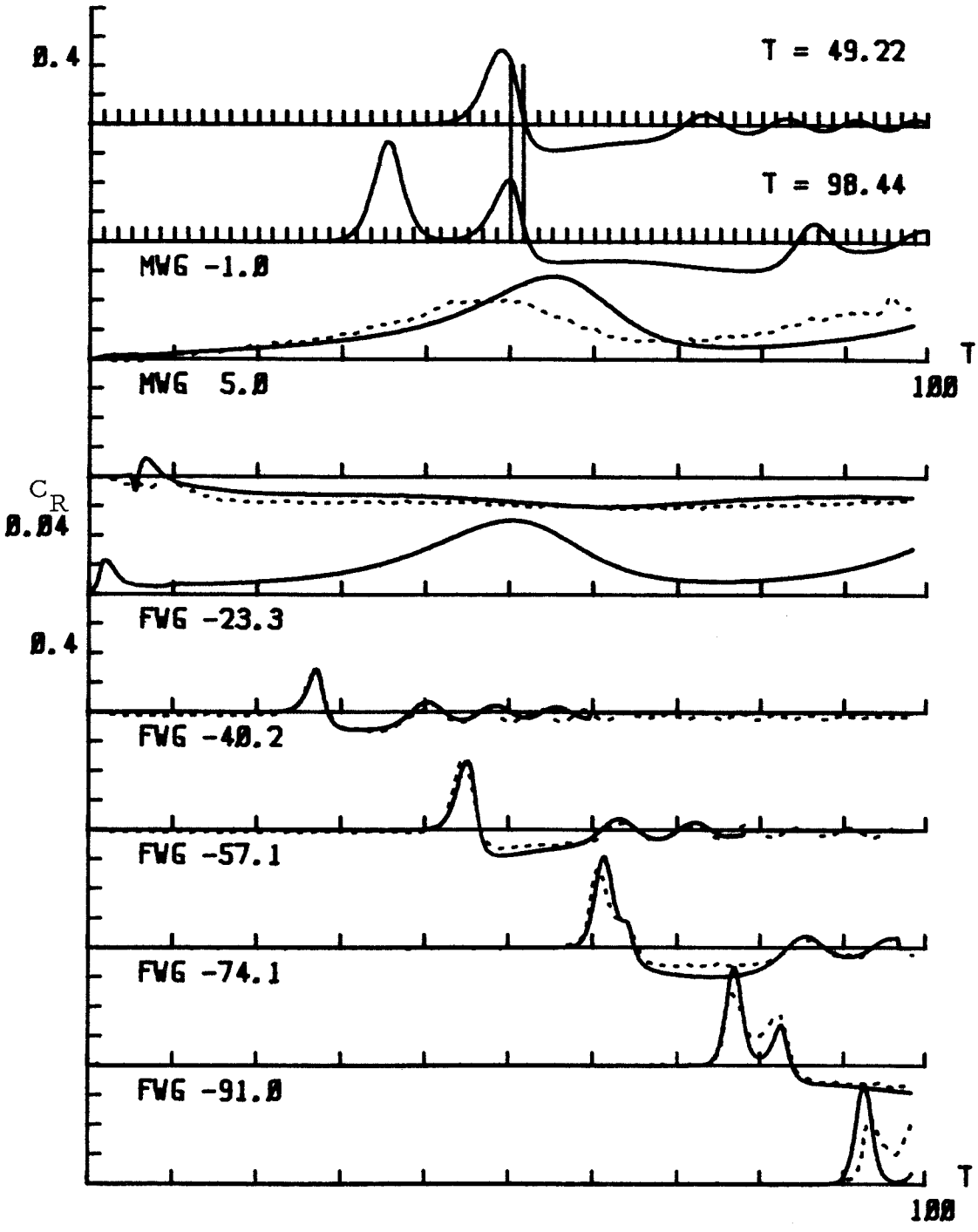

Fig. 5.3.10. Comparison of the surface elevations between the experimental data and the numerical solution given by the KdV model for Fn = 1.12, b_m = 0.2 and ϵ = 0.82.